UNIVERSITY OF NEVADA RENO

Parametric studies on dropwise condensation heat transfer

A dissertation submitted in partial fulfillment of the requirements for the degree of
Doctorate of Philosophy in Mechanical Engineering

by

Kuok Cheng

Dr. Kwang. J. Kim /Thesis Advisor

August, 2014

University of Nevada, Reno
Statewide • Worldwide

THE GRADUATE SCHOOL

We recommend that the thesis
prepared under our supervision by

KUOK KONG CHENG

entitled

Parametric studies on dropwise condensation heat transfer
be accepted in partial fulfillment of the
requirements for the degree of

DOCTORATE OF PHILOSOPHY

Kwang J. Kim, Advisor

Kam K. Leang, Committee Member

Miles Greiner, Committee Member

Thomas W. Bell, Committee Member

Dhanesh Chandra, Committee Member

Marsha H. Read, Ph. D., Dean, Graduate School

August, 2014

Abstract

Wettability of a solid surface with liquids could be tuned based on surface morphologies. This is significant in condensation heat transfer. Condensation is a critical heat transfer mechanism in industrial processes; Dropwise (DWC) and Filmwise (FWC) condensation processes are important and are focus of this study. There are few studies on surface morphology effect on wetting behavior of a solid in relation to condensation heat transfer. We conducted these studies to understand the phenomenon. Condensation heat transfer is affected by condensate droplets properties on the surface. Condensate drop sizes and mobility relationships are important to condensation heat transfer. Droplet sizes and mobility affect population density and condensation heat transfer coefficients directly. The goal of this study is to acquire the fundamental understanding of condensation heat transfer with relation to condensate droplet behavior. In order to achieve this goal, a liquid droplet wetting dynamic model was initially developed for predicting single drop behavior on different surfaces. Heat fluxes were then estimated by combining liquid droplet behavior models and heat transfer model. Condensation experiments were conducted to verify effectiveness of the model.

Experimental results coupled with condensation models revealed relationships between wetting behaviors and condensation heat transfer. Contact angle hysteresis (CAH) remains low at both high and low droplet contact angle, i.e. whether the surface is hydrophilic or hydrophobic. CAH increases with degree of wetting, but coating thermal conductance also increases. Details of drop (DWC) and film-wise (FWC) condensation are presented.

Acknowledgements

I would like to thank my adviser Dr. Kwang J. Kim (currently with University of Nevada Las Vegas) for the guidance and support for this project. He is my mentor and he helps me in technical, moral and financial supports to start and continue this program. I thank him for all his involvements and sacrifice for this project.

I also would like to thank Dr. Bong June Zhang (NBD Nano in Boston), Dr. Sunwoo Kim (University of Alaska Fairbanks), Dr. Chiyoung Lee (Korea Atomic Research Institute) and Dr. Sangsoo Lee (Texas A&M, Kingsville) with technical supports. I owe their help for details on designs and procedures of experiments as well as modeling perspectives.

I also would like to thank Dr. Kam Leang, Dr. Miles Greiner, Dr. Dhanesh Chandra and Dr. Thomas W. Bell for being as my committee members and their supports.

I gratefully acknowledge the financial support of National Science Foundation GK-12 E-fellowship Program (DGE #1045584).

Finally, I would like to thank my family for all the support and encouragement for me to finish this program.

Table of Contents

List of Figures

List of tables

Permissions

Figure 1.2	Reprinted from B. J. Zhang, J. Park, K. J. Kim, H. Yoon, “Biologically Inspired Tunable Hydrophilic/Hydrophobic Surfaces: A Copper Oxide Self-Assembly Multitier Approach,” Bioinspiration & Biomimetics, Vol. 7(3), 036011 (2012: DOI: http://dx.doi.org/10.1088/1748-3182/7/3/036011) with permission from © IOP Publishing. Reproduced with permission from IOP Publishing. All rights reserved.
Figure 4.1(c-d)	Permission to reprint from SPIE publication, Kuok Cheng, Bong June Zhang ; Chi Young Lee, Sunwoo Kim, et al., "Biomimetic super-hydrophobic surfaces for use in enhanced dropwise condensation", *Proc. SPIE* 7975, Bioinspiration, Biomimetics, and Bioreplication, 79750Y (March 23, 2011); doi:10.1117/12.882189

Nomenclature

A	Area of control surface, m^2
A_C	Drop cap area, m^2
A_{LG}	Liquid/gas interfacial area, m^2
A_{SG}	Solid/gas interfacial area, m^2
A_{SL}	Solid/liquid interfacial area, m^2
A_P	Drop projection area, m^2
$A_{t,i}$	Tube inner area, m^2
$A_{t,o}$	Tube outer area, m^2
b	Fin diameter, m
C_{pc}	Coolant heat capacity
D_d	Hydraulic diameter, m
$D_{t,i}$	Tube inner diameter, m
$D_{t,o}$	Tube outer diameter, m
E	Surface energy, J
E_{drop}	Drop energy, J
E_{hys}	Hysteresis energy, J
f	Friction factor
F	Line force, N/m
f_w	Projected area fraction for fully wetting space
g	Gravitational acceleration, m/s^2
G	Drop radius growth rate, m/s
G_1	Small drop radius growth rate, m/s
G_2	Large drop radius growth rate, m/s
h	Fin height, m
H	Droplet height, m
h_c	Coolant heat transfer coefficient, W/m^2-K
h_{int}	Interfacial heat transfer coefficient, W/m^2-K
h_{FWC}	Filmwise condensation heat transfer coefficient, W/m^2-K
H_{fg}	Latent heat of vaporization
Ja	Jacob number
k_c	Condensate thermal conductivity, W/m-K
k_{fin}	Fin thermal conductivity, W/m-K
k_t	Tube thermal conductivity, W/m-K
k_v	Vapor thermal conductivity, W/m-K
L	Fin distance, m
M	Total liquid mass of control surface, kg
$\bar{M}$	Molar mass, kg/mol
$\dot{m}''$	Mass flux rate of vapor condensation, kg/m^2-s
$\dot{m}_c$	Coolant mass flow rate, kg/s
M_{in}	Total incoming vapor mass to control surface, kg
M_{out}	Total mass leaving control surface, kg
$n(r)$	Small drop sizes distribution, m^{-3}

$N(r)$	Large drop sizes distribution, m^{-3}
N_S	Nucleation sites per unit area, m^{-2}
Nu_c	Coolant Nusselt number
Pr_c	Coolant Prantl number
q	Heat transfer rate, W
q''	Total heat flux, W/m^2
q_d	Single drop heat transfer rate, W
R	Drop radius, m
R_0	Initial radius, m
$\bar{R}$	Ideal gas constant, J/mol-K
Re_c	Coolant Reynolds number
R_{tot}	Total thermal resistant, K/W
R_c	Coolant thermal resistant, K/W
R_w	Tube wall thermal resistant, K/W
R_{cond}	Condensation thermal resistant, K/W
r	Drop radius used in modeling, m
r_e	Effective drop radius, m
r_{max}	Maximum drop radius, m
r_{min}	Minimum drop radius, m
r_f	Roughness ratio
S	Droplet sweeping rate, s^{-1}
t	time, s
ΔT	Total temperature difference, K
$T_{c,ave}$	Average coolant temperature, K
$T_{c,o}$	Coolant outlet temperature, K
$T_{c,i}$	Coolant inlet temperature, K
ΔT_{coat}	Temperature difference due to coating thickness, K
ΔT_{curve}	Temperature difference due to drop curvature, K
ΔT_{drop}	Temperature difference due to condensate conduction, K
ΔT_{int}	Interfacial temperature difference, K
T_{sat}	Saturation temperature, K
T_w	Surface temperature, K
U	Overall heat transfer coefficient
V	Drop volume, m^3
v_{fg}	Liquid/gas specific volume, m^3/kg
X_i	Measured values
Y	Calculated values
U_X	Measured uncertainties
U_Y	Calculated uncertainties

Greek Letter

α	Tilting angle
γ	Surface tension, N/m

γ_{LG}	Liquid/gas surface tension, N/m
γ_{SG}	Solid/gas surface tension, N/m
γ_{SL}	Solid/liquid surface tension, N/m
δ	Coating thickness, m
ε	Coating porousity
θ	Contact angle
θ_0	Young’s contact angle
θ_{adv}	Advancing contact angle
θ_{rcd}	Receding contact angle
θ_E	Equilibrium contact angle
μ	Condensate liquid viscosity, N-s/m^2
ρ	Condensate liquid density, kg/m^3
ρ_g	Vapor liquid density, kg/m^3
τ	Sweeping period, s
$\hat{\sigma}$	Accommodation coefficient
ϕ	Ratio of top surface area to projection area

1. Introduction

1.1 Project scope

Condensation is a critical heat transfer mechanism in numerous industrial processes and there have been many efforts to promote “dropwise” condensation (DWC), which shows a higher heat transfer rate than that of a “filmwise” condensation (FWC) [1]. Dropwise condensation has been researched for over 70 years and it is still an important subject in phase change heat transfer. Figure 1.1 illustrates a dropwise condensation process. DWC takes place when the liquid condensate does not fully wet a solid surface. The condensate does not spread but forms separate drops across the surface. In general, the greatest portion of the thermal resistance in FWC comes from the liquid condensate due to its poor thermal conductivity. During the condensation process, the vapor impinges on to the condensing surface; droplets are formed on the surface due to the external force, i.e. gravity, and release heat to the surface. Droplets grow very rapidly due to the continuing direct condensation of vapor on to the condensate. As the drops reach a critical radius, they depart from the condensing surface, taking in other droplets within their path. They then sweep a portion of the condensing surface clean, where new droplets are generated again. A continuous cycle of drop generation and departure is formed as a result. The effect of high thermal resistance due to condensate film observed in FWC can be minimized. Therefore, the rate of heat transfer in DWC is substantially greater than that of FWC. However, the long term DWC conditions are difficult to maintain in most cases.

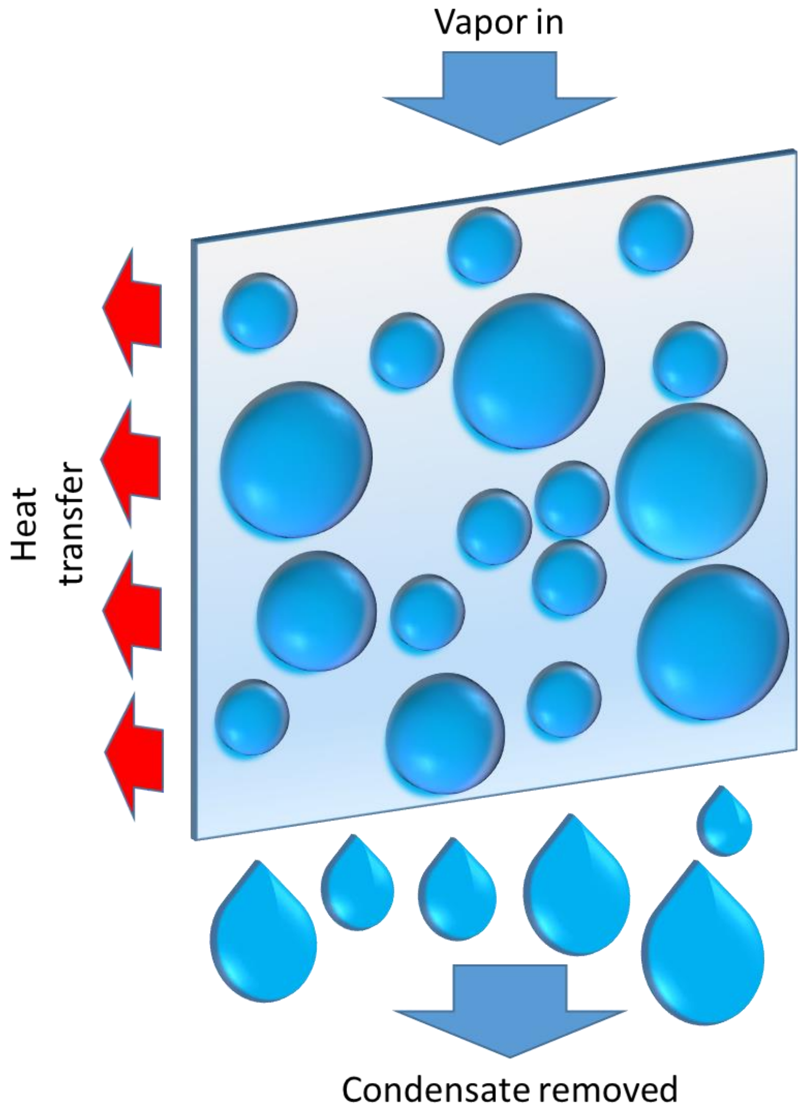

Figure 1.1 Dropwise condensation process illustration

A common method to promote the "dropwise" condensation is surface treatment on condensing surfaces using organic coatings, which can shift condensation modes from a filmwise (FWC) to a dropwise (DWC). Super-hydrophobic can be manufactured by using organic coatings. A super-hydrophobic surface is defined when water contact angle is greater than 150°, and it has the properties to repel water. In particular, super-hydrophobic surface induces water droplet to roll off (called self-cleaning) and this can increase the condenser performance by increasing the rate of refreshing on condensing surfaces (called “surface renewal”). Excellent examples of similar surfaces can be found in natural design such as rose petals and water striders. These designs utilize epidermal cell-structures to achieve super-hydrophobicity. Super-hydrophobic surface can be created by utilizing micro/nano surface textures. Super-hydrophobic surface could be made with inherited hydrophilic materials as explained by Barthlott and Neinhuis [2]. A SEM image of rose petals is shown in Figure 1.2(a). It should be noted that rose petals are covered with micro-sized tiers with nano-sized tiers on the surface [3]. Similarly, surfaces of wings and feet of aquatic insects, such as water striders or other flying insects are composed of micro surface textures as shown in Figure 1.2 [4]. Anti-wetting properties can be achieved with intricate micro textures. Trapped air between micro/nano textures can repel water, as found in plants and insects. Bio-inspired textured surfaces can be utilized in numerous applications.

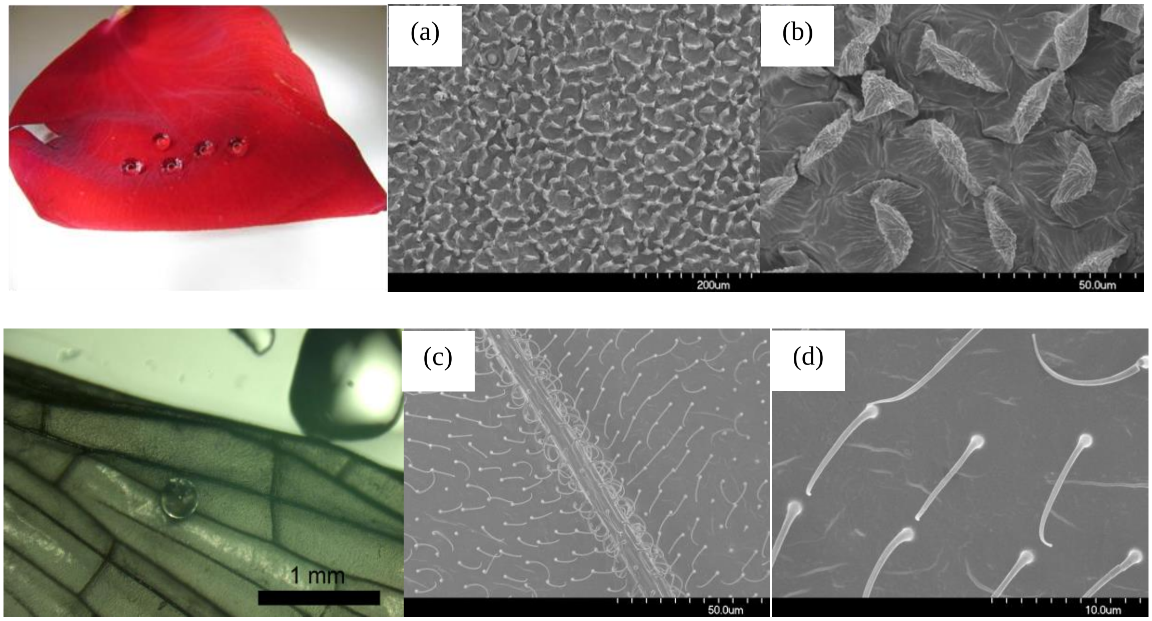

Figure 1.2 SEM images of: (Top) Rose petal (Bottom) Flying ant wing
(a-b) SEM images of Rose petal (c-d) SEM images of flying ant wing. Reproduced from Zhang *et al* with permission from © IOP Publishing [3]

Extensive experimental and theoretical studies on wetting behavior of micro/nano structures are attracting interest throughout recent years. The ability to tune a surface's wetting properties based on artificial engineered surface structures provides possibilities for varies industrial applications [5-13]. A number of previous studies [4, 14, 15] showed that bio-inspired micro- and nano-hybrid structures can create super-hydrophobic surfaces. Highly fluorinated monomer/polymers have been widely used to improve the hydrophobicity of surfaces utilizing low surface energy properties. Fluorinated polymers such as polytetrafluoroethylene, PTFE [16, 17], and others [18] can dramatically reduce the wettability of the surface. Recently, new techniques such as electromechanical systems were used to fabricate super-hydrophobic surfaces for applications in anti-bio fouling, corrosion, steam condensation, and flow control.

In order to overcome the typical FWC of plain metal tubes, DWC must be promoted through surface treatments. Early surface treatment methods involved the use of an organic promoter to foster DWC [19, 20], and later developed into more complex coatings. Blackman *et al.*, [21] determined that the two critical characteristics of a successful coating compound consists of a hydrophobic group and a chemical group with a high affinity for the metal. To achieve these characteristics, a number of methods have been employed. These methods include nanostructure in polymer matrix [18] and Self-Assembled Monolayers (SAMs) of organic material [22, 23].

Organic materials like hydrocarbons and polyvinylidene chloride coatings received considerable attention for their hydrophobic capabilities in promoting DWC [24]. Carbon Nanotubes (CNT) based DWC promoters have also been considered [16, 18]. Using micromachining, CNTs were combined to create a surface emulating that of the lotus leaf like structures. This structure promotes not only DWC, but the desired “Cassie type” drop state as well. “Cassie type” drop state is when liquid/solid interfacial area is kept at minimum, i.e. droplet only sits on top of surface structures. This type of wetting reduces contact angle hysteresis and increases mobility, both desirable traits for a DWC promoting surface. Das *et al.*, [25] used organic SAMs as a DWC promoter for horizontal tubes and carried out condensation experiments with number of different samples. Erb and Thelen [26] used coatings of inorganic compounds such as metal sulfides and found that a sample of sulfide silver on mild steel showed excellent DWC. Although each of these methods showed some degrees of success at promoting DWC, the durability of each promoter comes into a question when industrial conditions are considered.

Interesting wetting characteristics are shown with advancement of micro/nano structured surfaces. In order to fully implement these technologies for industrial usage, one must first understand the relationships between surface morphology and condensation heat transfer. Impact on condensation heat transfer with different surface morphology along with coating thickness would be examined in this study.

1.2 Surface energy and surface morphology

Condensation drop distribution is one of the most important factors in DWC heat transfer [27, 28]. Drop dynamic behavior should be the first to be considered in developing models to predict DWC condensation heat transfer. Contact angle hysteresis of liquid droplet on a surface is responsible for determining maximum drop sizes [29]. Contact angle hysteresis (CAH) is often defined as the difference between advancing and receding angle on an incline surface [30] as shown in Figure 1.3. Increase CAH would lead to large droplet sizes in DWC, thus thermal resistance in condensation heat transfer is increased.

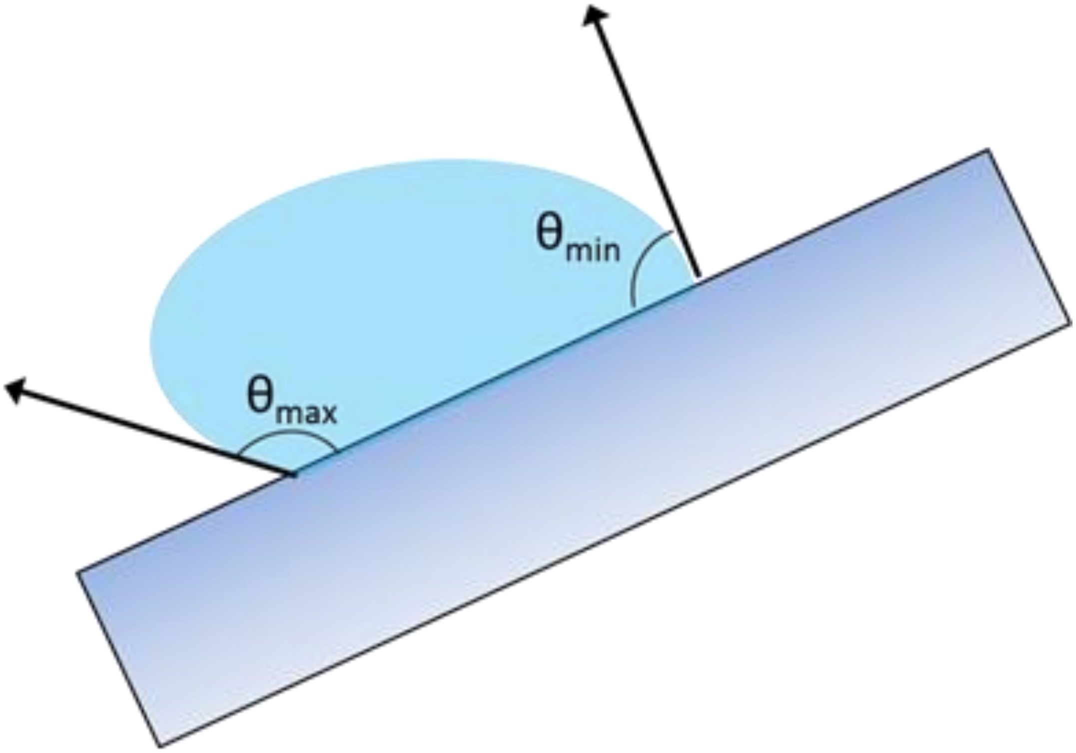

Figure 1.3 Advancing and receding contact angles on a surface

CAH has been the subject of research both in experiments and theoretical models. CAH in relations to surface roughness is first explained by Johnson [31]. There have been advances in understanding relationships between CAH and surface structure in recent researches in experimental side [17, 30, 32, 33]. Micro structured surfaces are often fabricated using known contact angles on flat surfaces in experimental studies [32]. Forsberg *et al.,* [32] fabricated micro structured surface using varies polymers with known flat surface contact angles. It was found that cosine of CAH results with these structured surfaces are linearly correlated with aspect ratios and fin densities. It was also found that CAH increased with surface with higher fin heights with increased roughness in Forsberg's work [32].

Most of the model deals with dynamic wetting behavior of liquid drops on rough surfaces [33-36]. There are few proposed models to estimate CAH [33, 35]. In order to understand CAH, thermodynamics of such droplet on the surfaces need to be understood [31]. Gibbs free energy, E, provided relations between surface energies in terms of interfacial contact areas and their perspective surface energies as shown in Equation (1.1),

$$E = A_{LG}\gamma_{LG} + A_{SL}\gamma_{SL} + A_{SG}\gamma_{SG} \tag{1.1}$$

where, A_{LG}, A_{SL}, A_{SG} are liquid/gas, solid/liquid, and solid/gas interfacial areas, respectively and γ_{LG}, γ_{SL}, γ_{SG} are the corresponding surface energies per unit area. Of the CAH models proposed, many of them involve complicated numerical simulations schemes [31]. These models give details on how a drop behaves under certain situations and matches well with experimental data. However they are difficult to use as design tools, especially in heat transfer applications. Several analytic models [30, 33, 37, 38] utilized concepts of surface energy minimization process which were first proposed by Young in 1800s. Results from these analytical models predict CAH with relative accuracy. However, CAH models have yet to be incorporated into DWC heat transfer models as designing tools for most industrial applications. CAH model based on surface energy minimization are included in this work. This model will examine,

1. Impacts on CAH in terms of varying degrees surface roughness,
2. Relationships between surface energies and CAH, and
3. Potential impact of CAH in DWC heat transfer.

1.3 Experimental approaches

Experimental studies were conducted to verify effects on condensation heat transfer with different surface morphologies and structured geometries. Surface morphologies of varies surfaces were examined by using a scanning electron microscope, and wetting behaviors are determined by contact angle measurements with respective surface geometries. Condensation heat transfer experiments were carried out to verify heat transfer model results for DWC and other imaging techniques were also employed to examined effects on drop sizes and distributions with varies surfaces.

1.4 Research goals and objectives

The goals of this project are i) to gain fundamental understanding of wetting characteristics on textured surface, ii) to find the relationship between wetting and drop size distribution in condensation environments, and iii) to determine how different surface morphologies and wetting impact condensation heat transfer. Both theoretical and experimental studies are employed in this study to further advance understanding of wetting in textured surface and how it influence condensation heat transfer. Direct correlations of surface geometries, wetting and condensation heat transfer are explored in this project and coating textures could be designed for improving condensation heat transfer. Surface geometries and wetting characteristics parameters are to be optimized in future studies with results found in this project.

Objectives are set in this study in order to achieve the project goals. They are as follows,

1. Develop drop dynamic model in order to estimate CAH,
2. Incorporate drop dynamic model into DWC heat transfer model to explore drop dynamics on condensation heat transfer,
3. Fabricate different coatings with different surface morphologies and test each coating in condensation experimental studies,
4. Verify effectiveness of mathematical model with experimental results.

1.5 Project tasks

Parametric studies on textured surfaces with various surface geometries, and wetting, and other contributing parameters, e.g. coating thickness and thermal conductance are the main focus in this project. Theoretical and experimental studies were conducted to accomplish this goal.

Task 1: A single drop dynamic model was developed to predict drop wetting behaviors based on theories of surface energies on different surface geometries. The modeling results can be used to estimate CAH and its impact on DWC heat transfer.

Task 2: Condensation heat transfer modeling was studied in this project. Condensation heat transfer coefficient and heat fluxes are examined with varying wetting characteristics for textured surfaces.

Task 3: Different surface coatings were fabricated. Different surface morphologies were examined with scanning electron microscopes and other visual techniques. Contact angle measurements were used to study wetting characteristic for varies coatings.

Task 4: Condensation experiments were taken place to examined heat transfer behaviors for different textured surfaces. Heat transfer coefficients were compared with the results from condensation heat transfer models. Visual studies for condensation with different textured surfaces were done with direct observation via imaging techniques.

Task 5: Drop distribution studies were followed with single drop modeling. Relationship between single drop dynamic and collective population behavior was explored. Preliminary studies were to provide details on future drop dynamic and drop sizes distribution researches.

2. Literature Survey

2.1. Surface wetting and drop dynamic

Wetting behaviors of droplets on surface should be first understood in order to understand how condensation heat transfer works. It is important to understand how a single drop on a surface would behave. Wetting properties of a single droplet strongly influence the drop size distribution in condensation heat transfer [39, 40].

According to Young [41], the liquid droplet shape would be determined by surface tensions of interfacial forces. Liquid droplets will attempt to spread through evenly on the wetting surface and the act of spreading is stopped when all interfacial tension forces are balanced, i.e. liquid/solid, solid/gas, liquid/gas. Liquid droplet would form a unique angle with the solid surface as shown in Figure 2.1.

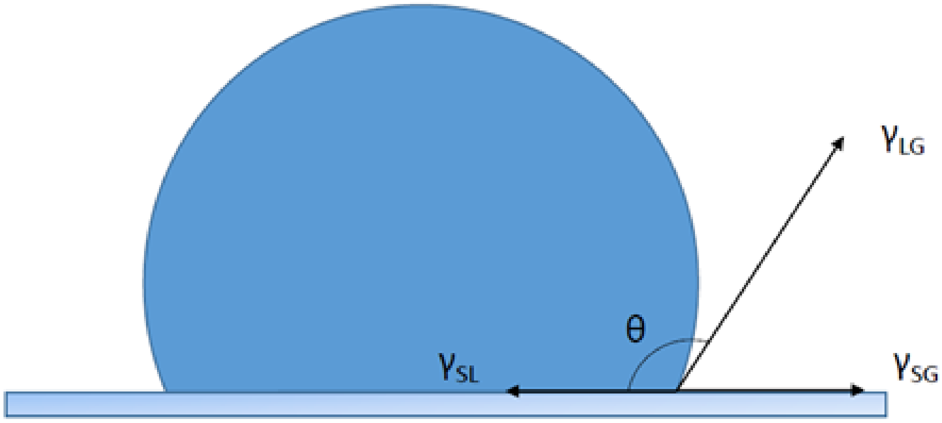

Figure 2.1 Surface tension and contact angle

Young's Equation for contact angle is obtained by force balance, as given in Equation (2.1),

$$\gamma_{LG} \cos\theta = \gamma_{SG} - \gamma_{SL} \tag{2.1}$$

Similarly, Equation (2.1) can be obtained by minimizing surface energies with respect to interfacial area given in Equation (1.1) and seen in Equation (2.2),

$$dE = 0 = dA_{LG}\gamma_{LG} + dA_{SL}\gamma_{SL} + dA_{SG}\gamma_{SG} \tag{2.2}$$

The Young's Equation gives important insight to how a drop would behave on a static homogeneous surface. However, it does not give information on how a drop would behave under external influence or drop shape in non-homogeneous surface [42] .

Theoretical and experimental approaches were conducted in drop dynamics with relationship with surface energy are ongoing research subjects. In recent years, the advance in nano-material research enable super-hydrophobic and other interesting wetting properties [5, 11, 33, 35, 38, 43-50]. Non-homogeneous surfaces are often presented in the studies on super-hydrophobic surfaces and other complex morphologies that produce complex wetting characteristics. In the early studies, researchers begin the notion of incorporating roughness in consideration of properties in wetting such as contact angles. While Young's Equation gives insight only on basic information on wetting on flat surface, it has been bases of wetting models [8, 35, 36, 38, 51, 52]. Notably, Wenzel [52] was one of the first to examine wetting on rough surfaces. Wenzel established relationship between roughness ratio (area of rough surface to area of projected flat surface) and contact angles and establish the following Equation in homogeneous wetting condition,

$$\cos\theta_W = r_f \cos\theta_0 \tag{2.3}$$

where r_f, θ_W, and θ_0 are the roughness ratio, Wenzel contact angle and Young's flat surface contact angle, respectively.

Later, Cassie and Baxter [51] establish contact angles in relationship with non-homogeneous condition as it takes into account of weighted average of different contact angles for different components,

$$\cos\theta_{CB} = \phi\cos\theta_1 + (1-\phi)\cos\theta_2 \tag{2.4}$$

where θ_1, θ_2, and ϕ are contact angle of component 1 and component 2 and solid/liquid contact area fraction.

Both Wenzel and Cassie models give some insights on wetting characteristics in rough surface. They still did not fully encompass how wetting characteristic would change under external influence, i.e. external forces.

Contact angle hysteresis (CAH) should be the first topic to be studied for drop dynamics. Models has been proposed to explain how wetting would change with respect to CAH. In order to initiate motion of drop on a surface, movement of a droplet is cause by external forces from the environments as explained in Gao and McCathy *et al* [30]. External force would deform the shape of a droplet and causes an observable difference in contact angle measurement. Contact angle hysteresis (CAH) is defined as the difference between the maximum and minimum contact angle. CAH could be caused by addition or subtraction of droplet masses or by tilting contact surface at an angle. It is very important to understand how CAH is initiated, thus it influence droplet sizes distribution in DWC heat transfer directly. CAH could be measure experimentally in several ways [53]. The most common ways are addition and drawing of liquid droplet mass to measure immediate advancing and receding angles or to measure droplet advancing and receding angles on a titled surface. These methods may have large variations and does not always represent accurate operating conditions on rough surfaces. Ongoing experimental and theoretical works are being conducted in order to understand topics on CAH. Quere *et al.,* [54] reviewed how roughness are related to surface energies and wetting characteristics. Young's Equation and the associate Gibbs energy Equation (see Equation 2.2) were reviewed and were adapted to different roughness and geometries. Since wetting dynamics depends of concepts of surface tension and surface energy, Gibbs energy continues to be used in varies wetting dynamic models, especially in CAH.

Most recently, Hejazi *et al.,* [37] proposed a multiphase model to describe contact angle hysteresis for system with multiple wetting components. Similar to Wenzel and Cassie-Baxter model, then Hejazi describe wetting under multi-phase surface energies. Rough surfaces were idealized as flat surface with different components with different wetting properties. The models also consider several geometries factors such as component spacing. The modeling results for CAH were found to agree well with solid/water/air and solid/water/oil systems. Since contact angle hysteresis is caused by additional energy applies in the system, Adam and Jessop [55] proposed that the additional energy is proportional to the forces with CAH,

$$F = \gamma(\cos\theta_{red} - \cos\theta_{adv}) \tag{2.5}$$

Similar models [56, 57] have explored contact angles and CAH with the roughness contribution. It was found that the effect of roughness is similar to having different components as in Cassie-Baxter models.

Xu and Wang *et al.,* [58] modified the Cassie-Baster Equation and simulate contact line movements with different patterns of wetting components arrangements. It was found that the classic Cassie-Baxter Equation works relatively well when different components are homogenously dispersed. However, contact line movement and CAH is highly depended on wetting components arrangements.

Moradi *et al.,* [33] examined geometry effect on spreading and CAH. Moradi modeled surface as parabolic cones and modeled how a drop would spread on the surface depended on geometries of the cones. Model results were compared with treated stainless steel plates with similar cone geometries on surface morphologies. It was found that CAH is highest with cones with high pillar height.

Other models [37, 38, 58-61] continued to modify the Wenzel and Cassie-Baxter drop models. Mchale *et al.,* [38] examined the limitation of the two models. The two models describe good trends of surface wetting in most cases. However, Wenzel and Cassie-Baxter models could potentially ignore factors such as geometries and could not be used above certain ranges, e.g. Wenzel model on super-hydrophobic surface.

Geometries factors along with local wetting properties in surface morphologies are found to be very important in recent researches. Wettability could be tuned by changing surface geometries with the same materials [33, 43, 62-65]. In studies with nano-structured surface morphologies, relationships between wettability and geometry factors continued to be subject of interest in regard of drop dynamics.

2.2 Condensation heat transfer

Dropwise condensation is capable of producing heat transfer coefficients up to 20 times those of filmwise condensation [1, 66]. Vapor condenses into individual droplet in DWC as contrast to forming a continuous film on the surface. Figure 2.2 illustrate FWC and DWC mechanism.

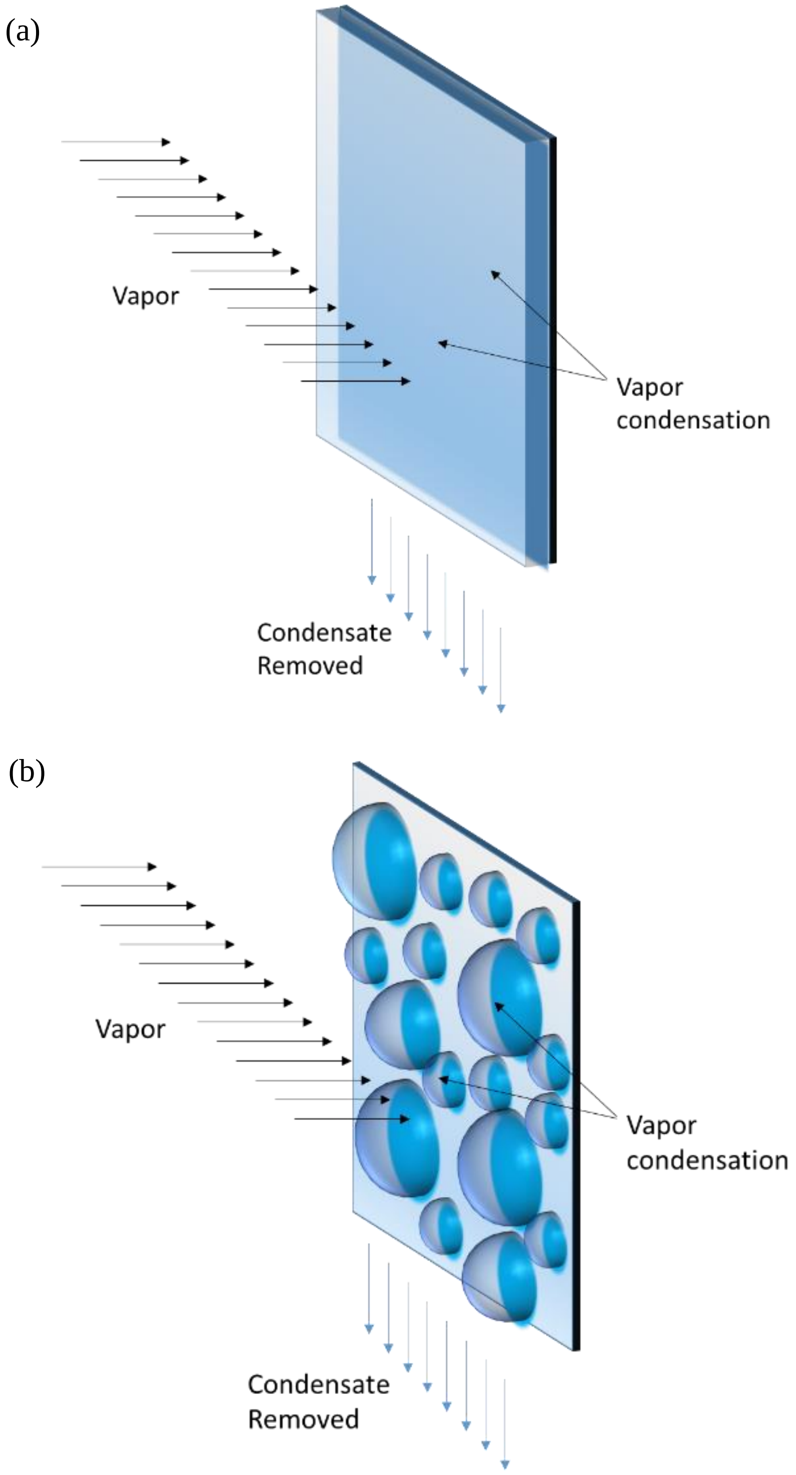

Figure 2.2 Condensation of vapor on surface (a) filmwise Condensation and (b) dropwise condensation

However, long term DWC conditions are difficult to maintain. To overcome the typical FWC of plain metal tubes, DWC must be promoted through a surface treatment of some sort. Early methods involved the use of an organic promoter to foster DWC [19, 20], though these surface treatments soon developed into more complex coatings. Blackman *et al.,* [21] determined that the two critical characteristics of a successful coating compound to be as follows:

- A hydrophobic group
- A chemical group with a high affinity for the metal used

To achieve these characteristics, a number of methods have been employed including:

- Self-assembled monolayers (SAM) of organic material [22, 23, 67]
- The application of thin layers of noble metals [68-73]
- And more recently, nano-structure in polymer matrix [18]

Although each of these methods showed degrees of success in promoting DWC, the durability of each promoter comes into question when industrial conditions are considered.

Many early coatings eroded as steam condensed, washing the promoter from the tube surface [19, 20]. The thin noble metal coatings were shown to be promoting DWC due to organic brighteners that remained from the plating process [27, 74]. Ion implanted surfaces were sensitive to more rugged industrial installation procedures, such as high temperature brazing and welding processes [75]. In order to reduce thermal resistances, extremely low thicknesses are required in polymer based coatings, and hence are susceptible to scratches and other durability issues.

Ma *et al.*, [28] used an ion-implemented coating and showed that the coatings increased the condensation heat transfer coefficient by a factor of 4-15. Das *et al.*, [25]was the first research group to use organic self-assembled monolayers (SAMs) as a DWC promoter. Using horizontal tubes, Das and co-workers carried out condensation experiments with a number of different samples. A bare aluminum tube was used as an FWC control, and a bare gold plated aluminum/titanium tube was used as an SAM free sample. Three tubes had SAM coatings applied; where the three different substrates were gold coated aluminum, copper, and copper nickel. All of the SAM tubes produced DWC at atmospheric and vacuum conditions, with an enhancement as compared to the FWC control. At atmospheric pressure conditions, this enhancement ranged from 4 times FWC for the SAM-on-gold-coated aluminum tube, to 15 times FWC for the SAM-on-copper tube. In this experiment, non-condensable gases were assumed to not be present in significant amounts due to the vapor velocity of the steam around the condensing tube. According to visual observations, all SAM coated surfaces showed smaller drops on their surfaces, though significantly larger drops were found on the top and bottom surfaces of the tubes. As large drops descended from the surface, the small drops on the side were swept away. According to Das's hypothesis, variations in the enhancement of heat transfer may originate due to the roughness of the substrate surface prior to coating, the surface chemistry of the SAM-metal bond, and the thermal conductivity of the substrate. Further investigations are recommended for clarification. It must be mentioned that the durability of the coated surfaces had not been determined. In general, organic coatings are difficult to maintain and require strong, long term adhesion forces between the coating and the metal substrate. Erb and Thelen [26] used coatings of inorganic compounds such as metal sulfides and found that a sample of sulfided silver on mild steel showed excellent dropwise condensation.

Extensive studies were made by researchers on condensation by using noble metal plated surfaces. Noble metal plated surfaces have consistently showed excellent dropwise characteristics [26, 74]. Erb wrote a collection of papers proposing the pursuit of noble metals for use in the desalination. His initial work [73] demonstrates that water would form high contact angles on certain metal surfaces, in particular gold, silver, rhodium, palladium, and platinum. DWC initially formed on all of the surfaces and was demonstrated to be sustainable on gold, silver and rhodium for up to 2 weeks. Erb attributed the wettability of other metals under condensing conditions to the formation of oxide films on the surfaces. Additional research by Erb [72] indicated that DWC sustained on gold, palladium, and rhodium surfaces for more than 10,000 hours of continuous condensation. Condensation rate increases of up to 90% were shown for a palladium coated Cu-Ni alloy tube versus a bare Cu-Ni alloy tube.

Building upon the work done by Erb, Woodruff and Westwater [69] examined the necessary thickness of a gold electroplated coating to promote DWC. The results of the study show that at least effectively coated layers of gold must be deposited to affect the condensation of steam on the surface. The condensing heat transfer enhancement of seven times than FWC was reported. The author made no comment about the presence of organic material on the condensing surface. However, the hydrophobic characteristics of these noble metals as DWC promoters have been controversial in the literature [71]. Wilkins *et al* [74] reported that pure gold will produce FWC when organic contaminants are absent. Furthermore, the cost of manufacturing such surfaces has limited their applications.

Organic materials [24, 76, 77] like hydrocarbons and polyvinylidene chloride coatings also received considerable attention for their hydrophobic capabilities in promoting DWC. Carbon nanotubes (CNT) based DWC promoters have been considered, beginning with a publication by Chen *et al.,* [78]. Using micromachining, carbon nanotubes were combined to create a surface emulating that of the lotus leaf. This structure promotes not only DWC, but the desired Cassie type drop state as well. This type of wetting reduces contact angle hysteresis and increases mobility, both desirable traits for a DWC promoting surface. Many researchers [24, 76, 77] have used different types of technologies to employ polymer coatings for promoting DWC and reported that heat transfer enhancements were up to 30 times higher than film condensation.

Most recent researches focus concentrate on how wettability could be tuned with surface geometries and other parameters, e.g. temperature, materials. Chu *et al.,* [79] examined the effect of symmetries of nano-structured surface on surface wettability and liquid spreading. It was found that changing geometries symmetries could change liquid spreading directions. Miljkovic *et al.,* [80] developed spike-liked nano-structured surface on condenser tube. It was found that heat fluxes was improved by 25 % comparing to plain surface and rapid drop renewal was also improved. Adera *et al.,* [81] introduced super-hydrophilic textured surface and it was found that wettability could be tuned by varying surface temperatures. Humplik *et al.,* [82] introduced super-hydrophilic porous textured surface and it was found that liquid mobility on the surface was enhanced. Miljkovic *et al.,* [83] introduce nano-spiked textured onto condenser surface and applied electric field to the system. It was found that external electric field further enhance anti-wetting properties in condensation environments.

In order to examined DWC promoters and parameter studies on wetting characteristics, varies surface coatings from different fabrication techniques would be manufactured. Condensation heat transfer results would be compared to heat transfer models. Direct observational studies in condensation would also be conducted at the same time.

3. Modeling Perspective

3.1 Modeling rationale

Drop dynamic model and heat transfer model were developed in this project. Drop dynamic model were developed according to principles of surface energies minimization, and the principles were first proposed by Young [41]. Heat transfer modeling was modified from drop distribution and heat transfer model by Kim *et al* [40]. Contact angle hysteresis results found in drop dynamic model were integrated into drop distribution and heat flux calculations into Kim's model. Sweeping period in Kim's model was also modified to accommodate the differences between varies drop sizes.

3.2 Single drop dynamic modeling in relation to surface energy

For a liquid droplet to be stable on surface, surface energies between interfaces between solid, liquid, and gas are to be minimized with the perspective interfacial areas [41].

$$E = A_{LG}\gamma_{LG} + A_{SL}\gamma_{SL} + A_{SG}\gamma_{SG} \tag{3.1}$$

$$dE = 0 = dA_{LG}\gamma_{LG} + dA_{SL}\gamma_{SL} + dA_{SG}\gamma_{SG} \tag{3.2}$$

E is surface energies of all interfaces. A_{LG}, A_{SL}, A_{SG} are liquid/gas, solid/liquid, and solid/gas interfacial areas and γ_{LG}, γ_{SL}, γ_{SG} are the corresponding surface energies per unit area. Figure 3.1 illustrate surface energies of a drop on a surface.

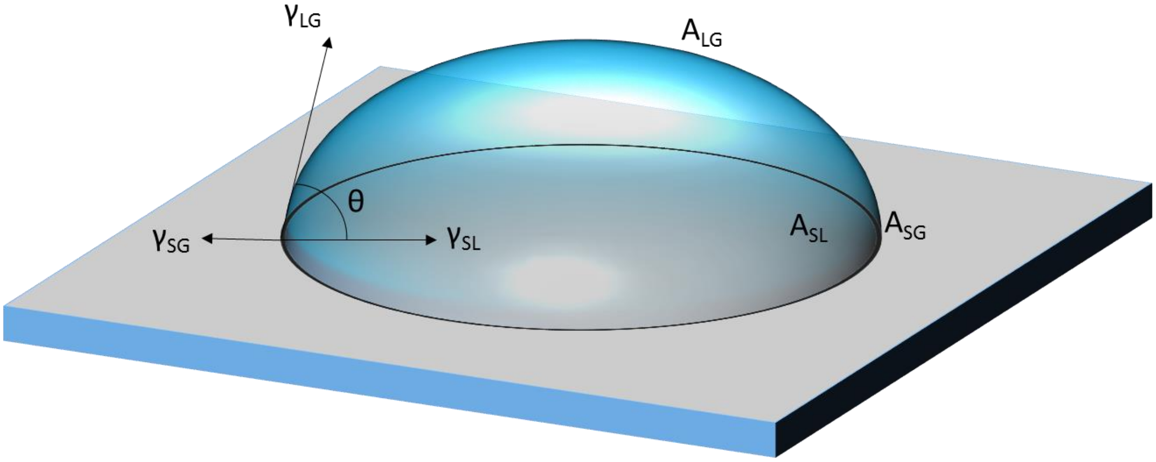

Figure 3.1 Surface energies of a single drop

Assuming droplet resting on a surface is a spherical cap with drop radius, R and contact angle θ. Drop volume, V (assume constant drop volume), cap surface area, A_C are given as,

$$V = \frac{\pi}{3} R^3 [2 - 3\cos\theta + \cos^3\theta] \tag{3.3}$$

$$A_C = A_{LG} = 2\pi R^2 (1 - \cos\theta) \tag{3.4}$$

Solid/gas surface energy, γ_{SG}, is responsible spreading the drop while Solid/liquid energy, γ_{SL}, is responsible for keeping the drop together. Area of both interfaces should be the same with opposite signs, i.e. A_{SL} = -A_{SG}. The projected base area, A_P is given by,

$$A_P = A_{SL} = -A_{SG} = \pi R^2 \sin^2\theta \tag{3.5}$$

Equations (3.1) and (3.2) could be re-written as,

$$E = A_{LG}\gamma_{LG} + A_{SL}(\gamma_{SL} - \gamma_{SG}) \tag{3.6}$$

$$dE = 0 = \frac{dA_{LG}}{dA_{SL}}\gamma_{LG} + (\gamma_{SL} - \gamma_{SG}) \tag{3.7}$$

Applying conditions from Equations (3.3) to (3.7), Young's Equation is obtained from minimizing surface energy with respect to contact areas for flat surface with young's contact angle, θ_0,

$$\gamma_{SG} = \gamma_{SL} + \gamma_{LG}\cos\theta_0 \tag{3.8}$$

As a result, Young's Equation states that forces are acting in equilibrium on the contact line of the triple interfaces of solid, liquid and gas.

Assuming a constant volume, drop radius R could be written in V and θ. So that surface energy depends only on contact angle. Surface energy for a flat surface is given as,

$$E = \gamma[A_C - \cos\theta_0\, A_P)] \tag{3.9}$$

For convenient, solid liquid interfacial area, Liquid/gas surface energy is equivalent to surface tension of a liquid, γ_{LG} and it is replaced with simply γ. Liquid/gas interfacial area A_{LG}, is replaced with A_C. A_{SL} of flat surface is set to be projected flat surface area of the cap, A_P for any contact angel θ.

In case of textured surfaces, extra parameters are needed to describe surface geometries in wetting. Roughness parameter, r_f and ϕ is introduced for rough surfaces. r_f is the ratio of actual area to projection area, and ϕ is ratio of top surface area to projection area. This could be seen in an idealized situation where rough surface could be seen as pillars extending from the surface as seen in Figure 3.2.

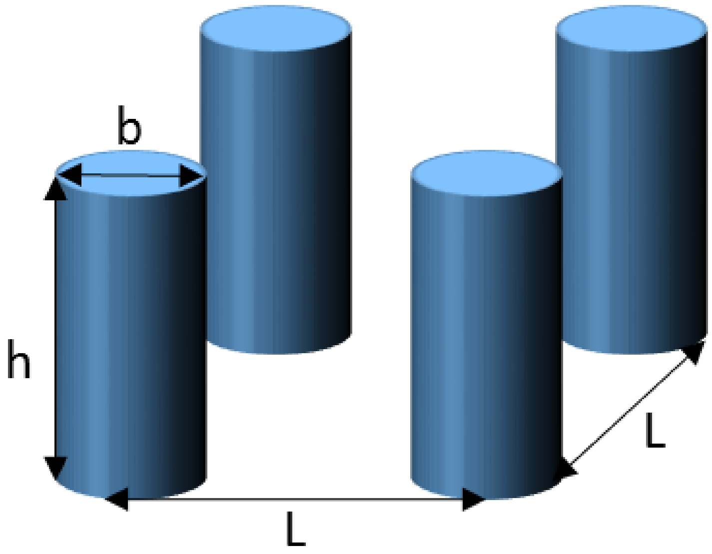

Figure 3.2 Idealized surface roughness representation, where *b* is the diameter, *h* is the height, and *L* is the center-to-center separation distance

L, *b*, and *h* represent pillar to pillar distance, diameter of cylinder top and height of pillars. In this representation, r_f and ϕ can be presented as following,

$$r_f = 1 + \frac{\pi b h}{L^2} \tag{3.10}$$

$$\phi = \frac{\pi b^2}{4L^2} \tag{3.11}$$

Surface energy of droplet should be found for evaluating an equilibrium contact angle in textured surface as shown in Figure 3.3.

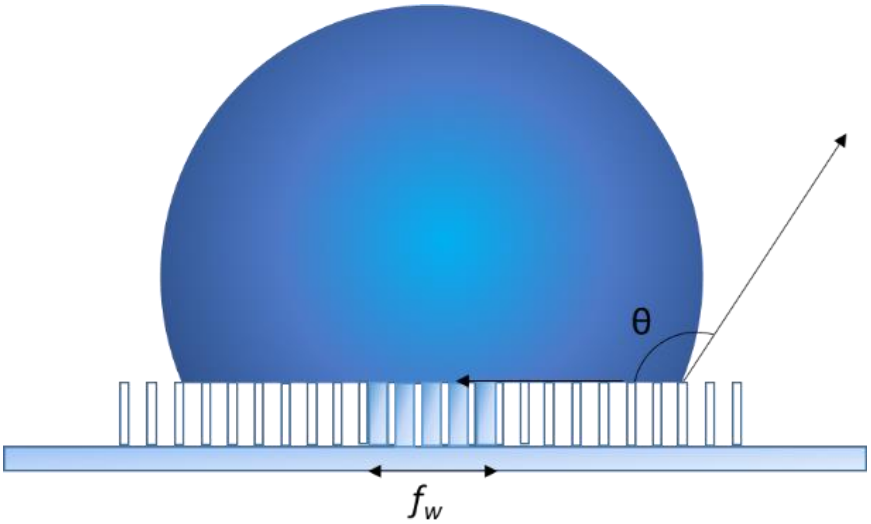

Figure 3.3 Wetting representation on textured surface

Fraction of liquid could penetrate the spaces between the pillars when liquid droplet rest on rough surface and starts to spread. There needs a way to represent this phenomenal in order to represent all wetting conditions on rough surface. f_w is introduced as the projected area fraction for wetting space, where it is between 0 and 1. Cassie-Baxter state is achieved if f_w is 0, and Wenzel state is achieved if f_w is 1 as shown in Figure 3.3.

Interfacial areas for liquid/gas, solid/liquid and solid/gas should be found in order to determine surface energy for partially wetted textured surface. Liquid/gas area, A_{LG}, solid/liquid area, A_{SL}, and solid/gas area, A_{SG}, with given geometry parameters Equations (3.12) and (3.13).

$$A_{LG} = 2\pi R^2(1-\cos\theta) + (1-f_w)(1-\phi)\pi R^2 \sin^2\theta \tag{3.12}$$

$$A_{SG} = -A_{SL} = \left[r_f f_w + \phi(1-f_w)\right](\pi R^2 \sin^2\theta) \tag{3.13}$$

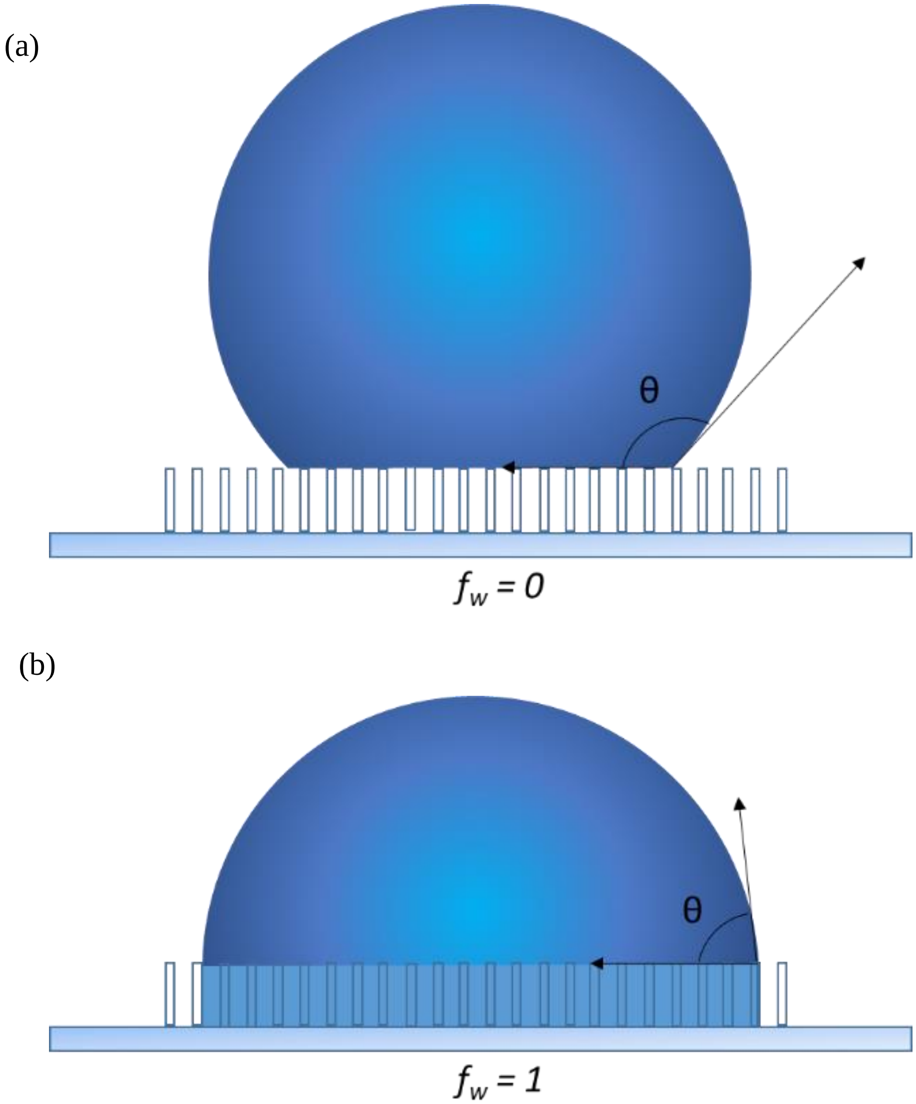

Figure 3.4 Droplet with different wetting conditions (a) Cassie-Baxter state (b) Wenzel State

Substitute Equations (3.4) and (3.5) for droplet cap and projection area, A_C and A_P to Equations (3.12) and (3.13),

$$A_{LG} = A_C + (1 - f_w)(1 - \phi)A_P \tag{3.14}$$

$$A_{SG} = -A_{SL} = \left[r_f f_w + \phi(1 - f_w)\right]A_P \tag{3.15}$$

Substitute Equations (3.14) and (3.15) to Equation (3.6) and surface energy becomes,

$$E = [A_C + (1 - f_w)(1 - \phi)A_P]\gamma_{LG} + \left\{\left[r_f f_w + \phi(1 - f_w)\right]A_P\right\}(\gamma_{SL} - \gamma_{SG}) \tag{3.16}$$

Using results for Young's contact angle from Equation (3.8) and substitute into Equation (3.16),

$$E = \gamma\left[A_C - A_P\left(\left[r_f f_w + \phi(1 - f_w)\right]\cos\theta_0 - (1 - f_w)(1 - \phi)\right)\right] \tag{3.17}$$

$$A_C = 2\pi R^2(1 - \cos\theta)\ and\ A_P = \pi R^2 \sin^2\theta$$

An equilibrium contact angle would be achieved when surface energy is minimized and differential of Energy with respect to contact angle would be zero,

$$\frac{dE}{d\theta} = 0 = \gamma\left[\frac{dA_C}{d\theta} - \frac{dA_P}{d\theta}\left(\left[r_f f_w + \phi(1 - f_w)\right]\cos\theta_0 - (1 - f_w)(1 - \phi)\right)\right] \tag{3.18}$$

Divide both sides by γ and $dA_P/d\theta$, Equation (3.18) becomes,

$$\left(\frac{dA_C}{d\theta}\right)/\left(\frac{dA_P}{d\theta}\right) = \left[r_f f_w + \phi(1 - f_w)\right]\cos\theta_0 - (1 - f_w)(1 - \phi) \tag{3.19}$$

By simplifying left hand side of Equation (3.19), equilibrium angle, θ_E for partially wetted textured surface is given as,

$$\cos\theta_E = \left[r_f f_w + \phi(1 - f_w)\right]\cos\theta_0 - (1 - f_w)(1 - \phi) \tag{3.20}$$

If no liquid is penetrated into spaces between the structures, then $f_w = 0$, and Cassie-Baxter Equation is extracted from Equation (3.20),

$$\cos\theta_E = \phi\cos\theta_0 - (1-\phi) \tag{3.21}$$

If spaces between structures are fully wetted, then $f_w = 1$, Wenzel's Equation is extracted from Equation (3.20),

$$\cos\theta_E = r_f\cos\theta_0 \tag{3.22}$$

Equilibrium angle on textured surface could be found with given geometries, contact angle on flat surface and degrees of wetting on rough surface from Equation (3.20).

3.3 Contact angle hysteresis and wetting characteristics

Contact angle hysteresis occurs while an external force acts on droplet. This could be view as an extra energy acting on the system. This extra energy is included as an extra term in the surface energy Equation.

$$E = E_{drop} + E_{hys} \tag{3.23}$$

Hysteresis energy E_{hys}, is acting on the triple phase contact line between solid/liquid/gas as shown in Figure 3.5.

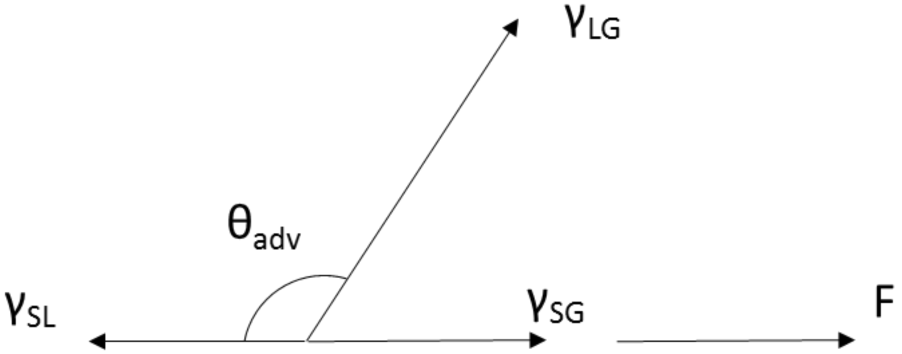

Figure 3.5 Hysteresis energy act on triple phase contact line

It is assumed that line force *F* acts parallel to the wetting surface and should be a minimum force required for triple phase contact line to move. Line force *F* is proportional to the difference between equilibrium angle and advancing/receding angle. In case of advancing angle, it should be written as,

$$F = \gamma(\cos\theta_E - \cos\theta) \tag{3.24}$$

Hysteresis energy is acting on solid/gas and solid/liquid interfacial area for a contact line to move parallel to the wetting surface. Hysteresis energy could be written as,

$$E_{hys} = \gamma(\cos\theta_E - \cos\theta)\left[r_f f_w + \phi(1 - f_w)\right]A_P = F * T_2 \tag{3.25}$$

$$F = \gamma(\cos\theta_E - \cos\theta)$$

$$T_2 = \left[r_f f_w + \phi(1 - f_w)\right]A_P$$

F represents line force with differences on cosine of equilibrium and maximum contact angles. T_2 represents contact areas underneath the drop. Substitute Equations (3.17) and (3.25) to (3.23),

$$E = \gamma\{A_C - A_P D_1\} \tag{3.26}$$

$$D_1 = \left[r_f f_w + \phi(1 - f_w)\right]\left(\cos\theta_0 + (\cos\theta_E - \cos\theta)\right) - (1 - f_w)(1 - \phi)$$

Take $dE/d\theta = 0$ in Equation (3.26) to find max/min angles,

$$\frac{dE}{d\theta} = 0 = \gamma\left\{\frac{dA_C}{d\theta} - \left(\frac{dA_P}{d\theta}\right)K - A_P\left(\frac{dK}{d\theta}\right)\right\} \tag{3.27}$$

$$K_1 = \left[r_f f_w + \phi(1 - f_w)\right]\left(\cos\theta_0 + (\cos\theta_E - \cos\theta)\right) - (1 - f_w)(1 - \phi)$$

Divide Equation (3.27) by $dA_P/d\theta$, and γ,

$$0 = \frac{dA_C/d\theta}{dA_P/d\theta} - K_1 - \frac{A_P}{dA_P/d\theta}\left(\frac{dK_1}{d\theta}\right) \tag{3.28}$$

$$\frac{dA_C/d\theta}{dA_P/d\theta} = \cos\theta$$

$$K_1 = \left[r_f f_w + \phi(1 - f_w)\right](\cos\theta_0 + (\cos\theta_E - \cos\theta)) - (1 - f_w)(1 - \phi)$$

$$A_P = \pi R^2 \sin^2\theta\,, \frac{dA_P}{d\theta} = 2\pi R\left(\frac{dR}{d\theta}\right)\sin^2\theta + 2\pi R^2 \sin\theta\cos\theta$$

$$= 2\pi R\sin\theta\left(\frac{dR}{d\theta}\sin\theta + R\cos\theta\right)$$

$$R = \left(\frac{3V}{\pi}\right)^{\frac{1}{3}}\left[2 - 3\cos\theta + \cos^3\theta\right]^{-\frac{1}{3}}, \frac{dR}{d\theta} = -\left(\frac{3V}{\pi}\right)^{\frac{1}{3}}\sin^3\theta\,(2 - 3\cos\theta + \cos^3\theta)^{-\frac{4}{3}}$$

$$\frac{dK_1}{d\theta} = 2\left[r_f f_w + \phi(1 - f_w)\right]\sin\theta$$

Simplify Equation (3.28) and obtain,

$$\cos\theta = \left(f_w\left(r_f - \phi\right) + \phi\right)C_1 - (1 - f_w)(1 - \phi) \tag{3.29}$$

$$C_1 = \cos\theta_0 + \cos\theta_E - \cos\theta + \frac{1}{2}\sin^2\theta\,(\cos\theta + 2)$$

Max/min angles could be solved with Equation (3.29) for known surface geometries and Young’s contact angle.

3.4 Single drop dynamic modeling results and discussion

From Equations (3.10) and (3.11), roughness factor r_f and top area projection factor ϕ is idealized as cylinders on flat surface as a model study. Surface energy profile given in (3.17) can change with varying pillar geometries and spacing. Changes in surface energy profiles in relations to varying contact angles are shown in Figure 3.6 for young's contact angle, $\theta_0 = 60°$, $\theta_0 = 90°$ and $\theta_0 = 120°$ for different f_w values as surface geometries are set at $b = 1 \mu m$, $h = 2 \mu m$, and $L = 3 \mu m$.

CAH can be affected by surface geometry factors as well as ratio of fully wetted area. Figure 3.7 demonstrate how CAH can be changed with varying fully wetted projected area ratio with different pillar height, $h = 0.5 \mu m, 1 \mu m, 2 \mu m$, while b and L are fixed at $1 \mu m$ and $3 \mu m$. Figure 3.8 shows how CAH depends on changing local flat surface contact angle with different wetting condition. Surface geometries are fixed at $b = 1 \mu m$, $h = 2 \mu m$ and $L = 3 \mu m$.

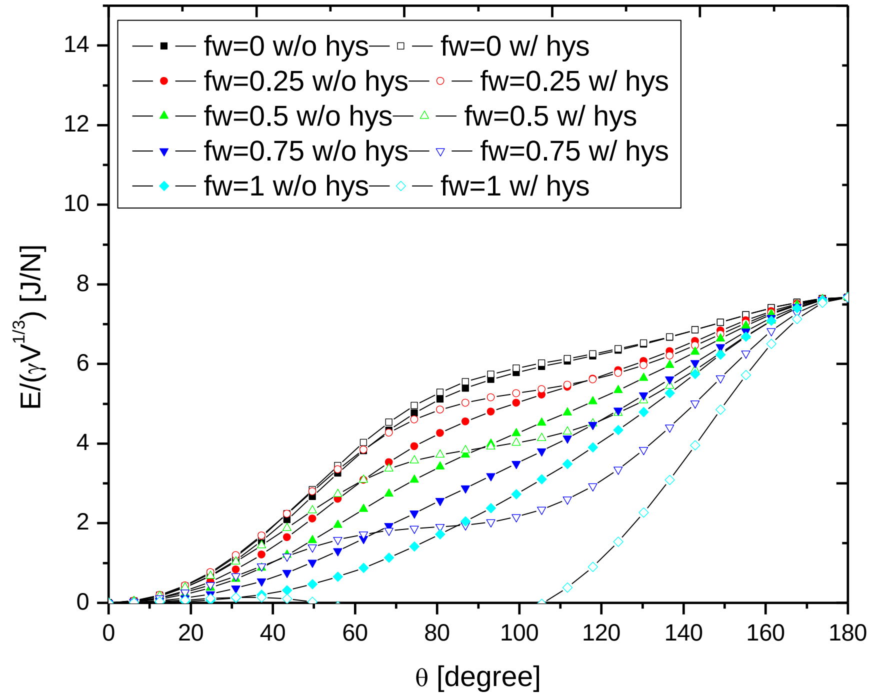
fw=0 w/o hys
fw=0 w/ hys
fw=0.25 w/o hys
fw=0.25 w/ hys
fw=0.5 w/o hys
fw=0.5 w/ hys
fw=0.75 w/o hys
fw=0.75 w/ hys
fw=1 w/o hys
fw=1 w/ hys
E/(γV^1/3) [J/N]
θ [degree]
0
2
4
6
8
10
12
14
0
20
40
60
80
100
120
140
160
180

(a)

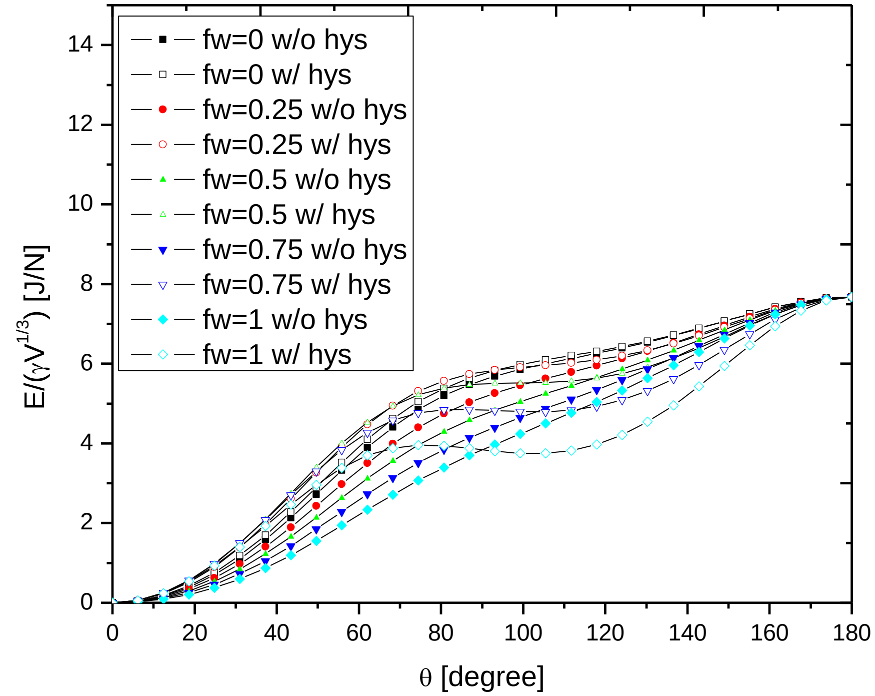
fw=0 w/o hys
fw=0 w/ hys
fw=0.25 w/o hys
fw=0.25 w/ hys
fw=0.5 w/o hys
fw=0.5 w/ hys
fw=0.75 w/o hys
fw=0.75 w/ hys
fw=1 w/o hys
fw=1 w/ hys
E/(γV^1/3) [J/N]
θ [degree]
0
2
4
6
8
10
12
14
0
20
40
60
80
100
120
140
160
180

(b)

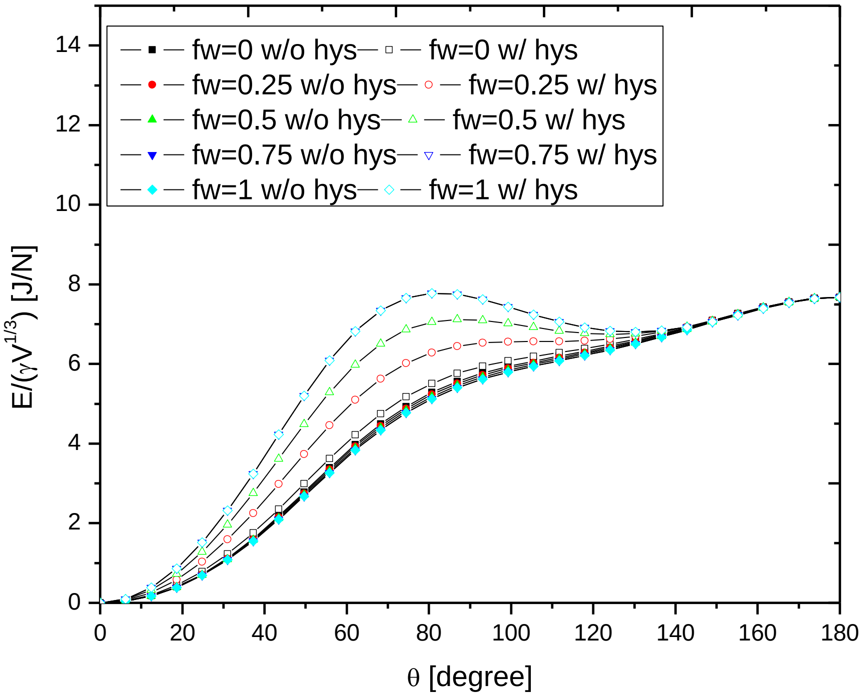

(c)

Figure 3.6 Surface energy profiles vs. contact angles for (a) *θ_0 =60°*, (b) *θ_0 =90°* and (c) *θ_0 =120°*, *b = 1 µm*, *h = 2 µm*, and *L = 3 µm*

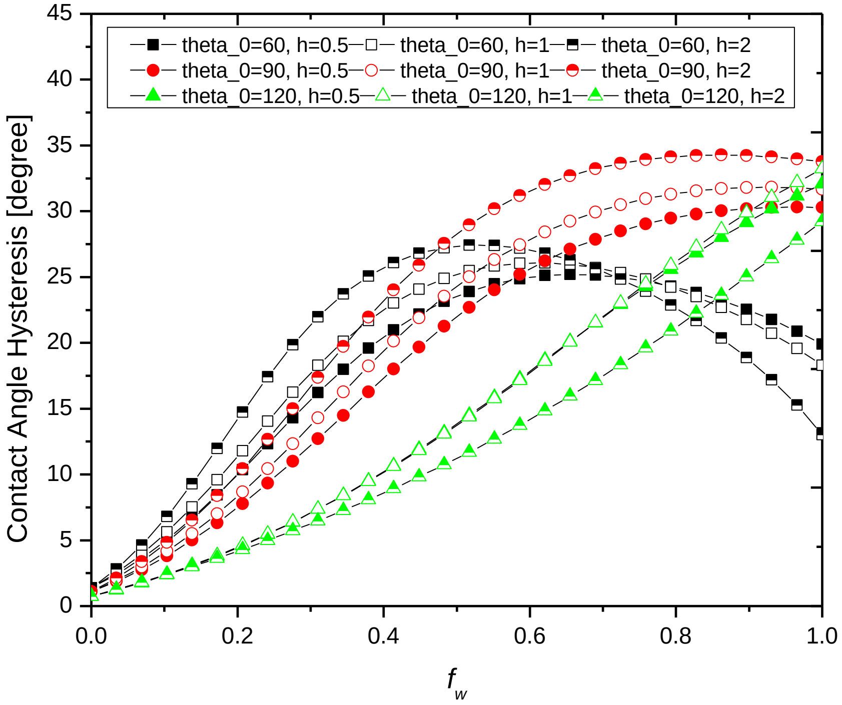

Figure 3.7 Contact angle hysteresis vs. fully wetted projection area ratio, *b = 1 μm*, *L = 3 μm*

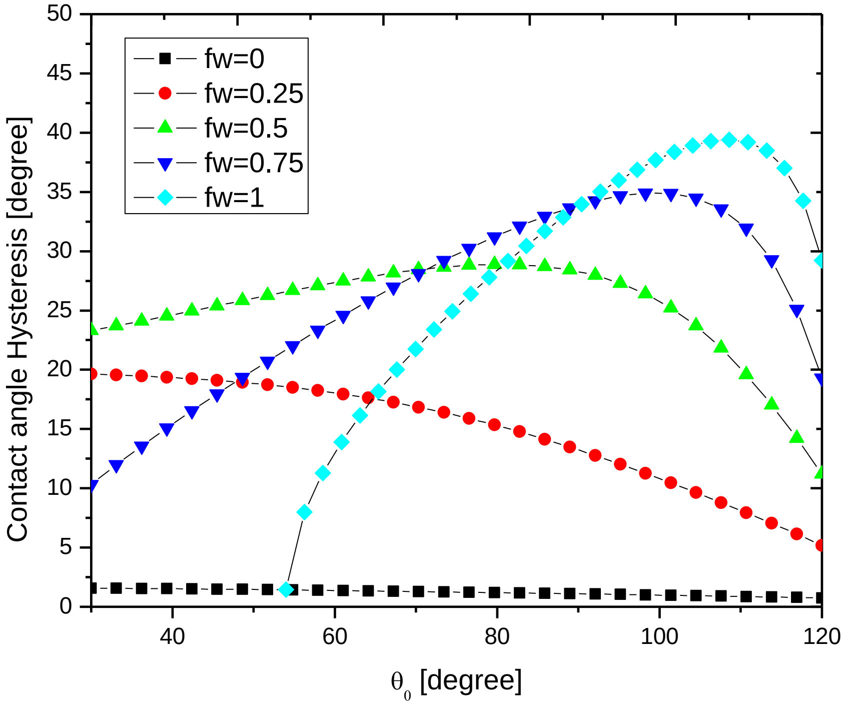

Figure 3.8 Contact angle hysteresis vs. Young's contact angles, *b = 1 μm*, *h = 2 μm*, *L = 3 μm*

From results of Figure 3.6, differences between surface energy profiles with and without hysteresis generally increases as wetted area ratio, f_w increases. These results indicate that it would take more energy to move contact lines of a drop in equilibrium state as more area is wetted. This is apparent in the results from $\theta_0 = 120°$. Difference between energy profiles at equilibrium and hysteresis state remains small at low values of f_w for $\theta_0 = 60°$, $\theta_0 = 90°$ and $\theta_0 = 120°$. These results demonstrate that CAH would remain small in Cassie-Baxter state. Apparent difference between equilibrium and hysteresis energy increases in Figure 3.6(a) and (b) for $\theta_0 = 60°$ and $\theta_0 = 90°$ in most of contact angle ranges. However, the two energy differences decreases at certain contact angle ranges at increasing as f_w increases. This indicated that CAH could decrease when drop is approaching Wenzel state in hydrophilic textured surface. When droplet is approaching Wenzel state on textured hydrophilic surface, contact angle decreases. This could explain decreases in CAH since droplet is being stretched out and approach a thin film at high value of f_w.

Increase pillar height increases surface roughness and Figure 3.8 shows that CAH increases as roughness increases at $\theta_0 = 90°$ across all values of wetting area ratio, f_w. CAH increases in $\theta_0 = 60°$ for $f_w \leq 0.7$ but decreases for $f_w \geq 0.7$ as surface roughness increases. In the case of $\theta_0 = 120°$, CAH decreases as roughness increases in all f_w values. At $\theta_0 = 90°$, increases on CAH with increasing roughness ratio could be explained as more liquid/solid contact area is presented for the same value of f_w. Therefore, higher roughness ratio increases CAH. In hydrophilic surface for $\theta_0 \leq 90°$, contact angle is decreased as roughness increases, therefore CAH increases with roughness. However, contact angle decreases at a faster rate as f_w increases. As shown in Figure 3.6, droplet is approaching film wise at a faster rate as wetting area increases, and CAH decreases CAH at higher value of f_w. Equilibrium contact angle increases on hydrophobic surface at high value of roughness ratio as shown in Equation (3.20). Equilibrium contact angle increases at a faster rate at increasing roughness ratio than contact angle at hysteresis state. Therefore CAH decreases with increased roughness ratio.

In different roughness profile, CAH trends remain similar with respect to projected wetting ratio, f_w for each corresponding local Young's contact angles, θ_0. Peak values are shown in Figure 3.6 in CAH for $\theta_0 = 60°$. This is explained before as wetting area increases, CAH would increase accordingly; at high wetting ratio, f_w, as contact angle approaches to 0, CAH would also decrease. At $\theta_0 = 90°$, CAH increases as f_w increases, but rate of increase decrease at higher values of f_w. For intermediate young's contact angle, increasing solid/liquid contact area increases surface energy, and CAH increases as a result. However, equilibrium contact angle values remains similar at higher value of f_w, therefore CAH remains flat at high wetting area ratio. In cases of $\theta_0 = 120°$, CAH increase with increasing f_w. This is due to the fact that at higher contact area of solid/liquid when the drop spreads into spaces between the pillars. More and more energy is required to move contact line of the drop. When liquid is trapped inside the spaces between the gaps in textured hydrophobic surface, it does not tend to spread to other areas very easily. Liquid becomes stagnated inside the gaps, thus more energy is required to induce movement on the contact line of a drop. CAH would increase with increasing values of f_w as a result.

With fixed surface geometries, CAH increased with increasing wetted areas in hydrophobic surface for $\theta_0 \geq 90°$, as shown in Figure 3.8. In hydrophilic surface with θ_0

$\leq 90°$, aside from non-wetted surface where $f_w = 0$, CAH values are lower at $f_w > 0.75$ and it is more apparent when values for θ_0 decrease. Figure 3.8 shows that CAH values are at peak with $f_w = 0.5$ if surface is hydrophilic. These phenomenons are explain above for individual cases for hydrophobic and hydrophilic textured surfaces.

At $f_w = 0$, CAH remains flat and remains small with varying Young's contact angles. Minimum solid/liquid contact area is maintained, thus little energy is required to move droplet contact line. At $f_w = 0.25$, CAH decreases with increasing θ_0. Droplet starts to spread out and solid/liquid contact area increases. Since contact line requires more energy to move in hydrophilic surfaces then hydrophobic surfaces, therefore CAH tends to be higher with lower values of θ_0. At $f_w = 0.5$, similar trend is seen with previous case for CAH vs. θ_0. Peak at CAH is starting to form with θ_0. Since contact area for solid/liquid is increased, more energy is needed to move contact line in hydrophilic surface. At lower values of θ_0, drop is starting to spread out and approach filmwise; CAH is starting to decrease. In cases of $f_w = 0.75$ and $f_w = 1$, there are clear maximum values of CAH with respect to young's contact angle. Droplet spreads out to be closer to filmwise at higher value of f_w as θ_0 decrease, thus CAH is also lower as a result. As θ_0 increase, equilibrium angle also increase as a result, but maximum angle increase at a slower rate at the same time as provided in Equations (3.17) and (3.29).

3.5 Condensation heat transfer modeling

In order to develop a population model to DWC, the basic mechanism of mass balance should be consider in the DWC scenario. A control surface of a section is constructed around a section of condensing surface where total condensate mass inside the control surface can only be gained by condensing vapor from the surrounding environment. Mass can only be decreased by condensate leaving the surface. Figure 3.9 illustrates the condensation process of such a scenario.

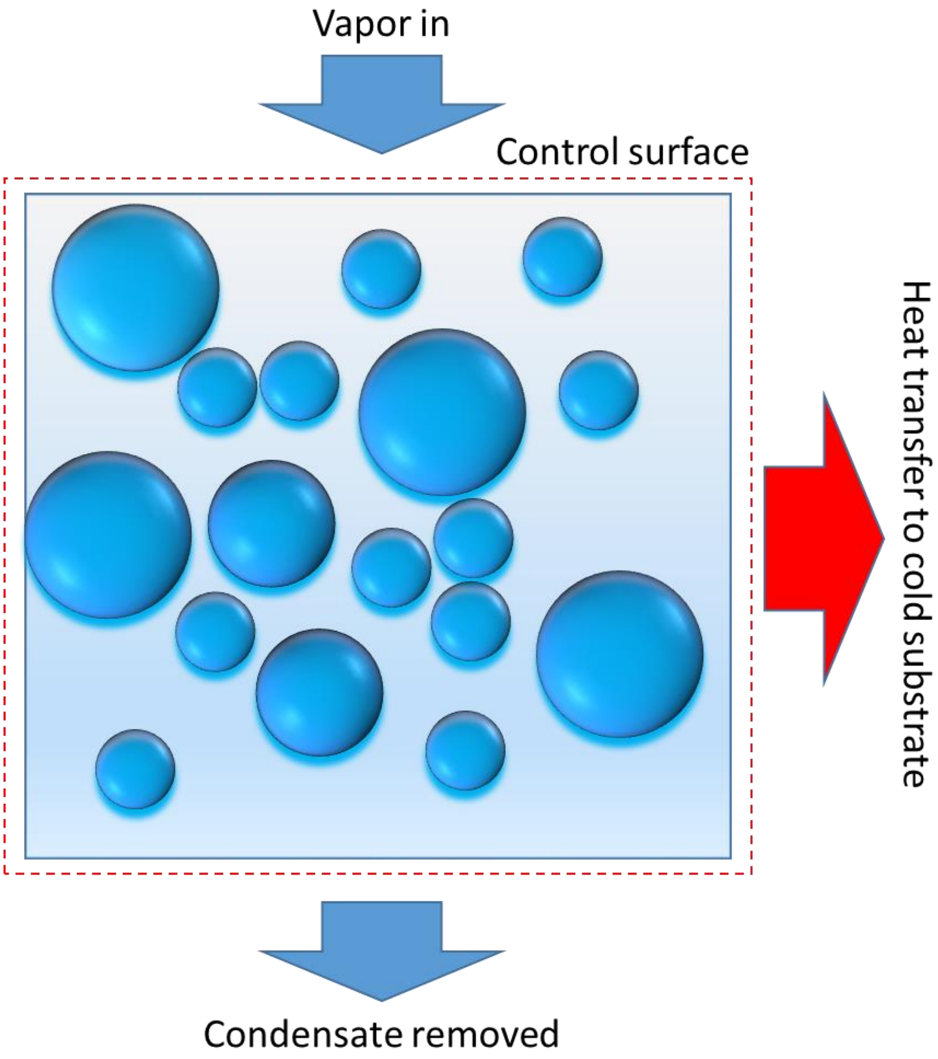

Figure 3.9 Condensation process illustration with a control surface

The condensate mass change rate inside the control surface can be written as,

$$\frac{dM}{dt} = \frac{dM_{in}}{dt} - \frac{dM_{out}}{dt} \tag{3.30}$$

Total condensate mass rates inside control surface, *dM/dt* are the difference between mass rates of vapor condensation, dM_{in}/dt and condensate removal, dM_{out}/dt.

Total mass gain by direct vapor condensation for DWC can be written as,

$$\frac{dM_{in}}{dt} = A \times n(r)\dot{m}'' A_C dr \tag{3.31}$$

$$A_C = 2\pi r^2(1 - \cos\theta)$$

where A is area of the control surface, and $n(r)$, $\dot{m}''$, A_C are drop size distribution, mass flux rate of vapor condensation of individual drop and drop cap area. θ and r are the equilibrium angle of droplet given in drop dynamic model previously and drop radius.

Mass flux rate of vapor condensation, $\dot{m}''$ is given as,

$$\dot{m}'' = \frac{h_{int}\Delta T_{int}}{H_{fg}} \tag{3.32}$$

where h_{int}, ΔT_{int}, and H_{fg} are interfacial heat transfer coefficient, interfacial temperature difference, latent heat of vaporization.

Interfacial temperature difference are given as,

$$\Delta T_{int} = \frac{q_d}{2\pi r^2(1-\cos\theta)h_{int}} \tag{3.33}$$

Heat transfer across drop is given as,

$$q_d = \rho H_{fg}\left(2\pi r^2(1 - \cos\theta)\right)\left(\frac{dr}{dt}\right) \tag{3.34}$$

dr/dt is the drop radius growth rate and ρ is droplet liquid density.

Equation (3.31) becomes,

$$\frac{dM_{in}}{dt} = A\rho\left(\frac{dr}{dt}\right)n(r)\left(2\pi r^2(1 - \cos\theta)\right)dr \tag{3.35}$$

Mass rate of condensate removal can be written as,

$$\frac{dM_{out}}{dt} = Sn(r)\rho V dr \tag{3.36}$$

$$V = \frac{\pi}{3} r^3 [2 - 3\cos\theta + \cos^3\theta]$$

S is the area sweeping rate for drop removal, and *V* is the drop volume.

At equilibrium, mass rate of change inside control surface approach zero,

$$\lim_{t\to\infty} \frac{dM}{dt} = 0 \tag{3.37}$$

Substituting Equations (3.35), (3.36) and (3.37), Equation (3.30) becomes,

$$\frac{2-3\cos\theta+\cos^3\theta}{6(1-\cos\theta)}\left(\frac{S}{A}\right) r = \frac{dr}{dt} \tag{3.38}$$

Assume S/A to be constant, both sides are integrated from minimum radius to maximum radius and Equation (3.38) becomes,

$$\int_{r_{min}}^{r_{max}} G dr = \frac{K}{2\tau}(r_{max}^2 - r_{min}^2) \tag{3.39}$$

$$\tau = \frac{A}{S}, K = \frac{2-3\cos\theta+\cos^3\theta}{6(1-\cos\theta)}, G = \frac{dr}{dt}$$

Drop growth rate, *G* and sweeping period, *τ* are unknown at the moment. Heat transfer of a single drop is to be solved. Drop growth rate by direct condensation can be solved from Equation (3.38),

$$G = \frac{q_d}{\rho H_{fg}\left(2\pi r^2(1-\cos\theta)\right)} \tag{3.40}$$

Drop heat transfer, q_d can found using thermal resistances and the individual temperature differences, as shown in Figure 3.10.

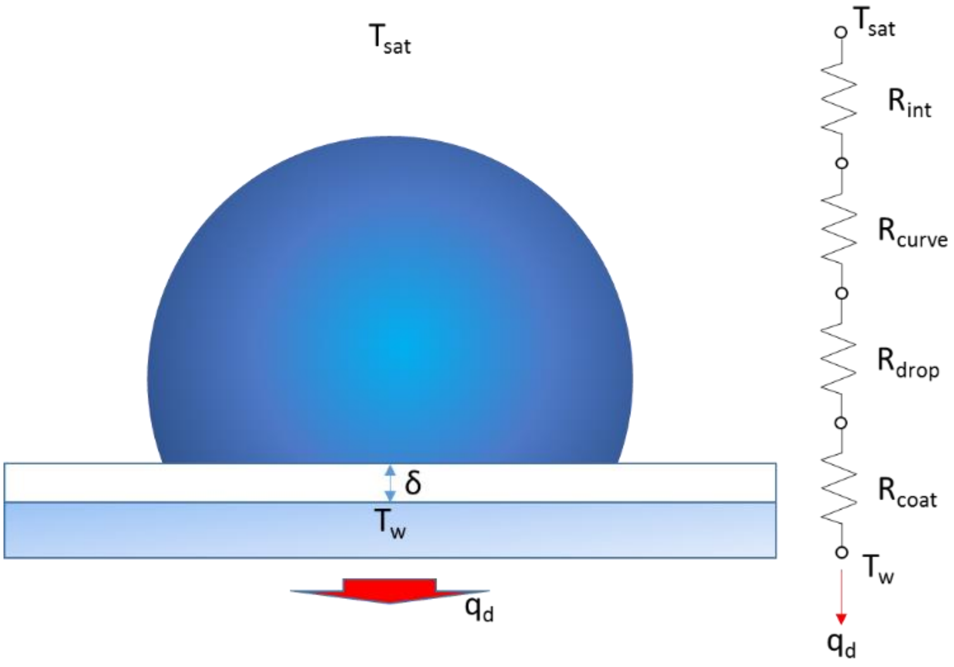

Figure 3.10 Single drop heat transfers illustration

Sum of temperatures drops by thermal resistances in a single condensate drop consisting of interfacial, a conduction through the condensate, a condensate drop curvature, and a fin like coating, which can be written as,

$$\Delta T = T_{sat} - T_w = \Delta T_{int} + \Delta T_{drop} + \Delta T_{curve} + \Delta T_{coat} \tag{3.41}$$

where T_{sat} and T_w are saturation temperature and surface temperature. ΔT_{int}, ΔT_{drop}, ΔT_{curv}, and ΔT_{coat} are the temperature drops due to thermal resistances of an interfacial, conduction through the condensate, a condensate drop curvature, and surface coating, respectively.

Interfacial temperature drop is given as,

$$\Delta T_{int} = \frac{q_d}{h_{int} 2\pi r^2 (1-\cos\theta)} \tag{3.42}$$

According to Sikarwar and Khandedar [29, 84, 85], interfacial heat transfer coefficient, h_{int} is given as,

$$h_{int} = \left(\frac{2\hat{\sigma}}{2-\hat{\sigma}}\right)\left(\frac{H_{fg}^2}{T_{sat}v_{fg}}\right)\left(\frac{\bar{M}}{2\pi\bar{R}T_{sat}}\right)^{\frac{1}{2}} \tag{3.43}$$

$\hat{\sigma}$ is accommodation coefficient and it is fraction of striking vapor molecule condensing into liquid. Values were reported ranging from 0.02 to 0.04 for alcohols and water. $\bar{R}$, $\bar{M}$, T_{sat}, and v_{fg} are ideal gas constant, molar mass, saturation temperature and specific volume of working fluid. Total heat transfer rate of a single drop is given as q_d.

According to Kim and Kim [40], temperature drop due to conduction heat transfer through the droplet, ΔT_{drop} is given by,

$$\Delta T_{drop} = \frac{q_d\theta}{4\pi r k_c \sin\theta} \tag{3.44}$$

where k_c is condensate droplet thermal conductivity.

Temperature drop due to coating thermal resistance, ΔT_{coat} is,

$$\Delta T_{coat} = \frac{q_d\delta}{k_{coat}\pi r^2 \sin^2\theta} \tag{3.45}$$

where δ is hydrophobic coating thickness. Coating conductivity k_{coat} can with written as following with consideration of surface morphologies and wetting condition,

$$k_{coat} = \varepsilon[(1-f_w)k_v + f_w k_c] + (1-\varepsilon)k_{fin} \tag{3.46}$$

ε, k_v and k_{fin} are porosity, vapor thermal conductivity, and surface fin thermal conductivity. From literature [86], temperature drop due to the condensate-drop curvature, ΔT_{curve} is,

$$\Delta T_{curve} = \frac{2T_{sat}\gamma}{H_{fg}r\rho} \tag{3.47}$$

where γ and ρ are condensate surface tension and density. Minimum viable drop radius, r_{min}, is determined by wall subcooling, ΔT, [87] and it is given as,

$$r_{min} = \frac{2T_{sat}\gamma}{H_{fg}\rho\Delta T} \tag{3.48}$$

Temperature drop due to drop curvature, ΔT_{curv}, in terms of minimum drop radius, r_{min}, is given as,

$$\Delta T_{curve} = \Delta T\frac{r_{min}}{r} \tag{3.49}$$

Heat transfer rate, q_d, through a drop of radius r is expressed as,

$$q_d = \frac{\Delta T\pi r^2\left(1-\frac{r_{min}}{r}\right)}{\left[\frac{\delta}{k_{coat}\sin^2\theta}+\frac{r\theta}{4k_C\sin\theta}+\frac{1}{2h_{int}(1-\cos\theta)}\right]} \tag{3.50}$$

Substitute Equation (3.51) into Equation (3.41), drop growth rate G_1 is,

$$G_1 = \frac{\frac{\Delta T}{2\rho H_{fg}}\left(1-\frac{r_{min}}{r}\right)}{\frac{r\theta(1-\cos\theta)}{4k_C\sin\theta}+\frac{\delta(1-\cos\theta)}{k_{coat}\sin^2\theta}+\frac{1}{2h_{int}}} = \frac{A_1\left(1-\frac{r_{min}}{r}\right)}{A_2 r+A_3} \tag{3.51}$$

$$A_1 = \frac{\Delta T}{2\rho H_{fg}}, A_2 = \frac{\theta(1-\cos\theta)}{4k_c\sin\theta}, A_3 = \frac{\delta(1-\cos\theta)}{k_{coat}\sin^2\theta}+\frac{1}{2h_{int}}$$

Once drop sizes reach a certain radius, drop growth would be dominated by coalescence from neighboring drops. This process is driven by surface tension forces unlike temperature difference driven as shown in Equation (3.51) According to Ristenpart [88] and Tanner [89], drop growth can be estimated as follows,

$$\frac{dR}{dt} \sim \left(\frac{\gamma}{\mu}\right)\left(\frac{H}{R}\right)^3 \tag{3.52}$$

H, μ and R are droplet height, liquid viscosity and drop radius. Drop height H, is given as,

$$H = R(1-\cos\theta) \tag{3.53}$$

Drop growth rate is related to contact angle as follows,

$$\frac{dr}{dt} = \Gamma(R)\left(\frac{\gamma}{\mu}\right)(1-\cos\theta)^3 \tag{3.54}$$

$\Gamma(R)$ is proposed as a dimensionless function to factor in the drop growth with respect to time. Drop growth by coalescence had be studied by past researchers [90, 91]. Drop radius is scaled proportional to $t^{1/2}$,

$$R \propto t^{1/2} \tag{3.55}$$

Divide both side with respect to a reference radius, R_0 and time, t_0 to get dimensionless form,

$$\left(\frac{R}{R_0}\right)^2 \propto \frac{t}{t_0} \tag{3.56}$$

Differential with respect to dimensionless factors,

$$2\left(\frac{R}{R_0}\right)\left(\frac{d\left(\frac{R}{R_0}\right)}{d\left(\frac{t}{t_0}\right)}\right) \propto 1 \tag{3.57}$$

Therefore, *dR/dt* could be written as,

$$\frac{dR}{dt} = F_1\left(\frac{R_0}{R}\right) \tag{3.58}$$

F_1 is a constant scaling factor. By comparing Equation (3.58) into (3.54), *dR/dt* becomes,

$$G_2 = \frac{dR}{dt} = \left(\frac{R_0}{R}\right)\left(\frac{\gamma}{\mu}\right)(1-\cos\theta)^3 \tag{3.59}$$

Vemuri [22] and Kim [40] separate drop sizes into small drops and large drops. Small drops sizes are in range of $r_{min}<r<r_e$, and large drops are in the range of $r_e \le r \le r_{max}$. Then drop growth rate can be separated into small and large drop growth rates by combining Equations (3.51) and (3.59). Substitute R_0 and R with r_{min} and r in Equation (3.59), drop growth rate is written as,

$$G(r) = \begin{cases} \frac{A_1\left(1-\frac{r_{min}}{r}\right)}{A_2 r + A_3}, \ r_{min} < r < r_e \\ \left(\frac{r_{min}}{r}\right)\left(\frac{\gamma}{\mu}\right)(1-\cos\theta)^3, \ r_e \le r < r_{max} \end{cases} \tag{3.60}$$

According to literatures [92, 93], effective drop radius, r_e is given as,

$$r_e = (4N_S)^{-\frac{1}{2}} \tag{3.61}$$

N_S is nucleation sites per unit area. Khandekar [85] determined maximum radius, r_{max} by force balance between surface tension, γ and gravity forces and also tilt angle, α. It is given as,

$$r_{max} = \sqrt{\left(\frac{1.25\sin\theta}{2-3\cos\theta+\cos^3\theta}\right)\left(\frac{(\cos\theta_{rcd}-\cos\theta_{adv})\gamma}{(\rho-\rho_g)g\sin\alpha}\right)} \tag{3.62}$$

θ_{rcd}, θ_{adv}, ρ_g, and g are receding angle, advancing angle, vapor density and gravitation acceleration.

Integrate drop growth rate from Equation (3.39),

$$\int_{r_{min}}^{r_{max}} G dr = \int_{r_{min}}^{r_e} G_1 dr + \int_{r_e}^{r_{max}} G_2 dr \tag{3.63}$$

$$G_1 = \frac{A_1\left(1-\frac{r_{min}}{r}\right)}{A_2 r + A_3}, G_2 = \left(\frac{r_e}{r}\right)\left(\frac{\gamma}{\mu}\right)(1-\cos\theta)^3$$

$$\int_{r_{min}}^{r_e} G_1 dr = \frac{A_1}{A_2 A_3}\left[(A_2 r_{min} + A_3)\ln\frac{A_2 r_e + A_3}{A_2 r_{min} + A_3} + A_2 r_{min}\ln\frac{r_{min}}{r_e}\right]$$

$$\int_{r_e}^{r_{max}} G_2 dr = r_{min}\left(\frac{\gamma}{\mu}\right)(1-\cos\theta)^3 \ln\frac{r_{max}}{r_e}$$

Substitute Equation (3.63) to (3.39) and solve sweeping period, τ,

$$\tau = \frac{K}{2}(r_{max}^2 - r_{min}^2)\left[\int_{r_{min}}^{r_{max}} G dr\right]^{-1} \tag{3.64}$$

Kim[40] propose drop population balance, and it is given as,

$$\frac{d}{dr}(Gn) + \frac{n}{\tau} = 0 \tag{3.65}$$

Expand Equation (3.65),

$$G\left(\frac{dn}{dr}\right)+n\left(\frac{dG}{dr}\right)=-\frac{n}{\tau} \qquad (3.66)$$

Rearrange Equation (3.66) and solve for *n*,

$$n(r)=C_1\exp\left(-\int\frac{G\prime}{G}dr\right) \qquad (3.67)$$

$$G'=\frac{dG}{dr}+\frac{1}{\tau}$$

$$\frac{dG}{dr}=\begin{cases}\frac{A_1(A_2r(2r_{min}-r)+A_3r_{min})}{r^2(A_2r+A_3)^2}, r_{min}<r<r_e\\ -\left(\frac{r_{min}}{r^2}\right)\left(\frac{\gamma}{\mu}\right)(1-\cos\theta)^3, r_e\leq r<r_{max}\end{cases}$$

Apply boundary condition when small and large drop distribution should be equal at *n(r_e)=N(r_e)*,

$$n(r)=\begin{cases}N(r_e)\left[\frac{r(r_e-r_{min})}{r_e(r-r_{min})}\right]\left[\frac{A_2r+A_3}{A_2r_e+A_3}\right]\exp(B_1+B_2),\ r_{min}<r<r_e\\ N(r),\ r_e\leq r<r_{max}\end{cases} \qquad (3.68)$$

$$B_1=\frac{A_2}{\tau A_1}\left[\frac{r_e^2-r^2}{2}+r_{min}(r_e-r)-r_{min}^2\ln\left(\frac{r-r_{min}}{r_e-r_{min}}\right)\right]$$

$$B_2=\frac{A_3}{\tau A_1}\left[r_e-r-r_{min}\ln\left(\frac{r-r_{min}}{r_e-r_{min}}\right)\right]$$

Le Fevre and Rose [27, 94] establish drop size distribution for large drop and it is given as,

$$N(r)=\frac{1}{3\pi r^2r_{max}}\left(\frac{r}{r_{max}}\right)^{-\frac{2}{3}},\ \&r_e\leq r<r_{max} \qquad (3.69)$$

When Equation (3.69) is applied to Equation (3.68), drop sizes distribution is achieved as following as determined by Kim [40],

$$n(r)=\frac{1}{3\pi r_e^3r_{max}}\left(\frac{r_e}{r_{max}}\right)^{-\frac{2}{3}}\left[\frac{r(r_e-r_{min})}{(r-r_{min})}\right]\left[\frac{A_2r+A_3}{A_2r_e+A_3}\right]\exp(B_1+B_2), r_{min}<r<r_e \qquad (3.70)$$

Sweeping period, τ with Kim's model is given as,

$$\tau = \frac{3r_e^2(A_2r_e+A_3)^2}{A_1\left(11A_2r_e^2-14A_2r_er_{min}+8A_3r_e-11A_3r_{min}\right)} \tag{3.71}$$

In order to find heat flux, heat transfer rate of single drop is integrated with respective drop size distribution ranges and it is given as,

$$q'' = \int_{r_{min}}^{r_e} q_d n(r)dr + \int_{r_e}^{r_{max}} q_d N(r)dr \tag{3.72}$$

3.6 Heat transfer and population modeling results and discussion

By combining drop dynamic model and heat transfer model, effects of drop dynamic on condensation heat transfer can be examine along with other factors. Coating thickness is one of the major thermal resistances in condensation heat transfer. According to Lee [39], coating thickness contribute significant thermal resistance in DWC. As coating thickness increases, temperature difference across coating becomes dominant. A lot of DWC promoters are made of low energy materials such as PTFE, or other Fluoride based polymers. It is important to understand how coating thickness would affect condensation heat transfer. In modeling results, water is used as working fluid and properties of water are set at saturation temperature, $T_{sat} = 100°C$. Figure 3.11 examined the effects of coating thickness with varies contact angle on flat surface with wetting fraction, $f_w = 1$, tilting angle, $\alpha = 90°$ and coating thermal conductivity, $k_{coat} = 0.2\ W/m\text{-}K$.

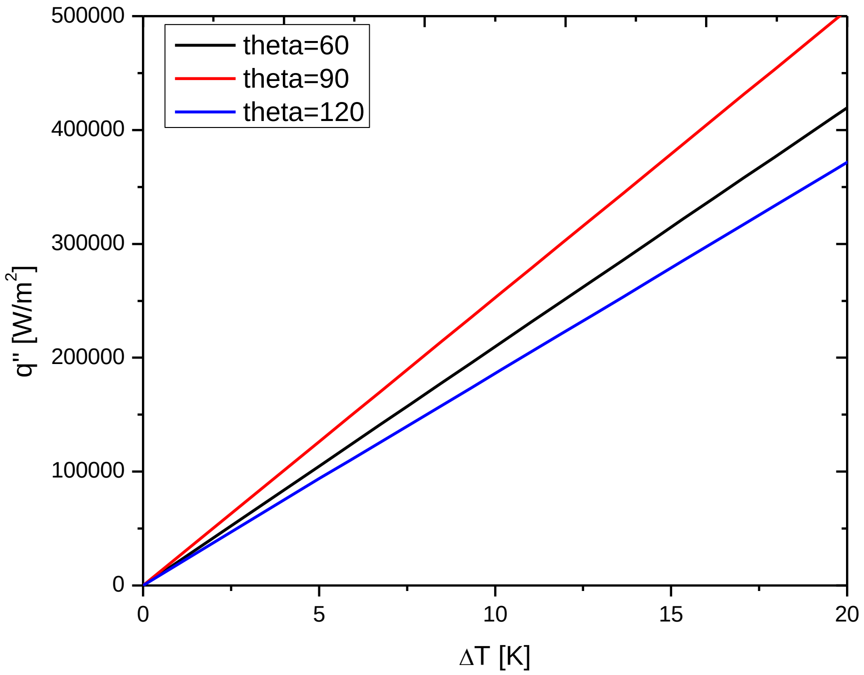
theta=60
theta=90
theta=120
q'' [W/m^2]
0
100000
200000
300000
400000
500000
0
5
10
15
20
ΔT [K]

(a)

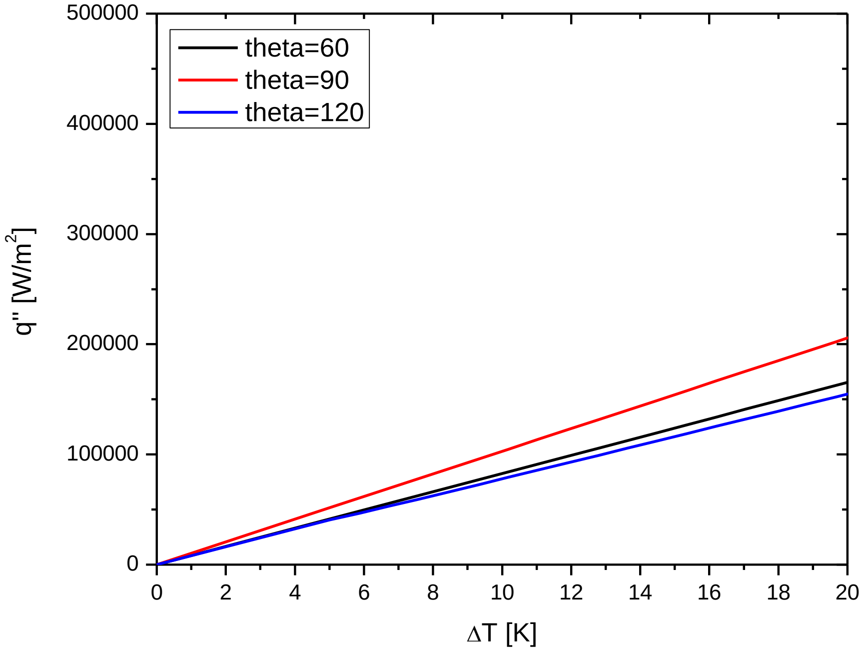
theta=60
theta=90
theta=120
q'' [W/m^2]
0
100000
200000
300000
400000
500000
0
2
4
6
8
10
12
14
16
18
20
ΔT [K]

(b)

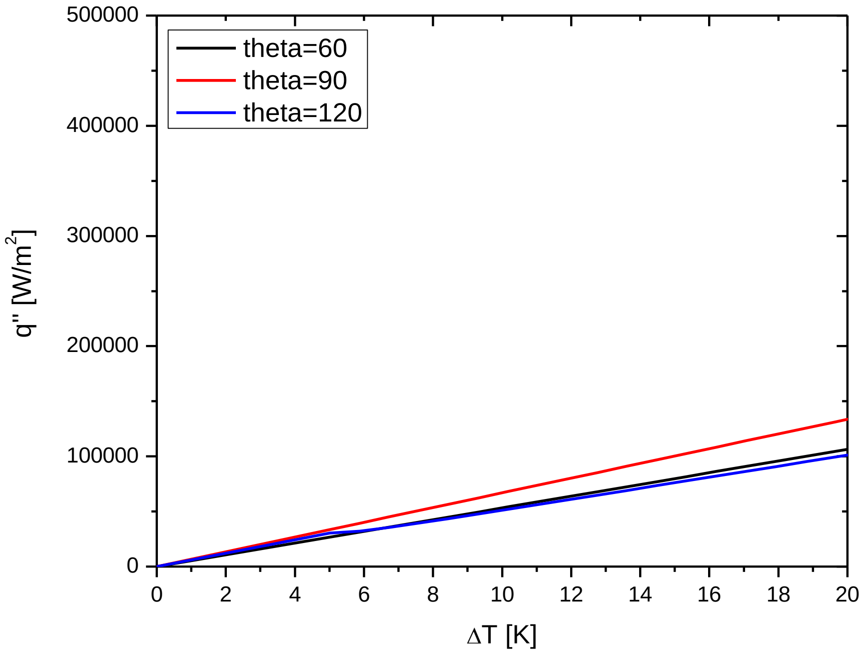

(c)

Figure 3.11 Heat fluxes vs. subcooling temperature differences (a) δ = 1 µm (b) δ = 5 µm (c) δ = 10 µm

Condensation heat transfers are shown to be at highest at contact angle at 90° and heat fluxes are shown to be lowest at 120°. This could be explained with drop dynamic model, as contact angle increase, CAH decrease. However, base contact area also decrease as a result. Therefore, heat transfer is a maximum for surface contact angle at 90°.

While concentrating on coating thickness, heat fluxes decrease 50% from 1 µm to 5 µm. Heat fluxes decreases another 50% from 5 µm to 10 µm. Temperature difference becomes more significant at thickness increases, and it becomes dominant at large thickness values. Figure 3.12 shows effects of coating thickness to heat fluxes with temperature difference set at 10 K and contact angle at 90° with wetting fraction, $f_w = 1$.

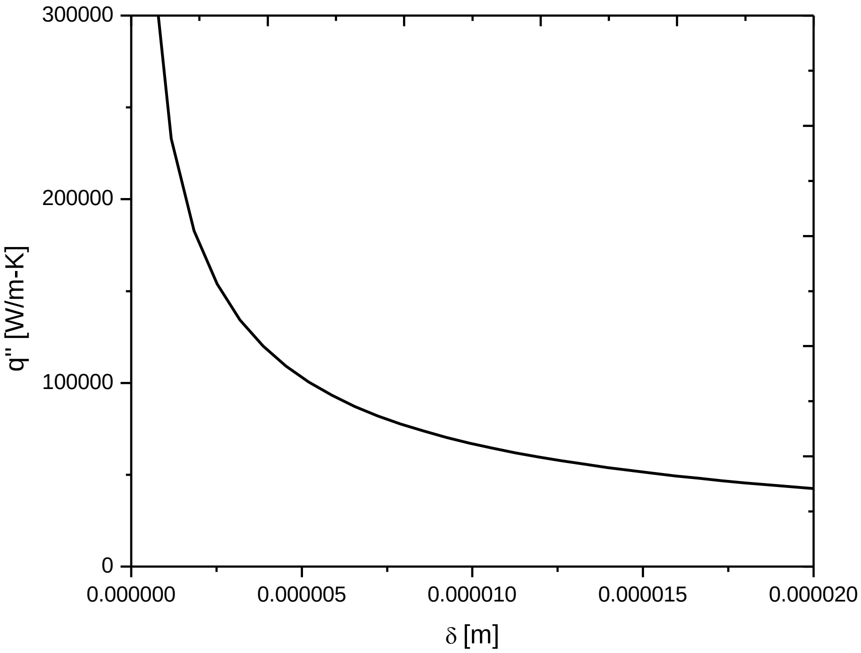

Figure 3.12 Heat fluxes vs. coating thickness

Liquid would often penetrate spaces between the surface geometries in textured surfaces during condensation. Thus relationships between heat transfer with surface morphologies and geometries are to be examined. Effects on the degrees of wetting should be first studied in that regard. Increase wetting under droplet would generally increase CAH as discussed previously. However, it is also discussed that in previous section that increase roughness could lower CAH in certain ranges of contact angles. Figure 3.13 compared effects on two different degrees of wetting, $f_w = 0.5$ and $f_w = 1$ on heat fluxes with different Young's contact angles with fixed coating geometries with $r_f = 1.5$, $\phi = 0.1$, $\delta = 1\ \mu m$, and $\varepsilon = 0.7$. This represents effect of partially and fully wetted textured surface scenario in condensation.

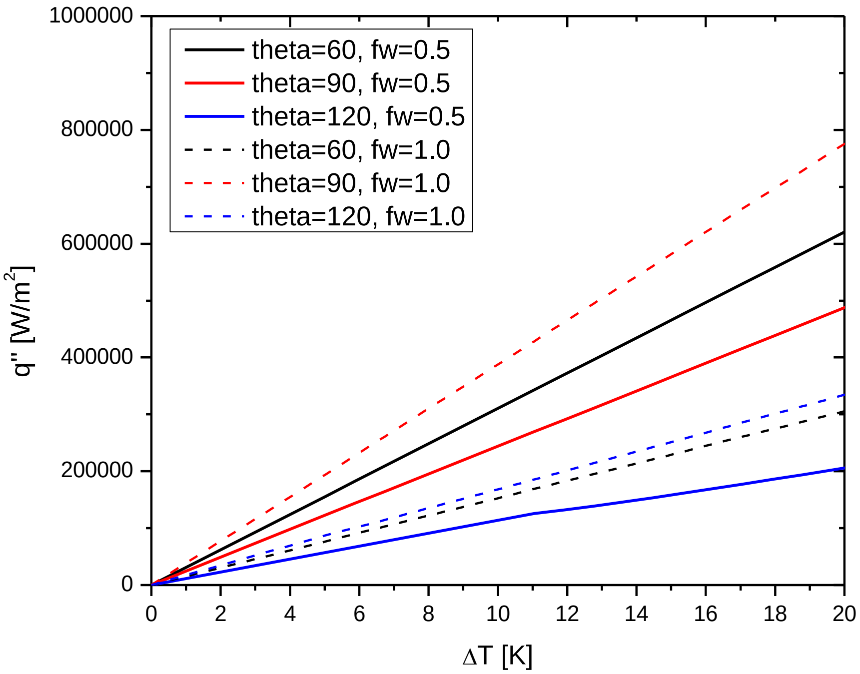

Figure 3.13 Heat fluxes vs. subcooling temperature differences for $f_w = 0.5$ and $f_w = 1$

Heat fluxes are shown to be highest with $\theta_0 = 60°$ at $f_w = 0.5$, and it is the highest with $\theta_0 = 90°$ at $f_w = 1.0$. Heat fluxes are at minimum with $\theta_0 = 120°$ at $f_w = 0.5$, and it is the highest with $\theta_0 = 60°$ at $f_w = 1.0$. It is also shown that heat fluxes are highest with $\theta_0 = 90°$ at $f_w = 1.0$ and lowest with $\theta_0 = 120°$ at $f_w = 0.5$, in overall results. CAH is lower in partially wetted surface comparing to fully wetted surface. However, thermal conductivity of void portion underneath the droplet has much higher thermal resistance then wetted portion. The combine contribution of both CAH and thermal resistance in both cases results in Figure 3.13.

Surface geometries are responsible for varying CAHs as discussed in drop dynamic modeling section. Varying geometries could have significant impact on heat transfer. Figures 3.14 shows heat flux vs. temperature differences for different contact angles, $\theta_0 = 60°, 90°, 120°$ with varying roughness, $r_f = 1.25, 1.5$ and 1.75 with fixed values of $\phi = 0.2$, $\varepsilon = 0.7$, $\delta = 5\ \mu m$, and $f_w = 0.5, 1.0$.

Figure 3.15 shows how varying top projection area ratio, $\phi = 0.1, 0.3$ would impact heat flux with different Young's contact angles, $\theta_0 = 60°, 90°, 120°$. Other parameters values are set at, $r_f = 1.5$, $\varepsilon = 0.7$, $\delta = 5\ \mu m$, and $f_w = 0.5, 0.75$.

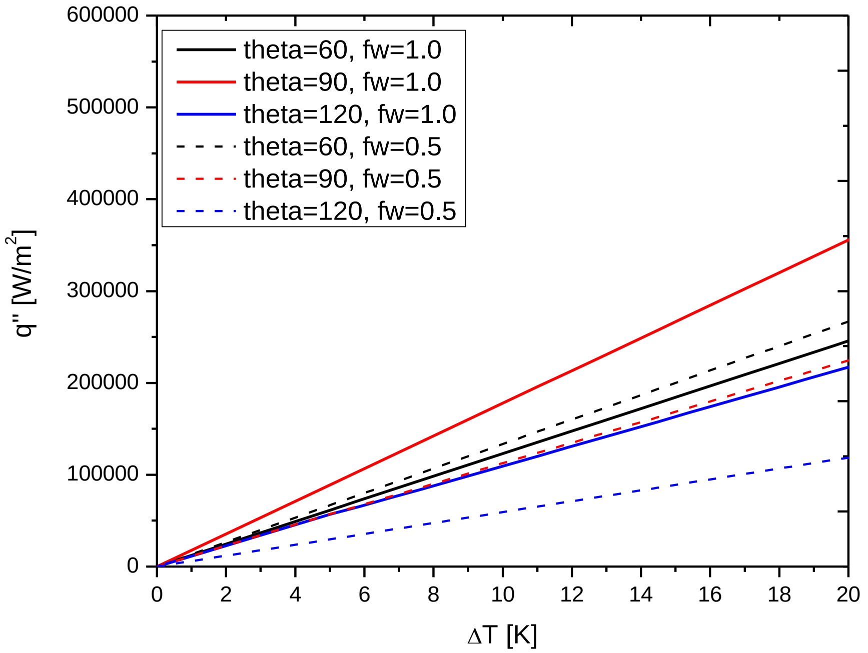
theta=60, fw=1.0
theta=90, fw=1.0
theta=120, fw=1.0
theta=60, fw=0.5
theta=90, fw=0.5
theta=120, fw=0.5
q'' [W/m^2]
ΔT [K]
0
100000
200000
300000
400000
500000
600000
0
2
4
6
8
10
12
14
16
18
20

(a)

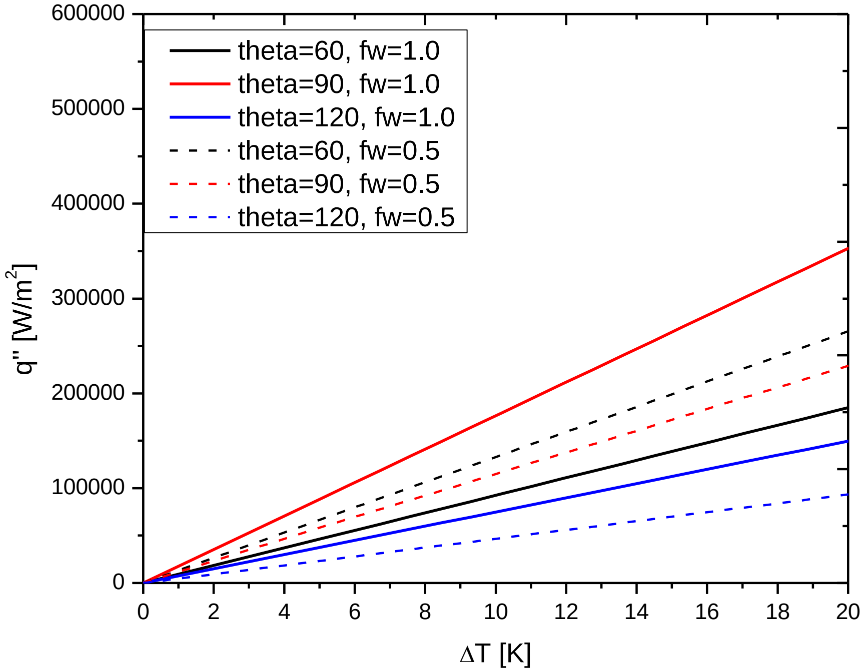
theta=60, fw=1.0
theta=90, fw=1.0
theta=120, fw=1.0
theta=60, fw=0.5
theta=90, fw=0.5
theta=120, fw=0.5
q'' [W/m^2]
ΔT [K]
0
100000
200000
300000
400000
500000
600000
0
2
4
6
8
10
12
14
16
18
20

(b)

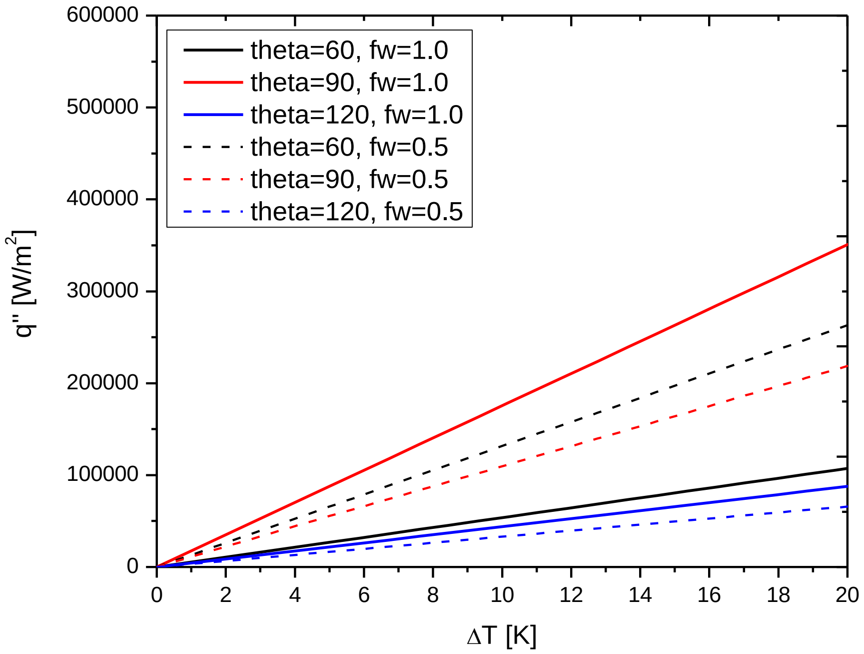

(c)

Figure 3.14 Heat fluxes vs. subcooling temperature differences (a) $r_f = 1.25$ (b) $r_f = 1.5$ (c) $r_f = 1.75$

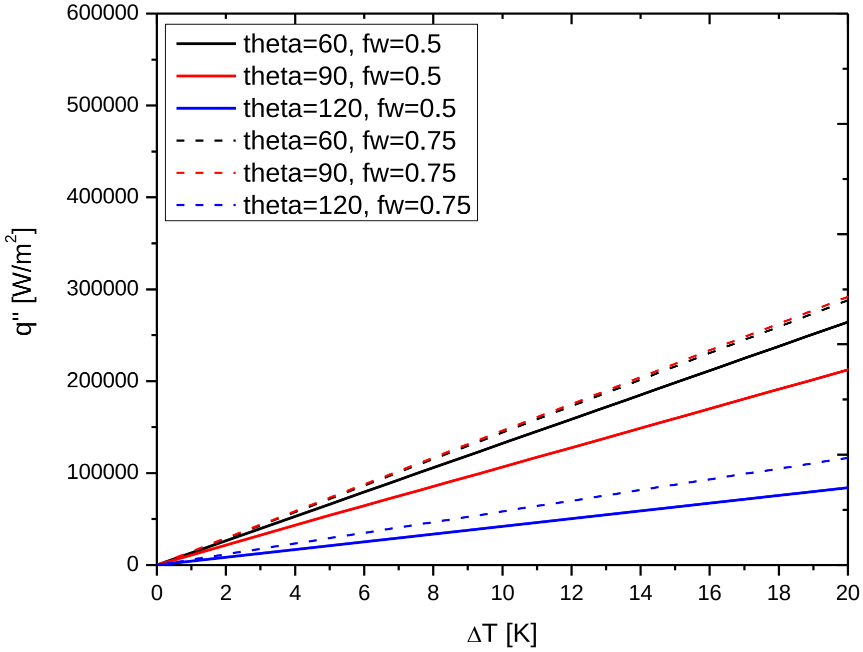

(a)

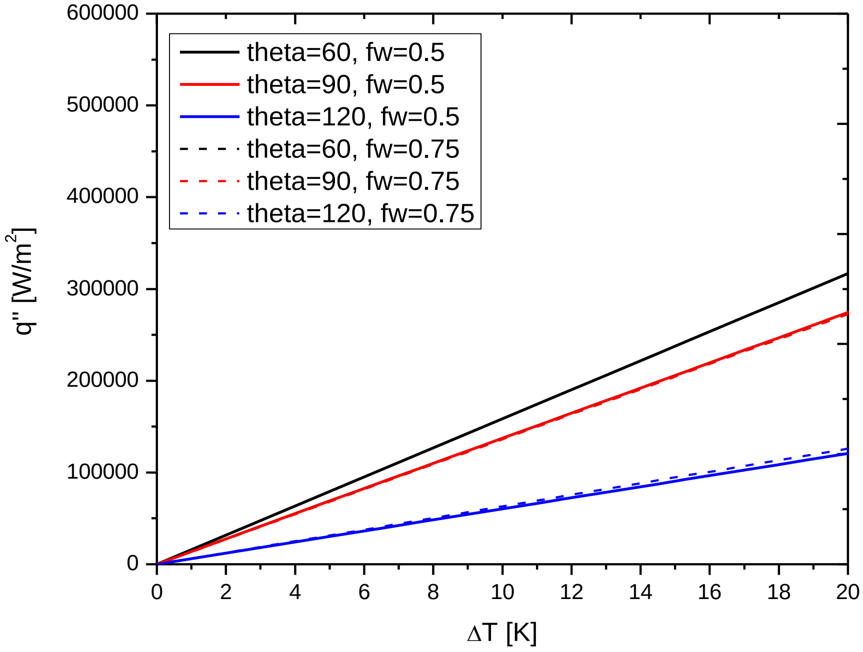

(b)

Figure 3.15 Heat fluxes vs. subcooling temperature differences (a) $\phi = 0.1$ (b) $\phi = 0.3$

Heat fluxes generally decrease with increased roughness ratio in fully wetted surface as shown in the results of Figure 3.14. However, heat fluxes are shown to be unaffected with roughness ratio in partially wetted surface, but overall heat fluxes are shown to be higher in fully wetted cases. CAH is lower in partially wetted surface, thus values of drop renewal period, τ is also lower. Thus heat flux would be increase as a result. CAH is higher in fully wetted surface and heat fluxes would be lower. However, temperature drop from coating would be lower fully wetted surface since thermal resistances from coating thickness is significant. Figure 3.14 shows the results of heat fluxes in combination of both contributions from drop dynamic and coating thermal resistance.

Figure 3.15 shows that when roughness stays the same, higher heat fluxes is achieved with higher degrees of wetting. This phenomenon is explained previously. However, as values of ϕ increase, degrees of wetting are not important in heat fluxes. Values of heat fluxes between $f_w = 0.5$ and $f_w = 0.75$ are almost identical in case of $\phi = 0.3$ as shown in Figure 3.15 (b). Heat fluxes values are also shown to be higher in $\phi = 0.3$ than $\phi = 0.1$. CAH would decrease as top projection area increase with the same roughness. Heat flux would also increase with decrease CAH. Area between the textured surfaces would decrease with increased top projection surface. Therefore, degree of wetting is less significant in condensation heat transfer. Thus heat fluxes stay the same with increased wetting fraction at higher values of ϕ.

Overall, drop dynamic in relation to surface geometries and degrees of wetting plays a significant role in affecting condensation heat transfer. Coating thicknesses as well as coating thermal conductivities are also important factors to be considered in condensation heat transfer. As coating thickness increase, thermal resistance becomes more significant. Benefits of low CAH values are being outweighed by coating thermal resistances with increasing thickness. Heat fluxes would be higher with increased wetting at increased coating thickness, since condensate has higher thermal conductance in common working fluid such as water.

3.7 Condensation modeling summary

In drop dynamic modeling, CAH was found to be closely related to surface geometries and materials. CAH remains low for droplet in Cassie-Baxter state, and it generally increases as solid/liquid interfacial area increases. It is found that CAH generally increases for hydrophobic coatings with increased roughness ratio, but decreases for hydrophilic coatings.

In heat transfer modeling, it was found that higher CAH would increase maximum drop sizes, thus heat flux decreases. However, as coating thickness increases, thermal resistance also increases. This becomes significant and it could overcome benefits of lower CAH in condensation heat transfer.

4. Experimental results

4.1 Objectives

Condensation model in this work is designed to predict trends of condensation heat transfer with given parameters such as coating thickness, wettability, and surface geometries. Experiments were performed to compare modeling and experimental results. The main objectives are,

1. Different surface geometries and wetting properties were developed with multiple coating fabrication methods;
2. Wettability and surface geometries were obtained with contact angle measurements and surface imaging techniques;
3. Condensation experimental results were then compared with modeling results with properties inputs from contact angles and surface imaging
4. Drop distribution were studied experimentally and provide insights for in depth droplet group behaviors in condensation

4.2 Polymer based coatings fabrication

Polymers are usually the choice for DWC promoter due to variety of wetting and chemical properties. Low surface energy surfaces are desirable in creating hydrophobic surface, and fluoride based polymers such as PTFE are some of the low surface energy materials for surface coatings. Recently polymer composites are on the subject of interest in creating super-hydrophobic surfaces. Different wetting properties can be achieved by combining different types of polymers. In this project, two types of polymer based porous surfaces coatings were prepared, and their compositions are summarized as follows.

Table 4.1 Composition of polymer coatings

Composition	PPS (parts)	PTFE (parts)	$(NH_4)_2CO_3$ (parts)	SiC (parts)	PEG (parts)	Additive (CNT) (parts)
Coating 1 (C1)	36	20	20	4	2	None
Coating 2 (C2)	36	20	20	4	2	3

Procedures to produce porous surface using the polymers are as follows:

- Components of the coatings are weighted and put into isopropanol solution
- The mixtures are sonic-mixed for 20 minutes
- Metal substrates are polished with a 300 grid sand paper and then cleaned with ethanol and acetone solutions
- The coating mixtures are applied to the metal substrates
- The coated metals are left to dry for 24 hours at room temperature
- The coated metal substrates are baked in an oven at 340°C for four hours

4.3 Copper oxide coatings fabrication

Copper oxide coatings were fabricated to introduce finer surface texture on copper surface. In this approach, an intrinsically hydrophilic surface is modified into a hydrophobic surface by introducing a sub millimeter-level of the primary surface treatment to provide irregular patterns, thereby trapping vapor and serving as the potential active nucleation sites on copper oxide Micro structure. The tertiary roughness is created by a bottom-up process. The surface of copper is treated with a power grinding tool and then a specially formulated solution was used to form the self-assembled copper oxide micro structure. The micro roughness generated by a grinding power tool, plays two important roles: (1) mechanically interlocks between a copper substrate and a self-assembled layer with enhanced adhesive strength and (2) increases nucleation sites on self-assemble layer.

The procedures to produce copper oxide self-assemble coating are described below:

- For the primary surface treatment, a power tool grinding (Grit-120) is used
- The specimen is cleaned in acid ($HCl:HNO_3$) to activate the surface and remove organic residues
- The specimen is cleaned in acetone for ten minutes under ultra-sonication
- On top of the primary surface treatment, the microstructure of the secondary modifications is introduced using NH_4OH solution
- The specimens are immersed in the NH_4OH solution for 72 hours at room temperature
- The self-assembled copper oxide black coating is formed on the surface (hydrophilic copper oxide surface)

- Thorough De-Ionized (DI) water rinsing is carried out several times
- The specimen is dried with compressed air
- The hydrophobic coating procedure is followed by immersing the specimen in a 1 mMol of 1-dodecanethiols solution for a day at room temperature (hydrophobic organic self-assembled layer)
- Thorough ethanol rinsing is carried out several times

4.4 Self-assembled organic coating fabrication

Hydrophobic surface can be fabricated in a more direct approach with self-assembled organic compounds with regular surface roughness pattern. In this method, two steps chemical treatments can be applied in order to achieved surface with super-hydrophobic properties. Manufacturing process is easier to control and more cost effective through this method. Self-assembled organic coating was fabricated using coating fabrication technique proposed by Vemuri [23], and manufacture process is as follows:

- Copper substrate is polished by fine sand paper to remove surface impurities and oxide layers
- Substrate is then clean in series of ethanol and acetone
- Once copper substrate is free of impurities, surface is oxidized with 30% wt H_2O_2 solution for 24 hours at room temperature.
- Substrate is then taken out and thoroughly rinsed with DI water and dried with compressed air

- 2 mMol octadecanethiol solution is prepared in ethanol for forming surface coating
- Substrate is immerged in octadecanethiol solution for another 24 hours at room temperature
- Copper substrate is then cleaned with ethanol to rinse out excess solution on the surface
- It is dry with compressed air quickly to reveal hydrophobic coating

4.5 Silver based coating fabrication

Noble metal coating such as gold, silver and platinum has reported to promote DWC [68-71]. Noble metals are known to be durable as surface coating with high thermal conductivities. Metal oxide nano particles are in subject of research subject with advent of nano-technology and interesting thermal physical properties were discovered[95]. Silver based coating was developed in this study. In aqueous silver nitration solution, silver and nitrate are ionized. Individual ions interact with counter anion (OH^-) and cation (H^+) and eventually crystallize into silver hydroxide: $AgNO_3$ (aq) + H_2O (aq) → AgOH (s) + HNO_3 (aq). Fabrication procedure is as followed:

- Substrate is polished with sand paper and cleaned with ethanol and acetone to remove impurities
- 10 mMol $AgNO_3$ solution is prepared in water
- Substrate is immerged into silver nitrate solution for 5 seconds and then quickly withdrawn to form a thin layer of silver oxide
- Excess particles were rinsed off DI water and dried with compressed air
- This procedure is repeated five times and silver oxide layer is visible
- 1 mMol 1-docanethiol ethanol solution is prepared and applied by finely spray evenly with spray gun 3 times.

4.6 Plain surface preparation for filmwise condensation

Smooth uniformly oxidized copper tube is also fabricated to provide base line experimental FWC comparison with the structured surfaces. Fabrication process for smooth oxidized surface is as follows,

- Copper substrate is polished incrementally from 150, 300, 800, 1000, 2000 grid sand papers, to get rid of any metal oxides and other materials on the surface and smooth out the substrate at the same time.
- Ultra-fine steel wool is used to smooth out any remaining imperfections and gives the surface a mirror finish.
- Acetone and ethanol is used to eliminate any organic materials and contaminates on the surface.
- Substrate is soaked in 30% wt H_2O_2 solution at 22 °C for 24 hours. It is then rinsed with DI water thoroughly and dried with compressed air.

4.7 Surface morphologies and contact angle analysis

Surface morphologies should be studied in order to understand how surface textures and geometries affect condensation heat transfer. Figure 4.1 shows scanning electron microscope (SEM) images of surface morphologies for polymer, copper oxide, self-assembled organic and silver based coatings. Figure 4.2 shows water contact angle measurements in atmospheric condition with coatings listed in Figure 4.1 and with H_2O_2 oxidized surface as reference for FWC (see section 4.5).

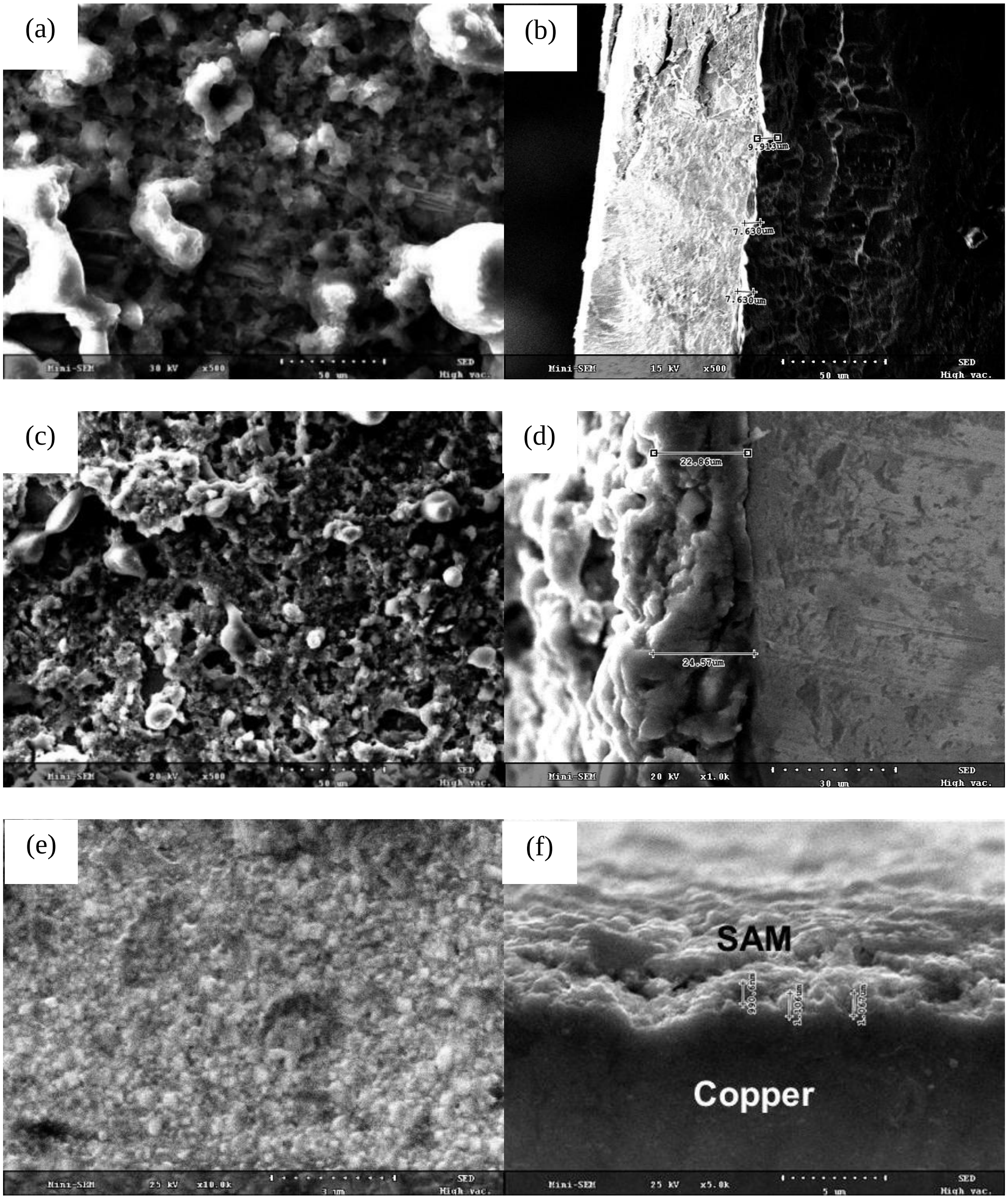
(a)
Mini-SEM 30 kV x500 50 um SED High vac.
(b)
9.913um
7.630um
7.630um
Mini-SEM 15 kV x500 50 um SED High vac.
(c)
Mini-SEM 20 kV x500 50 um SED High vac.
(d)
22.86um
24.57um
Mini-SEM 20 kV x1.0k 30 um SED High vac.
(e)
Mini-SEM 25 kV x10.0k 3 um SED High vac.
(f)
SAM
990.6nm
1.106um
1.067um
Copper
Mini-SEM 25 kV x5.0k 5 um SED High vac.

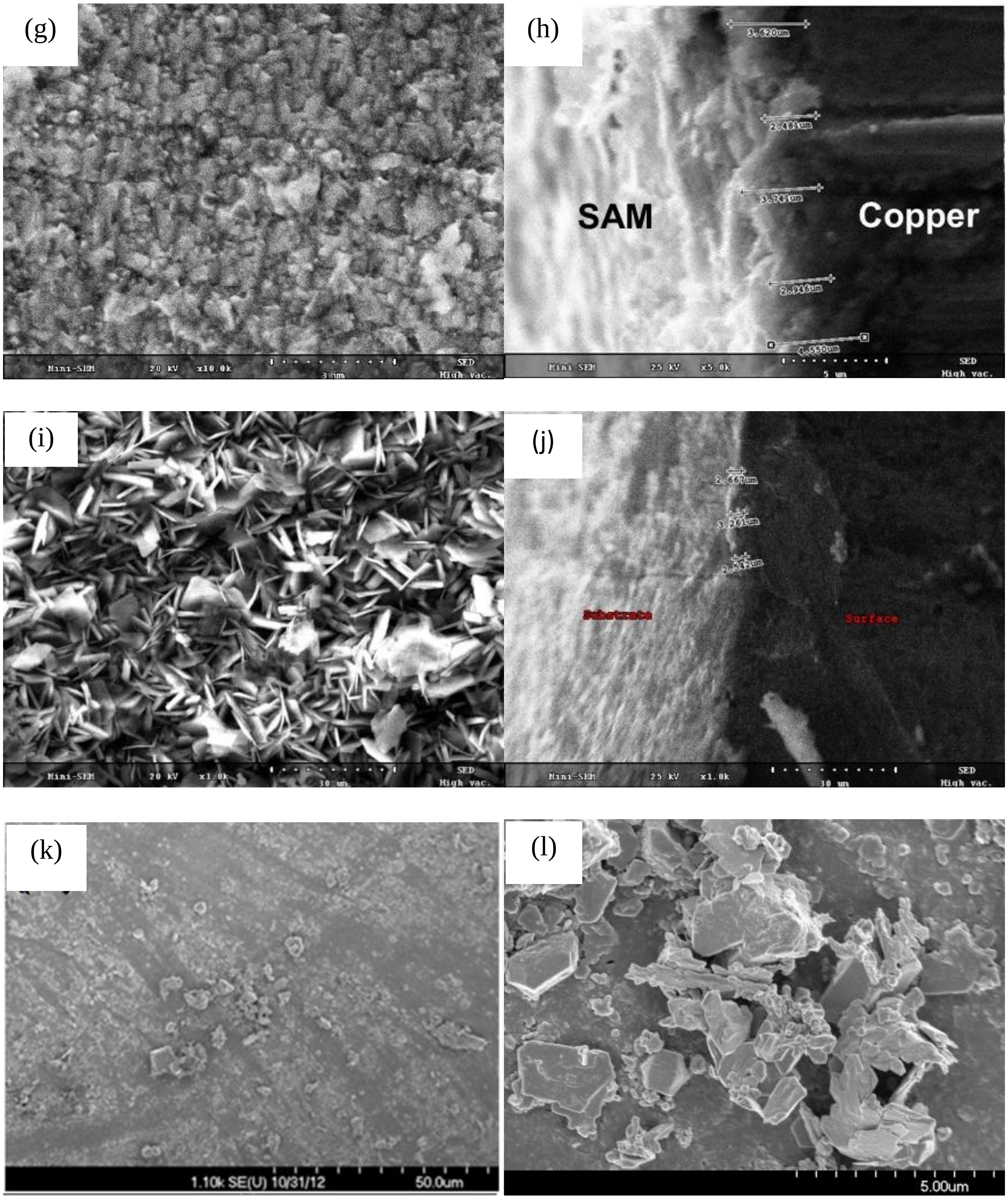

Figure 4.1 Surface coatings SEM images (a-b) polymer coating w/o CNTs surface and cross section thickness (~10 µm) (c-d) polymer coating w/ CNTs surface and cross section thickness (~20 µm) [96] (e-f) hydrophilic copper oxide coating surface and cross section thickness (~1 µm) (g-h) hydrophobic copper oxide coating surface and cross section thickness (~3 µm) (i-j) self-assemble organic coating surface and cross section thickness (~3 µm) (k-l) silver based coating surface and thickness (~1 µm)

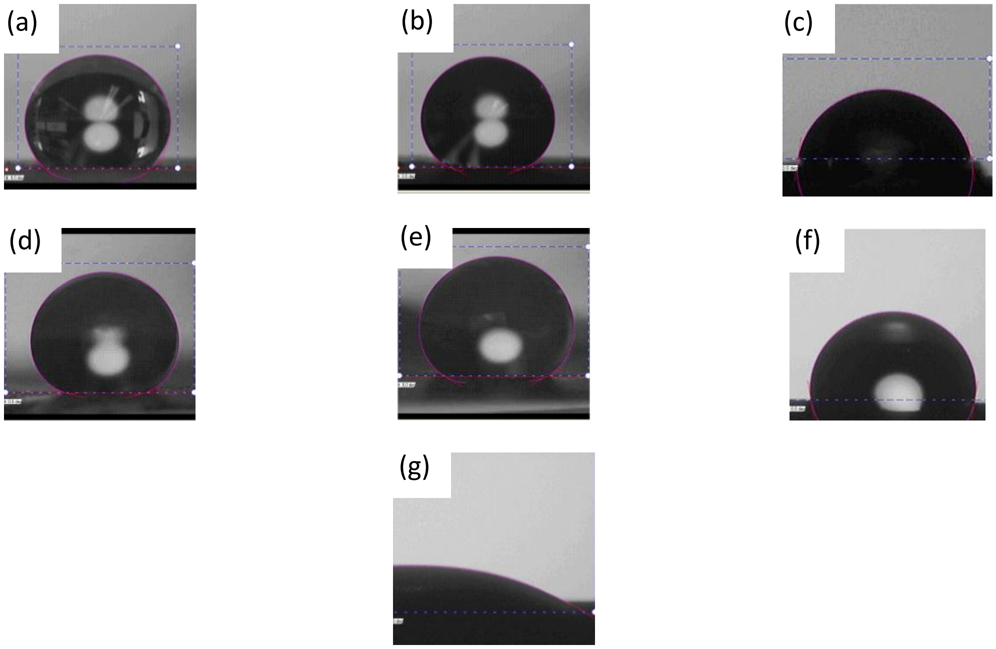

Figure 4.2 Water contact angle (a) polymer coating w/o CNTs, 141° (b) polymer coating w/ CNTs, 158° (c) hydrophilic copper oxide coating, 80° (d) hydrophobic copper oxide coating, 170° (e) self-assembled organic coating, 151° (f) silver based coating, 100° (g) H2O2 oxidized surface, 30°

It is shown in Figure 4.1 that polymer based coatings are relatively thick in comparison with other chemically treated coatings. It is also shown that polymer coatings are porous with the manufacture processes. Fine carpet like textures are found in copper oxide coatings with multi steps mechanical and chemical treatments. Regular spike patterns are visible in self-assembled organic coating and relatively larger void volume appeared between the spiky geometries comparing to copper oxide coatings. Small pebble like surface geometries are found in silver based coatings. Minimum roughness is found in silver based coating. Small void volume is found on the surface. Super-hydrophobic surfaces (contact angle greater than 150°) are found in polymer, hydrophobic copper oxide coating and self-assembled organic coatings. Void volume is found in textured surface and air is trapped between surface texture geometries. Thus the trapped air provided interfacial tension forces between gas, liquid and solid. Large contact angle is formed as a result as explain by Cassie and Baxter [51]. Droplets in Cassie-Baxter state have very low value of CAH. However, large void spaces between coating texture could potentially increase CAH in condensation. Void spaces can be filed with liquid with absent of non-condensable gases, and droplets would change to Wenzel state. Increased CAH and coating thickness could significantly hinder condensation heat transfer as discussed in drop dynamic and heat transfer model in Section 3 previously. Contact angle results from Figure 4.2 were assumed to be in Cassie-Baxter state. The results were used to estimate Young's contact angle. CAHs would be estimated in Wenzel state with given Young's contact angles and surface geometries.

4.8 Condensation experiment facility

Figure 4.3 shows an external condensation apparatus to test the heat transfer performances of test specimens. The photo of the test apparatus is also shown in the Figure. The test apparatus consists of a test section, a cooling loop, and a boiler. The test section consists of condensing chamber which can support to test thee condensing tubes, view ports, valves with plumbing, and measuring instruments. The cooling loop is operated by a chiller/circulator (Affinity, model RWE-012K) with a controlled temperature. The coolant from the chiller flows inside of the each test tube. The boiler generates steam by a submerged heating coil. A hot compressed water controlled by the heater (Advantage Engineering, model Sentra SK-1035 HE) flows inside of the heating coil to generate steam. The steam line is connected at tops of the boiler and the test section to provide water vapor during the tests, while, the condensate from test tubes falls on the bottom of the condensing chamber and flows back to the boiler through the condensate line connected at the bottoms of the condensing chamber and boiler.

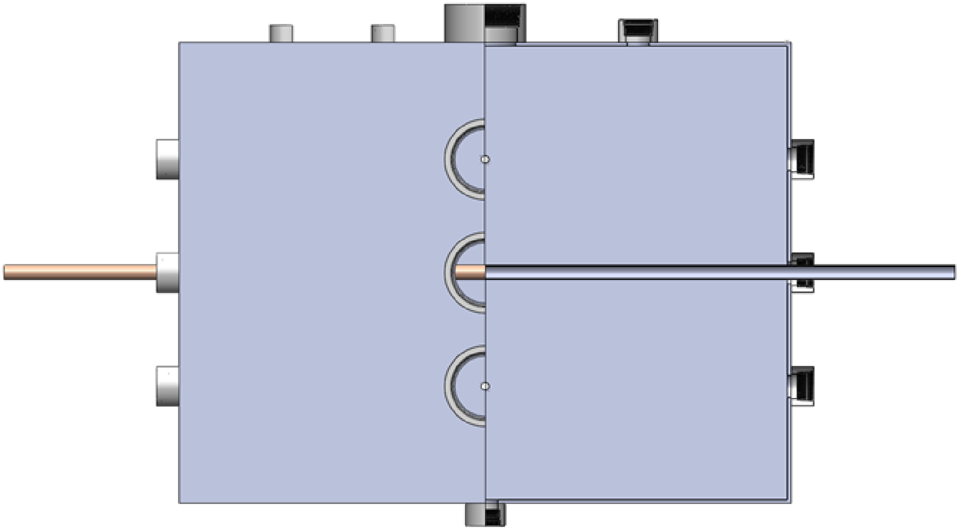

Figure 4.3 Condensation experimental apparatus design

The inlet and outlet of the coolant temperatures were measured by RTDs (OMEGA, class A, ±0.35˚C), and the chamber and steam temperature were measured by T-type thermocouples (±0.5˚C). The pressure of the chamber and boiler were measured by pressure transducers (AST, AST4300, 0 - 345 kPa, ±0.5%). The coolant flow rate was measured by a rotameter (Blue & White, F-440, 0- 5 GPM, ±4% of full scale).

Before experiments, the condensing chamber was vacuumed by a vacuum pump connected at the top of the condensing chamber, so that non-condensable gases in the condensing chamber are expelled to atmosphere. The condensing camber was vacuumed until the water could boil at the vacuumed pressure and the pressure of the condensing chamber was monitored for any leakage. A check valve was installed in the vacuum line to prevent any back flow of air even the vacuum pump is stopped. Once, the leakage of the test setup was verified, the boiler was used to generate steam, so that the water vapor could enter the condensing chamber. During this procedure, the chiller is turned on and coolant inlet temperature was controlled to provide an appropriate temperature of subcool. Once the system reached a steady state condition with keeping the temperatures and pressures of the test section constantly for 5 minutes, data was recorded for a heat transfer performance analysis.

A concentric tubes design is used in the coolant loop in all the testing. Water is used as coolant and coolant flow is between the inner and outer tubes as show in Figure 4.4. Copper tubes (Alloy 122) with different external coatings are used in the experiments. The dimensions of the test section are as follows: 15.9 mm OD and 14.2 mm ID for outer tube, and 9.5 mm OD for inner tube. Flow rate of coolant is fixed at 9 liter per min. Inlet temperatures for coolant are adjusted from 323 K to 363 K. Saturation pressures are varied from 67.5 kPa to 97.8 kPa correspondingly.

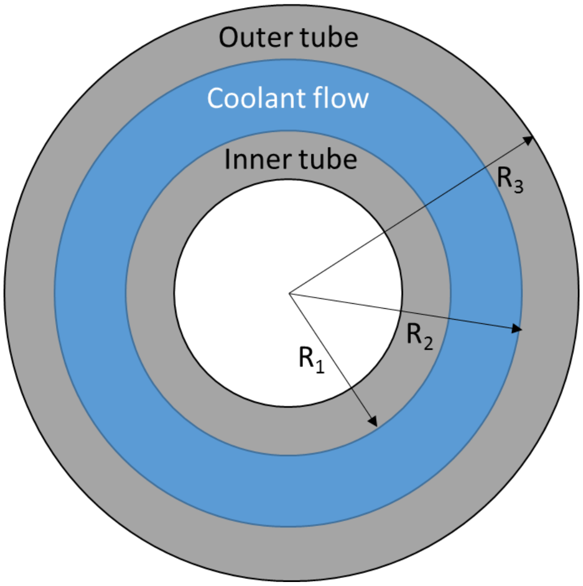

Figure 4.4 Test section cross section schematic

4.9 Data reduction

The coolant side heat transfer rate during the condensation was obtained by

$$q = \dot{m}_c C_{p_c}(T_{c,o} - T_{c,i}) \tag{4.1}$$

$\dot{m}_c$, C_{pc} $T_{c,o}$, $T_{c,i}$ are mass flow rate, heat capacity, outlet and inlet temperatures of coolant.

Overall heat transfer coefficient are calculated by

$$q = UA_{t,o}(T_{sat} - T_{c,ave}) \tag{4.2}$$

where U and $A_{t,o}$ are an overall heat transfer coefficient and an outer surface area of plain brass tube. T_{sat} and $T_{c,ave}$ are saturation temperature of water at the pressure of the chamber and average coolant temperature.

The total thermal resistance is obtained by,

$$R_{tot} = 1/UA_{t,o} \tag{4.3}$$

The total thermal resistance consists of thermal resistances of coolant side, R_c, tube wall, R_w, and condensations, R_{cond}, which is given by

$$R_{tot} = R_c + R_w + R_{cond} \tag{4.4}$$

The thermal resistance of coolant side is as follow,

$$R_c = 1/(h_c A_{t,i}) \tag{4.5}$$

where h_c and $A_{t,i}$ are a heat transfer coefficient of coolant and an inner surface area of plain brass tube, respectively and the heat transfer coefficient of coolant side, h_c is obtained by,

$$Nu_c = \frac{{}^{f}\!/_{8}(Re_c - 1000)Pr_c}{1 + 12.7\left({}^{f}\!/_{8}\right)^{0.5}\left(Pr_c^{\frac{2}{3}} - 1\right)}, 3 \times 10^3 \le Re_c \le 5 \times 10^6, 0.5 \le Pr_c \le 2000 \tag{4.6}$$

where D_d is a hydraulic diameter of concentric tube and f is a friction factor which is given by,

$$f = [0.790 \ln(Re_c) - 1.64]^{-2}, 3 \times 10^3 \le Re_c \le 5 \times 10^6 \tag{4.7}$$

Thermal resistance of the tube wall, R_w is calculated by

$$R_w = \frac{\ln\left(D_{t,o}/D_{t,i}\right)}{2\pi k_t \left(L_{t,o}\right)} \tag{4.8}$$

where $D_{t,o}$ and $D_{t,i}$ are inner and outer diameters of copper tube, respectively and k_t is the thermal conductivity of the copper tube.

Thermal resistance of condensation (R_c) is obtained by

$$R_c = 1/(h_{cond} A_{t,o}) \tag{4.9}$$

Temperature of subcool is defined by

$$\Delta T = T_{sat} - T_w \tag{4.10}$$

where wall temperature is calculated as

$$T_w = q(R_c + R_w) - T_{c,ave} \tag{4.11}$$

Note that the thermal resistance of the condensation includes any effect of surface treatment to increase the condensation performance.

Heat transfer coefficients of a filmwise condensation obtained from Nusselt correlation are also plotted for comparison, which is given by,

$$h_{FWC} = 0.728\left[\frac{g\rho(\rho-\rho_g)h'_{fg}k_c^3}{\mu(T_{sat}-T_w)D_{t,o}}\right]^{0.25}, h'_{fg} = H_{fg}(1+0.68Ja) \tag{4.12}$$

where g, ρ, ρ_g, H_{fg}, μ, Ja are gravitational acceleration, liquid and vapor density, latent heat of condensates, viscosity and Jacob number of condensates.

4.10 Condensation heat transfer results and model comparison

In experimental studies, drop size distributions were observed to be fixed at different subcooling temperatures. Since condensation experiments were done in vacuum in order to minimize errors present from non-condensable gases. Contact angle measurements done in open atmospheres cannot be directly used in condensation models. It would be difficult to measure contact angle when condensing surfaces are being tested for heat transfer performances. Assumptions would be needed to estimate CAH using measurements from open atmosphere.

- Water contact angles measurement in open atmosphere were in Cassie-Baxter state, i.e. air is being trapped inside surface textures
- Water contact angles are in Wenzel state when surface is in testing. Condensate would fill up spaces in the surface textures, assuming that there was no air presented.

- CAH is only based on surface energies and structure geometries of coatings and does not depend on other thermal properties such as thermal conductance.
- Drop radius is assumed to be much greater than length scales of coating surface textures.
- CAH is based on maximum and minimum sustainable contact angles on the surface. It would be fixed at any orientations of the surface.

Figure 4.5 and 4.6 show experimental results for heat fluxes and condensation heat transfer coefficients.

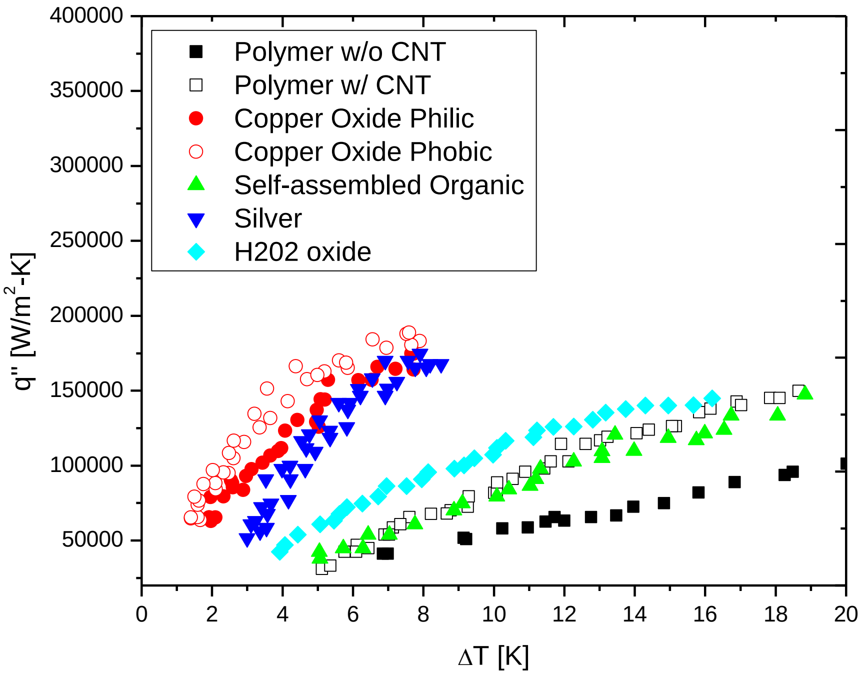

Figure 4.5 Heat fluxes vs. subcooling temperature differences experimental results

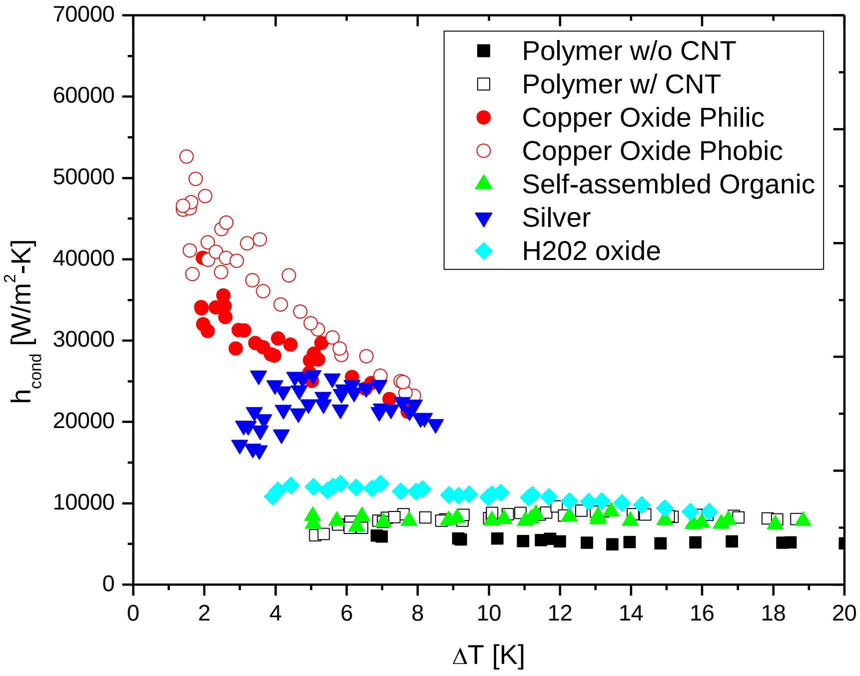

Figure 4.6 Condensation HTC vs. subcooling temperature differences experimental results

Both hydrophilic and hydrophobic copper oxide coatings as well as silver based coatings are shown to have heat fluxes and condensation heat transfer coefficients (CHTCs) higher than H_2O_2 oxide surface (reference surface). Heat fluxes and CHTCs in both polymer coatings (with and without CNTs additives) and self-assembled organic coatings are lower than results of H_2O_2 oxidized surface. Hydrophobic copper oxide heat fluxes and CHTCs resulted highest in values, and polymer coating without CNTs results were at the lowest overall. Each coatings heat transfer (heat fluxes and CHTCs) results from comparing to H_2O_2 oxidized surface are as follows,

- Copper oxide hydrophobic coating was about 300% and 350% higher in heat fluxes and CHTCs;
- Copper oxide hydrophilic coating was about 250% and 300% higher in heat fluxes and CHTCs;
- Silver based coating was about 200% and 250% higher in heat fluxes and CHTCs;
- Self-assembled organic coating and polymer coating with CNTs were about 25% and 20% lower in heat fluxes and CHTCs
- Polymer coating without CNTs was about 50% and 40% lower in heat fluxes and CHTCs.

Condensation visuals are presented in Figure 4.7 in order to further investigate condensate behaviors.

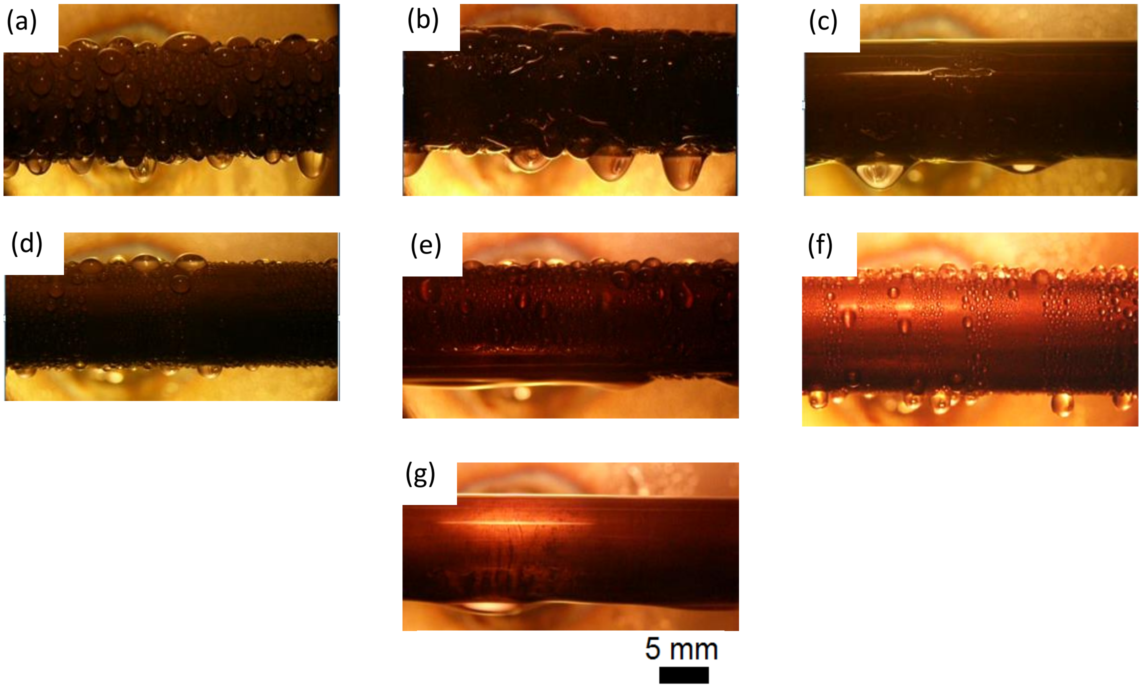

Figure 4.7 Condensation visuals for different coatings (a) polymer w/o CNTs (b) polymer w/ CNTs (c) copper oxide hydrophilic (d) copper oxide hydrophilic (e) self-assembled organic (f) silver (g) H_2O_2 oxidized

As shown in Figure 4.7, large drops are presented in polymer coatings and self-assembled organic coating with drops with large drop radius leaving condensing surface; flat liquid patches are found in copper oxide hydrophilic coating; small drops are shown to leave the condensing surface for both copper oxide hydrophobic surface; H2O2 oxide surface are shown to be in FWC condensation mode.

Drop dynamic and coating thickness are shown in experimental studies to be important parameters in condensation heat transfer. In polymer coatings, coating thickness as well as relatively large void volume inside surface textures seems to hinder condensation heat transfer. Thicker coating increase thermal resistance and large void volume in surface geometries increase CAH. In case of self-assembled organic coating, large void volume is found on surface texture, thus CAH increases. Also, needle like textured geometries are shown on surface, surface projection ratio, ϕ, is small (low area ratio in solid/liquid area contact in Cassie-Baxter state). CAH further increases with lower values of ϕ as shown in Figure 3.14. Heat fluxes lower with high CAH with self-assembled organic coatings. Contact angle of hydrophilic copper oxide coatings are shown to be hydrophilic (less than 90°) in Cassie-Baxter state (see Figure 4.2) on rough surface. Increase roughness on hydrophilic surface could decrease CAH on fully wetted surface as shown in Figure 3.6 and 3.7. Heat fluxes increases with decreased CAH and relatively low coating thickness. Contact angle are shown to be very high on hydrophilic copper oxide surface. CAH would also decrease with high values of contact angles in Figure 3.6 and 3.7, and heat fluxes increases as a result. Minimum roughness are shown in silver based coating and it is showed to be hydrophobic. CAH tend to be low with flat surfaces. Heat fluxes increased as a result with silver based coating with low coating thickness and low CAH value. Validation of heat transfer with drop dynamic model is shown in Figure 4.8.

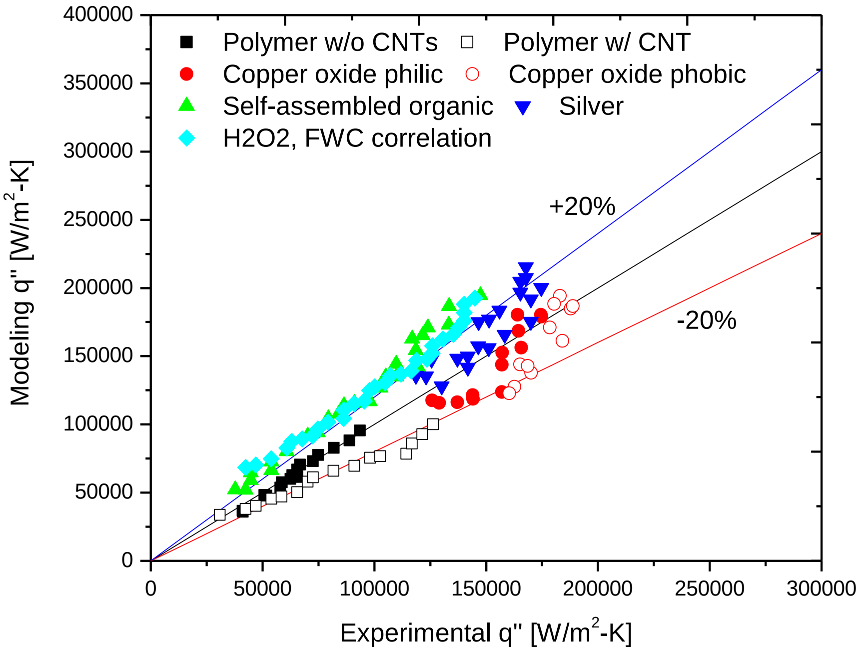

Figure 4.8 Modeling heat flux vs. experimental heat flux results comparison

Heat fluxes results FWC correlation seems to over predict results in H2O2 oxidized surface. Modeling results also over predict heat fluxes in self-assemble organic coating. However, modeling results agrees with experimental data within ±20% margin overall.

4.11 Uncertainties analysis for condensation heat transfer experiments

Uncertainties were calculated based on the NIST technical note 1297 [97] for temperature, pressure, flow rate measurements, which are given by

$$U_Y = \sqrt{\sum_i \left(\frac{\partial Y}{\partial X_i}\right)^2 U_X^2} \tag{4.13}$$

where X_i and Y represent measured and calculated variables respectively. U_X and U_Y are the measured and calculated uncertainties, respectively.

Table 4.2 shows the uncertainty of the calculated results due to the measurements. The maximum uncertainties were obtained at the lowest subcool temperature mostly due to the uncertainties of RTDs and thermocouples.

Table 4.2 Experimental uncertainties

	ΔT	q''	UA	h_c	h_{cond}
Average Uncertainty	±11.8%	±14.2%	±14.6%	±3.4%	±25.0%
Maximum Uncertainty	±31.4%	±32.3%	±32.9%	±3.5%	±52.5%

4.12 Drop sizes distribution studies and future work

Drop sizes distribution is important in topics of DWC. Factors such as surface wetting characteristic and morphologies could greatly impact drop population behavior and drop sizes distribution. In this project, preliminary studies on drop sizes distribution is established. Figure 4.9 and 4.10 shows experimental studies for drop sizes in silver based coating and polymer based coating with CNTs. Coatings were chosen as representation of how droplet would behave in flat and textured surfaces. Figure 4.11

shows population frequencies with respect to drop sizes for silver based coating and polymer based coating.

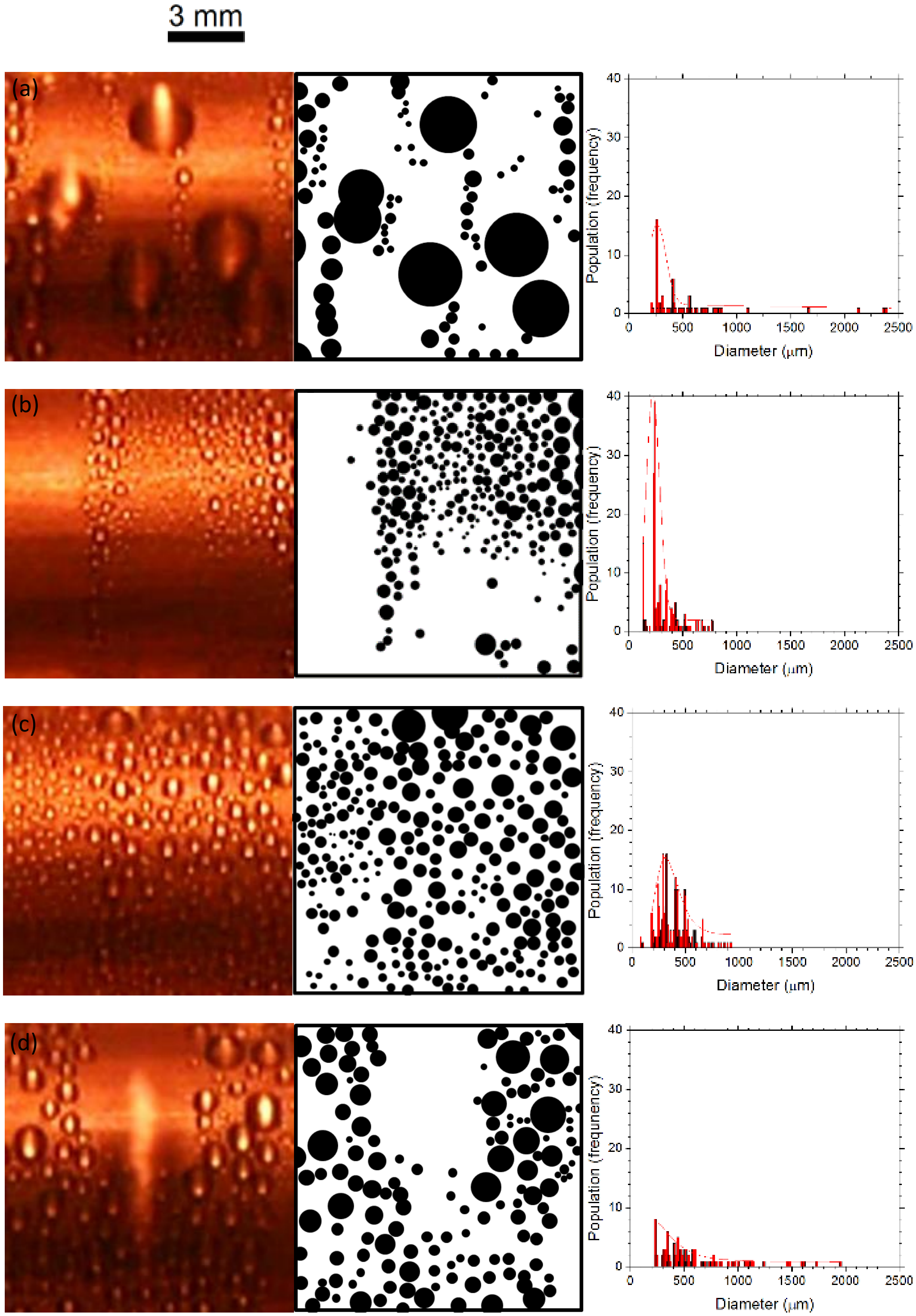

Figure 4.9 Spatial condensate (contour) distribution and the corresponding condensate population at different time frame of silver-coated surface. Still-frame taken at (a) 4.2s, (b) 4.9s, (c) 5.3s, and (d) 5.8s. [98]

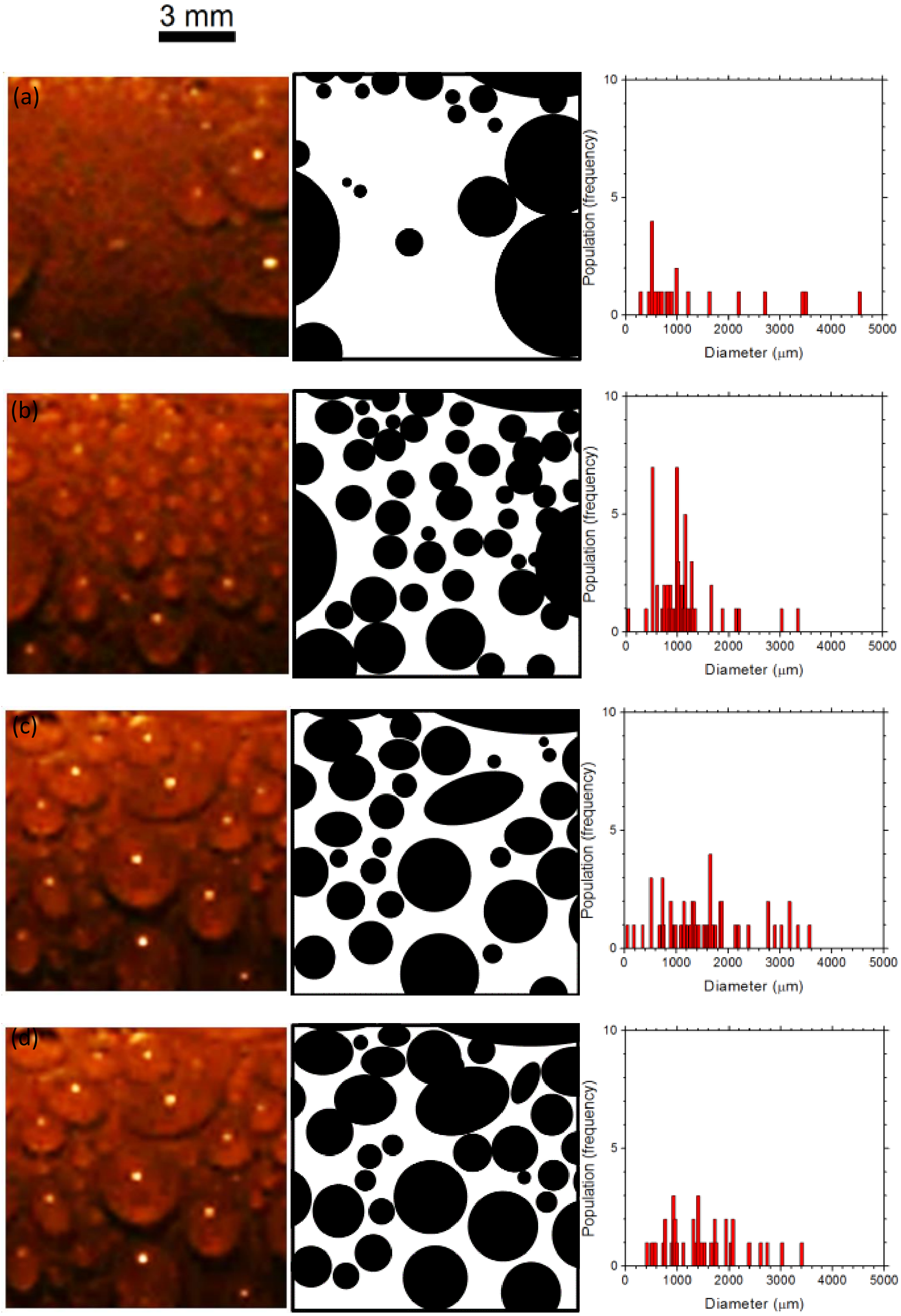

Figure 4.10 Spatial condensate (contour) distribution and the corresponding condensate population at different time frame of polymer coating w/ CNTs surface. Still-frame taken at (a) 0.4s, (b) 6.2s, (c) 12.0s, and (d) 14.9s [98]

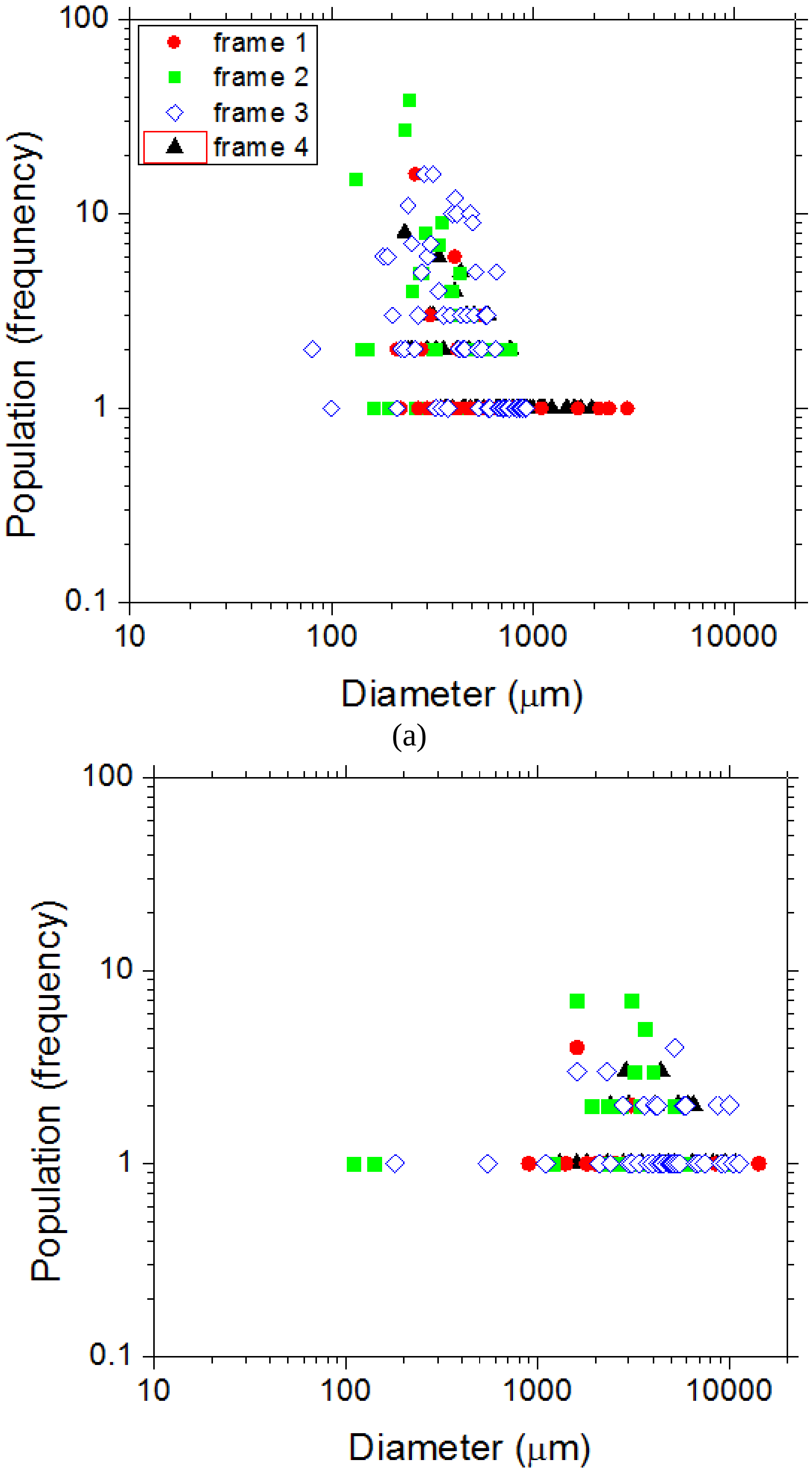

(a)

(b)

Figure 4.11 Drop sizes frequency distribution (a) silver based coating (b) polymer based coating

Surface texture geometries is significant in drop sizes distribution and sweeping periods in the preliminary studies. Drop growth rate appears to be faster in silver based coatings than in polymer coating. Majorities of drop sizes were below 1 mm in the case of silver based coatings while it is above 2 mm in case of polymer coatings. Polymer coating drop renewal periods (~10 seconds) were also two times longer than silver coatings (~5 seconds). Maximum drop radius was also shown to be two times bigger in polymer coating comparing to silver coating (~3 mm to ~1.5 mm).

Surface textures geometries affect CAH, thus maximum drop radius. Drop sizes distribution shifted to the right as CAH increased as shown in Figure 4.10 and 4.11. This means that drop radius of all drop sizes on the surface increased, thus droplets tended to stay on the surface longer. Droplet thermal resistance increased and heat fluxes decreased as a result. Preliminary studies provided important insight into how surface geometries and CAH impact overall drop sizes distribution. Future works should be focus on drop population studies both experimentally and analytically in order to capture details on effect of drop dynamic on drop sizes distribution and population behaviors.

4.13 Condensation experiment summary

Heat fluxes were found to be highest for surface with small contact angle hysteresis. Heat fluxes for copper oxide coatings and silver coatings were shown to be 200% to 300% above the results of FWC. Coating thickness was found to be significant in condensation heat transfer as seen in polymer coatings (10 μm to 20 μm in thickness). CAH were larger for coatings with large void volume between surface textures. As seen in the heat transfer results in self-assemble organic coating and polymer coatings, heat fluxes were 20% to 50% lower than FWC results. Heat transfer model was shown to agree well with experimental results within 20% margin. It was also found that average drop sizes were larger in coatings with high CAH and drop renewal period was also longer. Polymer coating average drop sizes was about 3 mm and silver coating average drop sizes was about 1.5 mm. Polymer coating drop renewal period was about 10 seconds and silver coating drop renewal period was about 5 seconds.

5. Conclusion and future works

5.1 Drop dynamic modeling

In single drop dynamic model, contact angle hysteresis (CAH) can be estimated using theories on surface energies. Roughness and projected top area ratios affects surface energy profile with fixed Young's contact angles. Differences between surface energies in equilibrium states and hysteresis state generally increases as wetted solid/liquid area increases. However, surface energies differences decreases in hydrophilic surfaces when increased wetted area and roughness ratios. This indicated that CAH can be lower when droplet is in Wenzel's state than partially wetted states. Surface energies differences at low and high contact angles remains small at all wetting conditions. It indicated that CAH remains low when young's angle is either super-hydrophilic or super-hydrophobic ($\theta_0 \approx 0$ or $\theta_0 \geq 150°$).

It was found that CAH remains low with any Young's contact angle when totally wetted surface area ratio is small. CAH also increases with increased roughness in general. However, CAH was shown to have an optimum values with varying wetted area ratio when surface is hydrophilic. Furthermore, CAH was shown to be lower with higher roughness ratio when wetting ratio is high ($f_w > 0.7$).

CAH values increases generally when comparing CAH against varying young's contact angle. It is also found that peak values of CAH started form with Young's contact angles with increased wetting. CAH decreases with increasing Young's contact angle at $f_w < 0.5$. Low values of CAH was shown to be at either super-hydrophilic or super-hydrophobic ($\theta_0 \approx 0$ or $\theta_0 \geq 150°$) as previously indicated.

5.2 Heat transfer modeling

CAH affects condensation heat transfer significantly along with surface coating thickness. It was found that heat fluxes decreased rapidly with coating thickness. Heat fluxes were shown to be lower at low thickness and lower wetting in the model. However, temperature difference due to coating increases as coating thickness increases. CAH increases with degrees of wetting, but coating thermal conductance also increases as wetting increases. Heat fluxes were often higher with fully wetting surface then partially wetted surface at higher coating thickness. It is apparent that thermal conductance is a more important factor in condensation heat transfer with thicker coating (>10 μm).

Surface geometry factors were found to be important in heat fluxes. Heat fluxes decreases as roughness increases generally when coating thickness was held constant. CAH increases with roughness ratio, and heat fluxes also decreases. Also, heat fluxes were higher with fully wetted surface at lower roughness ration. However, heat fluxes partially wetted surface were found to be higher when roughness increases at hydrophilic surface.

Heat fluxes were found to be higher at higher values of ϕ when roughness ratio was fixed. For wetting area ratio fw > 0.5, Increased wetting increased heat fluxes at $\phi = 0.1$, but differences between heat fluxes diminished when projection ratio increased to $\phi = 0.3$.

5.3 Condensation experimental studies

Different condensation surfaces were fabricated via different surface treatment techniques. Summary of surface treatment techniques are as follows,

- Polymer coatings were fabricated by bonding different component with heat,
- Micro-textured geometries were introduced to copper oxide coatings and self-assembled coating via chemical treatments,
- Silver coating was created with deposition of silver particles onto the substrate with chemical processes,
- Reference surface was polished and uniformly oxide, thus FWC could be achieved in condensation.

Varying degrees of surface textured geometries, thickness, and wetting characteristics were observed with imaging techniques. It was found that heat fluxes on copper oxide coatings (hydrophilic and hydrophobic) and silver based coating were about 200% to 300% higher than H_2O_2 oxidized surface (reference surface).

Droplets tends to be larger and longer renewal period were observed in self-assembled organic and polymer coatings. In population studies, larger drop sizes were found in polymer coating than silver coating. Drop sizes were concentrated less than 1 mm in case of silver coating, while more drops were in the range of 2 mm in polymer coating.

5.4 Conclusion and future works

Drop dynamics was shown to have direct impact with condensation heat transfer in this study. It is important to understand how surface geometries parameters such as roughness, wetting and coating thickness affect condensation heat transfer. Drop sizes distribution was shown to be in direct relationship with single drop dynamic in experimental observation. Low coating thickness in combination with low CAH results in higher heat flux values. On the other hand, heat fluxes for self-assembled organic coating and polymer coatings were lower than H_2O_2 oxidized surface. Theses coating were found to be porous, thus high roughness ratio. CAH increases and heat fluxes decreases. Future works should focus on detail studies on drop population group behavior both mathematically and experimentally.

Relevant publication

1. S. Lee, K. Cheng, and K. J. Kim, “Comparisons of Dropwise Condensation Heat Transfer using Various Types of Surfaces on a Horizontal Tube,” Proceedings of International Sorption Heat Pump (ISHP) Conference, Maryland, College Park, March 30-April 3, #93

2. Lee, S., Cheng, K., Palmre, V., Bhuiya, M. D., Kim, K. J., Zhang, B. J., & Yoon, H. (2013). Heat transfer measurement during dropwise condensation using micro/nano-scale porous surface. International Journal of Heat and Mass Transfer, 65, 619-626.

3. Cheng, K., Yang, E. S., Lee, C. Y., Ricks, Z., Palmre, V., Kim, K., “Fine-Tuned Polymer Nano-composite Coatings for Use in Geothermal Plants”, ASME SMASIS2011-5012, 2011

4. Cheng, K., Zhang, B. J., Lee, C. Y., Kennedy, M., Kim, S. W., Yoon H. K., Kim K., Liu J., Skandan G., “Biomimetic super-hydrophobic surfaces for use in enhanced dropwise condensation”, SPIE conference Proceedings Vol. 7975, 2011

REFERENCES

1. Tanasawa, I., *Advances in condensation heat transfer.* Advances in heat transfer, 1991. **21**: p. 55-139.

2. Barthlott, W. and C. Neinhuis, *Purity of the sacred lotus, or escape from contamination in biological surfaces.* Planta, 1997. **202**(1): p. 1-8.

3. Bong June Zhang and Jiyeon Park and Kwang, J.K.a.H.Y., *Biologically inspired tunable hydrophilic/hydrophobic surfaces: a copper oxide self-assembly multitier approach.* Bioinspiration & Biomimetics, 2012. **7**(3): p. 036011.

4. Yong, D., et al., *Modifying the anti-wetting property of butterfly wings and water strider legs by atomic layer deposition coating: surface materials versus geometry.* Nanotechnology, 2008. **19**(35): p. 355708.

5. Feng, L., et al., *Super-Hydrophobic Surfaces: From Natural to Artificial.* Advanced materials, 2002. **14**(24): p. 1857-1860.

6. Onda, T., et al., *Super-Water-Repellent Fractal Surfaces.* Langmuir, 1996. **12**(9): p. 2125-2127.

7. Teshima, K., et al., *Transparent ultra water-repellent poly(ethylene terephthalate) substrates fabricated by oxygen plasma treatment and subsequent hydrophobic coating.* Applied Surface Science, 2005. **244**(1–4): p. 619-622.

8. Swain, P.S. and R. Lipowsky, *Contact angles on heterogeneous surfaces: A new look at Cassie's and Wenzel's laws.* Langmuir, 1998. **14**(23): p. 6772-6780.

9. Lafuma, A. and D. Quere, *Super-hydrophobic states.* Nat Mater, 2003. **2**(7): p. 457-460.

10. *Wetting of textured surfaces.* Colloids and Surfaces A Physicochemical and Engineering Aspects, 2002. **206**(1-3): p. 41.

11. *Micrometrically scaled textured metallic hydrophobic interfaces validate the Cassie–Baxter wetting hypothesis.* Journal of Colloid and Interface Science, 2006. **302**(1): p. 308.

12. *Super-hydrophobic Metallic Surfaces and Their Wetting Properties.* Journal of Adhesion Science and Technology, 2008. **22**(3-4): p. 379.

13. *The Fabrication and Switchable Super-hydrophobicity of TiO2 Nanorod Films.* Angewandte Chemie International Edition, 2005. **44**(32): p. 5115.

14. Erbil, H.Y., et al., *Transformation of a Simple Plastic into a Super-hydrophobic Surface.* Science, 2003. **299**(5611): p. 1377-1380.

15. Gao, X. and L. Jiang, *Biophysics: water-repellent legs of water striders.* Nature, 2004. **432**(7013): p. 36-36.

16. Lau, K.K.S., et al., *Super-hydrophobic carbon nanotube forests.* Nano Letters, 2003. **3**(12): p. 1701-1705.

17. Barshilia, H.C., et al., *Effect of substrate roughness on the apparent surface free energy of sputter deposited super-hydrophobic polytetrafluoroethylene thin films.* Applied Physics Letters, 2009. **95**(3): p. 033116-3.

18. Chen, C.-H., et al., *Dropwise condensation on super-hydrophobic surfaces with two-tier roughness.* Applied Physics Letters, 2007. **90**(17): p. 173108.

19. Tanner, D.W., et al., *Heat transfer in dropwise condensation—part I The effects of heat flux, steam velocity and non-condensable gas concentration.* International Journal of Heat and Mass Transfer, 1965. **8**(3): p. 419-426.

20. Tanner, D.W., et al., *Heat transfer in dropwise condensation—part II surface chemistry.* International Journal of Heat and Mass Transfer, 1965. **8**(3): p. 427-436.

21. Blackman, L.C.F., M.J.S. Dewar, and H. Hampson, *An investigation of compounds promoting the dropwise condensation of steam.* Journal of Applied Chemistry, 1957. **7**(4): p. 160-171.

22. Vemuri, S. and K.J. Kim, *An experimental and theoretical study on the concept of dropwise condensation.* International Journal of Heat and Mass Transfer, 2006. **49**(3–4): p. 649-657.

23. Vemuri, S., et al., *Long term testing for dropwise condensation using self-assembled monolayer coatings of n-octadecyl mercaptan.* Applied Thermal Engineering, 2006. **26**(4): p. 421-429.

24. Marto, P.J., et al., *Evaluation of organic coatings for the promotion of dropwise condensation of steam.* International Journal of Heat and Mass Transfer, 1986. **29**(8): p. 1109-1117.

25. Das, A.K., et al., *The use of an organic self-assembled monolayer coating to promote dropwise condensation of steam on horizontal tubes.* Journal of Heat Transfer, 2000. **122**(2): p. 278-286.

26. Erb, R.A. and E. Thelen, *Dropwise condensation characteristics of permanent hydrophobic systems*, in *US Off. Saline Water Res.* 1966.

27. Rose, J.W., *Dropwise condensation theory and experiment: a review.* Proceedings of the Institution of Mechanical Engineers, Part A: Journal of Power and Energy, 2002. **216**(2): p. 115-128.

28. Ma, X., et al., *Advances in dropwise condensation heat transfer: Chinese research.* Chemical Engineering Journal, 2000. **78**(2–3): p. 87-93.

29. Sikarwar, B.S., et al., *Dropwise Condensation Studies on Multiple Scales.* Heat Transfer Engineering, 2011. **33**(4-5): p. 301-341.

30. Gao, L. and T.J. McCarthy, *Contact angle hysteresis explained.* Langmuir, 2006. **22**(14): p. 6234-6237.

31. Dettre, R.H. and R. Johnson, *Contact angle hysteresis II. Contact angle measurements on rough surfaces.* Adv. Chem. Ser, 1964. **43**: p. 136-144.

32. Forsberg, P.S.H., et al., *Contact line pinning on microstructured surfaces for liquids in the Wenzel state.* Langmuir, 2009. **26**(2): p. 860-865.

33. Moradi, S., P. Englezos, and S.G. Hatzikiriakos, *Contact angle hysteresis: surface morphology effects.* Colloid and Polymer Science, 2013. **291**(2): p. 317-328.

34. Marmur, A., *Wetting on Hydrophobic Rough Surfaces: To Be Heterogeneous or Not To Be?* Langmuir, 2003. **19**(20): p. 8343-8348.

35. Okumura, C.I.a.K., *Nucleation scenarios for wetting transition on textured surfaces: The effect of contact angle hysteresis.* EPL (Europhysics Letters), 2006. **76**(3): p. 464.

36. Ishino, C. and K. Okumura, *Wetting transitions on textured hydrophilic surfaces.* The European Physical Journal E, 2008. **25**(4): p. 415-424.

37. Hejazi, V. and M. Nosonovsky, *Contact angle hysteresis in multiphase systems.* Colloid and Polymer Science, 2013. **291**(2): p. 329-338.

38. McHale, G., N.J. Shirtcliffe, and M.I. Newton, Langmuir, 2004. **20**: p. 10146.

39. Lee, S., et al., *A dropwise condensation model using a nano-scale, pin structured surface.* International Journal of Heat and Mass Transfer, 2013. **60**(0): p. 664-671.

40. Kim, S. and K.J. Kim, *Dropwise condensation modeling suitable for super-hydrophobic surfaces.* Journal of heat transfer, 2011. **133**(8).

41. Young, T., *An Essay on the Cohesion of Fluids.* Philosophical Transactions of the Royal Society of London, 1805. **95**: p. 65-87.

42. Tadmor, R., *Line energy and the relation between advancing, receding, and young contact angles.* Langmuir : the ACS journal of surfaces and colloids, 2004. **20**(18): p. 7659-7664.

43. Li, W. and A. Amirfazli, *A thermodynamic approach for determining the contact angle hysteresis for super-hydrophobic surfaces.* Journal of Colloid and Interface Science, 2005. **292**(1): p. 195-201.

44. Li, W. and A. Amirfazli, J. Colloid Interface Sci., 2005. **292**: p. 195.

45. Tongjie Yao and Chuanxi Wang and Quan Lin and Xiao Li and Xiaolu Chen and Jie Wu and Junhu Zhang and Kui Yu and Bai, Y., *Fabrication of flexible super-hydrophobic films by lift-up soft-lithography and decoration with Ag nanoparticles.* Nanotechnology, 2009. **20**(6): p. 065304.

46. *Super-Hydrophobic PDMS Surface with Ultra-Low Adhesive Force.* Macromolecular Rapid Communications, 2005. **26**(22): p. 1805.

47. *Fabrication of nano-structured super-hydrophobic film on aluminum by controllable immersing method.* Applied Surface Science, 2012. **258**(16): p. 5933.

48. *Particle deposition after droplet evaporation on ultra-hydrophobic micro-textured surfaces.* Soft Matter, 2012. **8**(44): p. 11294.

49. *Plasma treatment allows water suspending of the natural hydrophobic powder (lycopodium).* Colloids and Surfaces B: Biointerfaces, 2012.

50. Zong-Han Yang and Chao-Yang Chiu and Jing-Tang Yang and, J.A.Y., *Investigation and application of an ultrahydrophobic hybrid-structured surface with anti-sticking character.* Journal of Micromechanics and Microengineering, 2009. **19**(8): p. 085022.

51. Cassie, A.B.D. and S. Baxter, *Wettability of porous surfaces.* Transactions of the Faraday Society, 1944. **40**(0): p. 546-551.

52. Wenzel, R.N., *Resistance of solid surfaces to wetting by water.* Industrial & Engineering Chemistry, 1936. **28**(8): p. 988-994.

53. Yuan, Y. and T.R. Lee, *Contact Angle and Wetting Properties.* 2013.

54. Quéré, D., *Rough ideas on wetting.* Physica A: Statistical Mechanics and its Applications, 2002. **313**(1): p. 32-46.

55. Adam, N.K. and G. Jessop, *CCL.-Angles of contact and polarity of solid surfaces.* Journal of the Chemical Society, Transactions, 1925. **127**(0): p. 1863-1868.

56. Good, R.J., *A Thermodynamic Derivation of Wenzel's Modification of Young's Equation for Contact Angles; Together with a Theory of Hysteresis1.* Journal of the American Chemical Society, 1952. **74**(20): p. 5041-5042.

57. Shepard, J.W. and F.E. Bartell, *Surface Roughness as Related to Hysteresis of Contact Angles. III. The Systems Paraffin–Ethylene Glycol–Air, Paraffin–Methyl Cellosolve–Air and Paraffin–Methanol–Air.* The Journal of Physical Chemistry, 1953. **57**(4): p. 458-463.

58. Xu, X. and X. Wang, *The modified Cassie's equation and contact angle hysteresis.* Colloid and Polymer Science, 2013. **291**(2): p. 299-306.

59. Johnson Rulon, E. and H. Dettre Robert, *Contact Angle Hysteresis*, in *Contact Angle, Wettability, and Adhesion*. 1964, AMERICAN CHEMICAL SOCIETY. p. 112-135.

60. *Model for solid-liquid and solid-solid friction of rough surfaces with adhesion hysteresis.* The Journal of Chemical Physics, 2007. **126**(22): p. 224701.

61. *The rigorous derivation of Young, Cassie–Baxter and Wenzel equations and the analysis of the contact angle hysteresis phenomenon.* Chemical Physics Letters, 2008. **450**(4-6): p. 355.

62. Michael Nosonovsky and Bharat, B., *Roughness-induced super-hydrophobicity: a way to design non-adhesive surfaces.* Journal of Physics: Condensed Matter, 2008. **20**(22): p. 225009.

63. *Preparation of a durable super-hydrophobic membrane by electrospinning poly (vinylidene fluoride) (PVDF) mixed with epoxy–siloxane modified SiO2 nanoparticles: A possible route to super-hydrophobic surfaces with low water sliding angle and high water contact angle.* Journal of Colloid and Interface Science, 2011.

64. Woo Kyung Cho and Sangjin Park and Sangyong Jon and Insung, S.C., *Water-repellent coating: formation of polymeric self-assembled monolayers on nanostructured surfaces.* Nanotechnology, 2007. **18**(39): p. 395602.

65. Ulrike Mock and Ralf Förster and Wolfgang Menz and Jürgen, R., *Towards ultrahydrophobic surfaces: a biomimetic approach.* Journal of Physics: Condensed Matter, 2005. **17**(9): p. S639.

66. Kakac, S., H. Liu, and A. Pramuanjaroenkij, *Heat exchangers: selection, rating, and thermal design*. 2012: CRC press.

67. Zhong, L., et al., *Effects of surface free energy and nanostructures on dropwise condensation.* Chemical Engineering Journal, 2010. **156**(3): p. 546-552.

68. O'neill, G.A. and J. Westwater, *Dropwise condensation of steam on electroplated silver surfaces.* International journal of heat and mass transfer, 1984. **27**(9): p. 1539-1549.

69. Woodruff, D.W. and J.W. Westwater, *Steam condensation on electroplated gold: Effect of plating thickness.* International Journal of Heat and Mass Transfer, 1979. **22**(4): p. 629-632.

70. Westwater, J.W., *Gold surfaces for condensation heat transfer*. Gold Bulletin, 1981. **14**(3): p. 95-101.

71. Erb, R.A., *Dropwise condensation on gold.* Gold Bulletin, 1973. **6**(1): p. 2-6.

72. Erb, R. and E. Thelen, *PROMOTING PERMANENT DROPWISE CONDENSATION.* Industrial & Engineering Chemistry, 1965. **57**(10): p. 49-52.

73. Erb, R.A., *Wettability of Metals under Continuous Condensing Conditions.* The Journal of Physical Chemistry, 1965. **69**(4): p. 1306-1309.

74. Wilkins, D.G., L.A. Bromley, and S.M. Read, *Dropwise and filmwise condensation of water vapor on gold.* AIChE Journal, 1973. **19**(1): p. 119-123.

75. Zhao, Q. and B. Burnside, *Dropwise condensation of steam on ion implanted condenser surfaces.* Heat Recovery Systems and CHP, 1994. **14**(5): p. 525-534.

76. Holden, K., et al., *The use of organic coatings to promote dropwise condensation of steam.* Journal of heat transfer, 1987. **109**(3): p. 768-774.

77. Haraguchi, T., et al., *The effect of polyvinylidene chloride coating thickness on promotion of dropwise steam condensation.* International journal of heat and mass transfer, 1991. **34**(12): p. 3047-3054.

78. Chen, C.H., et al., *Dropwise condensation on super-hydrophobic surfaces with two-tier roughness.* Applied Physics Letters, 2007. **90**: p. 173108.

79. Chu, K.-H., R. Xiao, and E.N. Wang, *Uni-directional liquid spreading on asymmetric nanostructured surfaces.* Nat Mater, 2010. **9**(5): p. 413-417.

80. Miljkovic, N., et al., *Jumping-Droplet-Enhanced Condensation on Scalable Super-hydrophobic Nanostructured Surfaces.* Nano Letters, 2012. **13**(1): p. 179-187.

81. Adera, S., et al., *Non-wetting droplets on hot superhydrophilic surfaces.* Nat Commun, 2013. **4**.

82. Humplik, T., et al., *Effect of Hydrophilic Defects on Water Transport in MFI Zeolites.* Langmuir, 2014. **30**(22): p. 6446-6453.

83. Miljkovic, N., et al., *Electrostatic charging of jumping droplets.* Nat Commun, 2013. **4**.

84. Sikarwar, B., S. Khandekar, and K. Muralidhar, *Mathematical modelling of dropwise condensation on textured surfaces.* Sadhana, 2013. **38**(6): p. 1135-1171.

85. Khandekar, S. and K. Muralidhar, *Dropwise Condensation on Inclined Textured Surfaces*. 2013, Springer: Dordrecht.

86. Rose, J.W., *Dropwise condensation theory.* International Journal of Heat and Mass Transfer, 1981. **24**(2): p. 191-194.

87. Randolph, A.D. and M.A. Larson, *Theory of particulate processes: analysis and techniques of continuous crystallization*. 1988: Academic Press.

88. Ristenpart, W.D., et al., *Coalescence of Spreading Droplets on a Wettable Substrate.* Physical Review Letters, 2006. **97**(6): p. 064501.

89. Tanner, L.H., *The spreading of silicone oil drops on horizontal surfaces.* Journal of Physics D: Applied Physics, 1979. **12**(9): p. 1473.

90. EGGERS, J., J.R. LISTER, and H.A. STONE, *Coalescence of liquid drops.* Journal of Fluid Mechanics, 1999. **401**: p. 293-310.

91. DUCHEMIN, L., J. EGGERS, and C. JOSSERAND, *Inviscid coalescence of drops.* Journal of Fluid Mechanics, 2003. **487**: p. 167-178.

92. Rose, J. and L. Glicksman, *Dropwise condensation—the distribution of drop sizes.* International Journal of Heat and Mass Transfer, 1973. **16**(2): p. 411-425.

93. Wen, H.W. and R.M. Jer, *On the heat transfer in dropwise condensation.* The Chemical Engineering Journal, 1976. **12**(3): p. 225-231.

94. Le Fevre, E.J., *A theory of heat transfer by dropwise condensation*, J.W. Rose, Editor. 1966, AICHE: Proceedings of the Third International Heat Transfer Conference. p. 362–373.

95. Fernández-García, M. and J.A. Rodriguez, *Metal oxide nanoparticles.* Encyclopedia of Inorganic and Bioinorganic Chemistry, 2007.

96. Cheng, K., et al. *Biomimetic super-hydrophobic surfaces for use in enhanced dropwise condensation*. 2011.

97. Taylor, B.N., *Guidelines for Evaluating and Expressing the Uncertainty of NIST Measurement Results (rev*. 2009: DIANE Publishing.

98. Bong June Zhang, K.C., Kwang Jin Kim, Hyungkee Yoon, Sangsoo Lee, *Dropwise steam condensation induced by a polyphenylene sulfide (PPS)-based coating, a polytetrafluoroethylene (PTFE) coating, and a self-assembled micro/nano silver (SAMS)-deposited coating*. 2014: International Journal of Heat Transfer.

Appendix

A. Drop dynamic model EES codes

```
"Roughnes geometry"

{b=1
h=2
L=3

r_f=1+pi*b*h/(L^2)
phi=pi*b^2/(4*L^2)}
r_f=1
phi=1

"Surface Energy and contact angle"

f_w=1                                       "projected wetted area fraction"
{theta=theta_D*pi/180}                      "varying contact angle"
theta_0_D=150
theta_0=theta_0_D*pi/180                    "flat surface contact angle"
K=r_f*f_w+phi*(1-f_w)
{V=1                                        "Drop Volume"
R=((3*V/pi)^(1/3))*(2-cos(theta)+(cos(theta))^3)^(-1/3)"Drop Radius"
A_C=2*pi*R^2*(1-cos(theta))                 "Cap Area"
A_P=pi*(R*sin(theta))^2                     "Projection area under cap"
E=A_C-A_P*(K*cos(theta_0)-(1-f_w)*(1-phi))} "Surface Energy w/o hysteresis"

cos(theta_E)=K*cos(theta_0)-(1-f_w)*(1-phi) "theta_E for fw<1"
theta_E_D=theta_E*180/pi

"Hysteresis Energy and advancing angle"

{E_H=A_C-A_P*(K*(cos(theta_0)+(cos(theta_E)-cos(theta)))-(1-f_w)*(1-
phi))}"Surface Energy w/ hysteresis"

cos(theta_A)=K*(cos(theta_0)+(cos(theta_E)-
cos(theta_A))+0.5*(sin(theta_A))^2*(cos(theta_A)+2))-(1-f_w)*(1-phi)"Advancing
angle"

{G=cos(theta)-K*(cos(theta_0)+(cos(theta_E)-
cos(theta))+0.5*(sin(theta))^2*(cos(theta)+2))-(1-f_w)*(1-phi)}
theta_A_D=theta_A*180/pi
theta_hys=abs(theta_A-theta_E)              "Contact Angle hysteresis"
theta_hys_D=theta_hys*180/pi
```

B. Dropwise condensation heat transfer modeling codes

```
"Constants"

T_sat=100                                 "oC" "Saturation Temperature"
T_w=T_sat-Delta_T                         "oC" "Surface Temperature"
N_S=2.5*10^11                             "#/m2" "Fin Density"
g1=9.81                                   "m/s2" "Gravitational
Acceleration"
{Delta_T=15}
alpha=90*pi/180                           "Tilting Angle"
h_int=15.7*10^6                           "W/m2-K" "Interfacial heat
transfer coefficient"
gamma=SurfaceTension(Water,T=T_sat)       "N/m" "Surface tension"

theta=150*pi/180                          "Contact Angle"
theta_hys=15.52*pi/180                    "Angle Hysteresis"
theta_rcd=theta-theta_hys                 "Receding Contact Angle"
theta_adv=theta+theta_hys                 "Advancing Contact Angle"

rho=Density(Water,T=T_sat, x=0)           "kg/m3" "Liquid Density"
rho_g=Density(Water,T=T_sat, x=1)         "kg/m3" "Vapor Density"
h_vap=Enthalpy(Water,T=T_sat, x=1)        "J/kg" "Vapor Entalpy"
h_liq=Enthalpy(Water,T=T_sat, x=0)        "J/kg" "Liquid Entalpy"
H_fg=h_vap-h_liq                          "J/kg" "Latent Heat"

delta=1*10^(-6)                           "m" "Coating Thickness"
epsilon=0                                 "Porosity"
f_w=0                                     "Wetting fraction"
k_c=Conductivity(Water,T=T_sat, x=0)      "W/m-K" "Liquid Conductivity"
k_v=Conductivity(Water,T=T_sat, x=1)      "W/m-K" "Vapor Conductivity"
k_f=0.2                                   "W/m-K" "Fin conductivity"
k_coat=f_w*epsilon*k_c+(1-f_w)*epsilon*k_v+(1-epsilon)*k_f"Effective
Conductivity"

"Max and Min drop radius"

r_max=sqrt((1.25*sin(theta)/(2-3*cos(theta)+(cos(theta))^3))*((cos(theta_rcd)-
cos(theta_adv))*gamma/((rho-rho_g)*g1*sin(alpha))))
r_min=2*(T_sat+273.15)*gamma/(H_fg*rho*Delta_T)
r_e=(4*N_S)^(-1/2)

"Drop period"
```

```
{tau=(3*r_e^2*(A_2*r_e+A_3)^2)/(A_1*(11*A_2*r_e^2-14*A_2*r_e*r_min+8*A_3*r_e-11*A_3*r_min))}

tau=(K/2)*(r_max^2-r_min^2)*(G_1+G_2)^(-1)
K=(2-3*cos(theta)+cos(theta)^3)/(6*(1-cos(theta)))
G_1=(A_1/(A_2*A_3))*((A_2*r_min+A_3)*ln((A_2*r_e+A_3)/(A_2*r_min+A_3))+A_2*r_min*ln(r_min/r_e))
G_2=r_min*(gamma/mu)*(1-cos(theta))^3*ln(r_max/r_e)
mu=Viscosity(Water,T=T_sat,x=0)

"Small drop distribution"

{n=(1/(3*pi*r_e^3*r_max))*((r_e/r_max)^(-2/3))*(r_0*(r_e-r_min)/(r_0-r_min))*((A_2*r_0+A_3)/(A_2*r_e+A_3))*exp(B_1+B_2)}
A_1=Delta_T/(2*rho*H_fg)
A_2=theta*(1-theta)/(4*k_c*sin(theta))
A_3=delta*(1-cos(theta))/(k_coat*(sin(theta))^2)+1/(2*h_int)

B_1=(A_2/(tau*A_1))*((r_e^2-r_0^2)/2+r_min*(r_e-r_0)-r_min^2*ln((r_0-r_min)/(r_e-r_min)))
B_2=(A_3/(tau*A_1))*(r_e-r_0-r_min*ln((r_0-r_min)/(r_e-r_min)))

"Large drop distribution"

{N=(1/(3*pi*r_1^2*r_max))*((r_1/r_max)^(-2/3))}

"Drop heat transfer"

{q_d=Delta_T*pi*r_0^2*(1-r_min/r_0)/(delta/(k_coat*sin(theta)^2)+r_0*theta/(4*k_c*sin(theta)^2)+1/(2*h_int))}
{q_d_1=Delta_T*pi*r_1^2*(1-r_min/r_1)/(delta/(k_coat*sin(theta)^2)+r_1*theta/(4*k_c*sin(theta)^2)+1/(2*h_int))}

"Overall heat flux"

q_flux_small=integral(Delta_T*pi*r_0^2*(1-r_min/r_0)/(delta/(k_coat*sin(theta)^2)+r_0*theta/(4*k_c*sin(theta)^2)+1/(2*h_int))*(1/(3*pi*r_e^3*r_max))*((r_e/r_max)^(-2/3))*(r_0*(r_e-r_min)/(r_0-r_min))*((A_2*r_0+A_3)/(A_2*r_e+A_3))*exp(B_1+B_2),r_0,r_min*1.01,r_e)
q_flux_large=integral(Delta_T*pi*r_1^2*(1-r_min/r_1)/(delta/(k_coat*sin(theta)^2)+r_1*theta/(4*k_c*sin(theta)^2)+1/(2*h_int))*(1/(3*pi*r_1^2*r_max))*((r_1/r_max)^(-2/3)),r_1,r_e,r_max)
q_flux=q_flux_small+q_flux_large
```

C. EES codes for experiment data reduction

```
TT=Type+T_v_1+T_v_2+T_v_3+T_v_4+T_avg+T_c_i+T_c_o+Del_T+V_dot_gm
p+P_cond
P_sat=(P_cond-P_delta)*convert(psi, kPa)
T_s_calculated=T_sat(Water,P=P_sat)
T_s_Delta=T_s_calculated-T_s
T_s_Delta=0

"Condenser conditions"
T_s=T_avg
T_i=T_c_i
T_o=T_c_o

{T_s=94.8 [C]}                          "Condenser chamber
temperature [C]"
P_s=P_sat(Water, T=T_s)                 "Condenser chamber pressure
[kPa]"

"Condenser tube properties"

d_i=0.561*convert(in,m)                 "Outer Tube internal diameter
[m]"
d_o=5/8*convert(in,m)                   "Outer Tube outter diameter [m]"

d_io=3/8*convert(in,m)                  "Inner Tube outter diameter [m]"

L=21*convert(in,m)                      "Tube length [m]"


"Cross Sectional Area"
A_c_i=pi*(d_i^2*0.25-d_io^2*0.25)       "Tube cross sectional area [m^2]"

"Heat transfer Area"
A_i=d_i*pi*L                            "Tube inner surface area [m^2]"
A_o=d_o*pi*L                            "Tube outer surface area [m^2]"

"Hydraulic Diameter"
d_h=d_i-d_io{4*A_c_i/(pi*(d_i+d_io))}


"Coolant properties and conditions"
{T_i=79.2 [C]}                          "Coolant inlet termperature [C]"
{T_o=81.7 [C]}                          "Coolant outlet temperature [C]"
```

```
V_dot_c=V_dot_gmp *convert(gpm,m3/s)        "Coolant volume flow rate [m3/s]"
m_dot_c=rho_c*V_dot_c                       "Coolant mass flow rate [kg/sec]"
v_c=V_dot_c/A_c_i                           "Coolant velocity [m/s]"

"Coolant properties"
T_c_avg=(T_o+T_i)/2                         "Mean interanl termperature [C]"
rho_c=Density(Water,T=T_c_avg,x=0)          "Coolant density [kg/m3]"
mu_c=Viscosity(Water,T=T_c_avg,x=0)         "Coolant viscosity [kg/m-s]"
Pr_c=Prandtl(Water,T=T_c_avg,x=0)           "Coolant Prantl number"
k_f_c=Conductivity(Water,T=T_c_avg,x=0)     "Coolant conductivity [W/m2-K]"
C_p_c=Cp(Water,T=T_c_avg,x=0)               "Coolant heat capacity [J/kg-K]"

"Heat transfer Rate"
Q_dot=m_dot_c*C_p_c*(T_o-T_i)               "Coolant heat transfer [W]"
q=Q_dot/A_o                                 "heat flux [W/m2]"

"Overall Heat transfer coefficeint X Area"
UA=Q_dot/(T_s-(T_c_i+T_c_o)/2)              "Overall heat transfer coefficient
[W/m2-K]"

R_tot=1/UA                                  " [K/W] Total Resistant thermal
resistant" "Total thermal resistant = internal resistant+wall resistant+coating
resistant+environment resistant"

"Coolant side thermal resistance"
Re_c=rho_c*v_c*d_h/mu_c                     "Coolant Reynold number"
f_c_t=(0.790*ln(Re_c)-1.64)^(-2)            "Friction Factor Developed by
Petukhov 3000 < Re < 5*10^6"
Nusselt_c=(((f_c_t/8) *(Re_c-1000)*Pr_c)/(1+12.7*(f_c_t/8)^0.5*(Pr_c^(2/3)-
1)))"Gnielinski  0.5< Pr < 2000, 3000 < Re < 5*10^6"
h_c=Nusselt_c*k_f_c/d_h
R_coolant=1/(h_c*A_i)                       " [K/W]" "coolant side thermal
resistant"

"Wall thermal resistance"
K=k_('Copper', (T_i+T_o)/2)                 "Tube conductivity [W/(m^2*K)]"
R_w=ln(d_o/d_i)/(2*pi*L*K)                  " [K/W]" " Wall thermal resistant"

"Wall Temperatures"
Q_dot=(T_w-T_c_avg)/(R_coolant+R_w)         "oC" "Calcuate the Wall
temperature"
T_subcool=T_s-T_w                           "oC" "Temperature of Subcool"

"Condensation thermal resistance"
```

```
R_cond=R_tot-(R_coolant+R_w)                "Total thermal resistant = internal
resistant+wall resistant+coating resistant+environment resistant"
R_Ratio=R_coolant/R_cond                    "Ratio of Internal and external
thermal resistant"
R_cond=1/(h_cond*A_o)

{U=Q_dot/(T_subcool*A_o)                    "Overall heat transfer coefficient
[W/m2-K]"
{R_tot=1/(U*A_o)}                           "Total Resistant thermal resistant
[K/W]"
R_tot=R_i+R_w+R_ct+R_c                      "Total thermal resistant = internal
resistant+wall resistant+coating resistant+environment resistant"
R_i=1/(h_i*A_i)

R_ct=0
h_c=U                                       "since R_ct =0"
R_c=1/(h_c*A_o)

r_in_c=R_i/R_c                              "Ratio of Internal and external
thermal resistant"

"Wall Temperatures"

 }

"Nusselt FWC"
h_FWC=0.729*((g*rho_l*(rho_l-rho_v)*h_fg_FWC*k_l^3)/(mu_l*(T_s-
T_w)*d_o))^0.25"Nusselt Correlation for filmwise condensation"
Ja_FWC=(cp_l*(T_s-T_w))/(h_fg)
h_fg_FWC=h_fg*(1+0.68*Ja_FWC)
g=9.81 [m/s^2]
rho_l=Density(Water,T=(T_s+T_w)/2,x=0)
rho_v=Density(Water,T=T_s,x=1)
h_fg=h_g-h_f

cp_l=Cp(Water,T=(T_s+T_w)/2,x=0)
h_g=Enthalpy(water,T=(T_s+T_w)/2,x=1)
h_f=Enthalpy(water,T=(T_s+T_w)/2,x=0)
mu_l=Viscosity(water,T=(T_s+T_w)/2,x=0)
k_l=Conductivity(water,T=(T_s+T_w)/2,x=0)
{Pr_l=Prandtl(Water,T=(T_s+T_w)/2,x=0)}
nu_l=mu_l/rho_l

q_FWC=h_FWC*(T_s-T_w)
Q_FWC_F=h_FWC*(T_s-T_w)*A_o
```

```
RQ=(Q_dot-Q_FWC_F)/Q_FWC_F*100
RH=(h_cond-h_FWC)/h_FWC*100
h_band=(h_cond-h_FWC)/h_FWC*100

h_Griffith=51104+2044*T_s

{h_v_NFWC_1=(Re_delta_1*mu_l*h_fg_FWC)/(4*L*(T_s-T_w))}
Re_delta_1=3.78*((k_l*L*(T_s-T_w))/(mu_l*h_fg_FWC*(nu_l^2/9.81)^(1/3)))
^0.75

h_v_NFWC_2=(Re_delta_2*mu_l*h_fg_FWC)/(4*L*(T_s-T_w))
Re_delta_2=((3.70*k_l*L*(T_s-T_w))/(mu_l*h_fg_FWC*(nu_l^2/9.81)^(1/3))+4.8)
^0.82

{h_v_NFWC_3=(Re_delta_3*mu_l*h_fg_FWC)/(4*L*(T_s-T_w))}
{Re_delta_3=(((0.069*k_l*L*(T_s-
T_w))/(mu_l*h_fg_FWC*(nu_l^2/9.81)^(1/3)))*Pr_l^0.5-151*pr_l^0.5+253) ^0.75}

h_Wu_1976=k_l/0.045*(3*(0.045/r_e)^(2/3)-(2*(0.045/r_max)^(2/3)))
N_s=2*10^11
r_e=1/(2*(2*(N_s)^0.5))
r_max=1*10^(-4)
```

D. Experimental Data

Table D.1 Polymer coating without CNTs heat transfer experimental data

ΔT	q”	h_{cond}
6.993	41131	5882
6.854	41223	6014
9.139	51775	5665
9.214	50835	5517
10.24	57925	5656
10.97	58638	5343
11.47	62593	5459
12	63285	5273
11.73	65632	5593
12.76	65611	5141
13.48	66744	4950
13.96	72570	5197
14.83	74936	5053
15.81	81915	5182
16.84	88910	5281
18.26	93601	5127
18.49	95859	5183
20.02	101187	5053
21.45	105425	4916
21.85	110149	5042
23.43	109740	4683
24.37	115099	4723
25.33	119243	4708
26.11	124643	4773
27.07	131426	4856

29.11	128863	4427
29.65	136058	4589

Table D.2 Polymer coating with CNTs heat transfer experimental data

ΔT [K]	q” [W/m^2]	h$_{cond}$ [W/m^2-K]
5.119	30973	6051
5.766	42457	7364
6.108	47064	7705
6.897	53987	7827
7.133	58600	8215
7.605	65541	8618
8.78	70191	7994
9.259	72523	7832
10.01	81794	8172
10.54	91076	8638
11.43	98069	8581
11.62	102718	8837
11.91	114348	9600
13.02	116758	8968
14.05	121478	8646
15.17	126241	8321
15.83	135608	8565
16.89	142700	8448
17.85	145130	8132
18.65	149904	8039
5.364	33263	6202
6.089	42459	6973
6.44	44772	6952
7.024	53985	7685
7.349	60895	8286
8.219	67837	8253

8.667	67866	7830
9.292	79424	8547
10.09	81790	8108
10.1	88735	8785
10.89	95723	8788
12.12	102722	8477
12.61	114368	9067
13.23	119061	9000
14.4	123805	8595
15.06	126212	8382
16.15	137928	8543
17.02	140364	8245
18.11	145123	8015

Table D.3 Copper oxide hydrophilic coating heat transfer experimental data

ΔT [K]	q" [W/m^2]	h_{cond} [W/m^2-K]
1.914	65308	34122
1.971	63016	31977
1.927	65423	33942
1.965	78929	40173
2.597	85389	32878
2.884	83691	29020
2.969	92917	31296
3.433	101904	29685
3.875	109684	28306
4.079	123328	30234
5.032	125936	25028
4.958	129088	26037
4.978	137125	27545
5.295	157127	29674
6.534	157249	24065
7.212	164462	22805
7.719	164018	21249
2.094	65265	31164
2.328	79322	34079
2.578	88185	34211
2.538	90183	35533
3.122	97578	31259
3.657	106614	29151
3.966	111592	28135
4.427	130468	29472
5.084	144221	28366

5.203	143991	27676
6.158	157046	25504
6.693	165764	24767
7.72	174576	22613
7.659	174738	22814

Table D.4 Copper oxide hydrophobic coating heat transfer experimental data

ΔT [K]	q" [W/m^2]	h$_{cond}$ [W/m^2-K]
1.406	64824	46099
1.666	63587	38170
1.597	65581	41054
1.596	73792	46248
1.629	76540	46980
2.109	84211	39933
2.1	88307	42048
2.473	94932	38387
2.33	95322	40918
2.614	104930	40145
2.909	115746	39786
3.353	125386	37395
3.654	131662	36037
4.152	143004	34441
4.7	157680	33551
5.191	162776	31357
4.995	160342	32098
5.853	165176	28221
6.953	178510	25675
7.895	183047	23186
7.658	180478	23566
1.405	65446	46578
1.506	79246	52608
1.759	87703	49862
2.028	96817	47735
2.481	108353	43680

2.62	116597	44506
3.207	134509	41942
3.568	151358	42421
4.375	166208	37993
5.606	170130	30350
5.809	168598	29025
6.562	184168	28068
7.52	187882	24984
7.593	188805	24866

Table D.5 Self-assembled organic coating heat transfer experimental data

ΔT [K]	q” [W/m^2]	h_{cond} [W/m^2-K]
5.069	37855	7467
5.044	42454	8417
5.722	44764	7824
6.281	44783	7130
6.43	53978	8394
7.037	53999	7673
7.761	60937	7851
8.864	70182	7918
9.108	74810	8214
10.09	79472	7873
10.43	84113	8068
11.03	86448	7841
11.2	91096	8135
11.32	98052	8660
12.27	102745	8375
13.07	105102	8044
13.07	109758	8395
13.98	109798	7854
13.44	120703	8980
14.95	118550	7932
15.75	116899	7424
15.99	121582	7602
16.54	123951	7492
16.74	133330	7965
18.06	133440	7388
18.84	147516	7831

Table D.6 Silver based coating heat transfer experimental data

ΔT [K]	q” [W/m^2]	h_{cond} [W/m^2-K]
2.998	51584	17206
3.109	60767	19543
3.235	63080	19501
3.411	72304	21197
3.671	74634	20329
3.528	90759	25723
3.985	97689	24511
4.211	100027	23752
4.67	111602	23897
4.548	116247	25558
4.767	120901	25363
5.056	130205	25753
5.596	141863	25351
6.155	151233	24571
6.547	158259	24174
6.92	169940	24556
7.569	170024	22463
8.193	167776	20479
7.902	174720	22112
3.362	56165	16706
3.546	58499	16496
3.575	67691	18937
4.166	76925	18464
4.224	90763	21488
4.647	97730	21032
4.932	109304	22163

5.355	118602	22148
5.34	123157	23064
5.83	125609	21547
5.85	137215	23457
5.914	141869	23988
6.211	146539	23593
6.917	146623	21196
6.985	151273	21658
7.25	155946	21510
7.769	165362	21284
8.083	165391	20461
8.502	167768	19733